Marquette University
e-Publications@Marquette

Master's Theses (2009 -) Dissertations, Theses, and Professional Projects

EEG Source Localization of Visual and Proprioceptive Error Processing During Visually-Guided Target Tracking with the Wrist

Prajakta Sukerkar
Marquette University

Recommended Citation
Sukerkar, Prajakta, "EEG Source Localization of Visual and Proprioceptive Error Processing During Visually-Guided Target Tracking with the Wrist" (2010). *Master's Theses (2009 -)*. Paper 70.
http://epublications.marquette.edu/theses_open/70

EEG SOURCE LOCALIZATION OF VISUAL AND PROPRIOCEPTIVE ERROR PROCESSING DURING VISUALLY-GUIDED TARGET TRACKING WITH THE WRIST

by

Prajakta Ashok Sukerkar, B.S.

A Thesis submitted to the Faculty of the Graduate School,
Marquette University,
in Partial Fulfillment of the Requirements for
the Degree of Master of Science

Milwaukee, Wisconsin

December 2010

ABSTRACT
EEG SOURCE LOCALIZATION OF
VISUAL AND PROPRIOCEPTIVE ERROR PROCESSING
DURING VISUALLY-GUIDED TARGET TRACKING WITH THE WRIST

Prajakta A. Sukerkar, B.S.
Department of Biomedical Engineering
Master of Science

Sensorimotor error feedback plays an integral role in movement; it adapts the sensorimotor control system to rapid changes in environmental loads and allows smooth limb coordination. Studies have shown the cerebellum, parietal, and premotor cortices to be involved in error processing, but the specific neural function of those areas remain relatively unknown. The objective of this study was to characterize the neural sources that underlie the computation of visual and proprioceptive error during goal-directed movement. We tested the hypothesis that the cortical networks meditating the two sensory error systems are distinct.

Subjects (n=7) used a cursor to track a moving target presented on a computer display. Cursor position on the screen was yoked to a 1-D wrist manipulandum that recorded wrist position, velocity, and torque and applied controlled torques to the wrist. External displacement errors were applied as either force perturbations to the wrist (Proprioceptive condition) or visual displacements to cursor position (Visual condition). Five levels of displacement were applied to identify neural responses that co-varied with the magnitude of displacement. EEG was collected from 64 electrodes. Distributed cortical source modeling (Brainstorm v.3) identified cortical sources that contributed to the averaged EEG activity across error levels.

In force perturbation trials, current source density across subjects showed early somatosensory, premotor, motor, and frontal activity ranging from 43±5 ms to 48±6 ms, followed by parietal activity at 70±8 ms. In visual perturbation trials, parietal activation at 113±8 ms was followed by sensory, motor, and premotor activation (123±42 ms to 131±22 ms). Spatial analyses suggest error representations for proprioception and vision may be computed in spatially distinct areas of frontal and parietal cortices.

The temporal sequence of error-related activity suggests that sensorimotor error may not initially be computed in parietal regions before being processed in motor areas. The early premotor/motor activation in the Proprioceptive condition suggests that a course estimate of error is first computed in those areas before a more accurate representation of error is generated in the parietal regions. This may occur to initiate a course correction faster in the direction of the error while gathering more information about the error.

DEDICATION

To all teachers of the past, present, and future

Yatah sarvani bhutani pratibhanti stithani cha
yatrai vo pasamam yanti tasmai satyatmane namah

Salutations to that reality in which all the elements,
and all the animate and inanimate beings shine as if they have an independent existence,
and in which they exist for a time
and into which they merge.

‘Vasistha’s Yoga’.
by Swami Venkatesananda,
State University of New York Press, Albany, NY

ACKNOWLEDGEMENTS

I would like to thank my parents for their unending support and unconditional love. A special note of gratitude to my father for pushing me headfirst into graduate school – this journey has undoubtedly been one of the most rewarding experiences of my life. A huge hug to my sister, Kavita, who never turned down an opportunity to help me with my endless Matlab questions, and for always encouraging me to stay strong and push through whenever I had fleeting thoughts of renouncing everything and absconding to the Himalayas.

I would like to acknowledge and thank my advisor, Dr. Scott Beardsley, whose knowledge, ethics, and support have been a true motivation throughout my thesis. His strive for nothing short of perfection and professionalism has helped me improve as a researcher. I would also like to extend my gratitude to my committee members, Drs. Robert Scheidt and Brian Schmit, for graciously allowing me to use their lab resources and equipment and for offering their invaluable feedback on my thesis project. A note of recognition also to Drs. Sylvain Baillet and Aniko Szabo for getting me acquainted with the necessary skill set to perform the analyses outlined in my thesis, and a big 'thank you' to the Falk Family Medical Research Trust and the Department of Biomedical Engineering at Marquette University for their financial support of this project.

My thesis would have been much less enjoyable had it not been for the help of my many friends at Marquette University. I would especially like to thank my labmate, Chintan, and friends, Madhavi, Ashvini, Nuttaon, Krishnaj, Sanket, Ryan, Sunaina (& UCSB), Sheraz, Sampada, Tushar, David, Megan, and Jain, for all their help and support.

My love and gratitude goes out to my friends in the Art of Living for being my loving family in the United States. Special thanks to Naresh, Shraddha, and Parneet.

Last and in no way least, I would like to express a heart full of gratitude to my spiritual advisor, friend, and mentor, Sri Sri Ravi Shankar, for making me grow leaps and bounds as a person, for giving me an opportunity to give back to the society, and for making my life magical and beautiful – Jai Guru Dev!

TABLE OF CONTENTS

DEDICATION i

ACKNOWLEDGEMENTS ii

LIST OF FIGURES v

LIST OF TABLES vi

LIST OF ABBREVIATIONS vii

1 INTRODUCTION AND SPECIFIC AIMS 1

2 BACKGROUND & SIGNIFICANCE 3

2.1 Motivation 3

2.2 Types of Sensory Error 4

2.3 Brain Areas Involved in Sensorimotor Error Processing 5

2.3.1 The Posterior Parietal Cortex 5

2.3.2 The Cerebellum 11

2.3.3 The Premotor, Motor, and Medial-Frontal Cortices 12

2.4 Event Related Potentials in Sensory Error Processing: the N100, P300, and fERN 14

2.5 Visual and Proprioceptive Sensorimotor Processing 16

2.6 Significance 17

3 METHODS 19

3.1 Overview 19

3.2 Experimental Apparatus 19

3.3 Subjects 21

3.4 Experimental Design 21

3.4.1 Trial Structure 22

3.4.2 Proprioceptive Trials 23

3.4.3 Visual Trials 24

3.4.4 Triggering 26
3.5 Experimental Setup and Protocol 31
3.6 Analysis Methods 37
3.6.1 Behavioral Data 37
3.6.2 EEG Data 38
3.6.3 Cortical Source Reconstruction 40
3.6.4 Source Localization within ROI's 42
4 EXPERIMENTAL RESULTS 50
4.1 Behavioral response to proprioceptive and visual displacements 50
4.2 Evoked neural response to proprioceptive and visual displacements 55
4.3 Cortical source reconstruction across proprioceptive and visual ROI's 58
4.4 Temporal activation of sources correlated with proprioceptive and visual error 63
4.5 Spatial activation of cortical sources correlated with proprioceptive and visual error 70
5 DISCUSSION 74
5.1 Differences in Evoked Responses to Visual and Proprioceptive Displacements 76
5.2 Temporal Dynamics of Error Processing for Proprioceptive and Visual Conditions 79
5.3 Spatial Dynamics of Proprioceptive and Visual Error Correlates 85
6 FUTURE DIRECTIONS 86
BIBLIOGRAPHY 88
APPENDICES 95
Appendix A: Averaged Behavioral Response 95
Appendix B: Averaged Evoked Response 109
Appendix C: Current Source Density Profiles Across ROI's 116
Appendix D: Functional Activation of ROI's 122

LIST OF FIGURES

Figure 3.1: Experimental trial sequence of EEG experiment ……25

Figure 3.2: Proprioceptive trigger circuit diagram ……28

Figure 3.3: Visual trigger circuit diagram …….29

Figure 3.4: Motor torque delay…… ……..30

Figure 3.5: Overview of EEG setup ……..35

Figure 3.6: Overview of EEG and MRI experimental analysis …….. ..38

Figure 3.7: 3D reconstruction of scalp and cortical models ……. 42

Figure 3.8: Overview of cortical source analysis ……..47

Figure 4.1: Behavioral wrist responses in proprioceptive trials …….…….. 50

Figure 4.2: Behavioral cursor responses in visual trials ……..……. 51

Figure 4.3. Grand subject evoked potentials in visual and proprioceptive trials ……...……55

Figure 4.4: Current source density in bilateral BA 4 for proprioceptive and visual trials …….58

Figure 4.5: Current source density for left parietal BA's 5, 7, and 40 ……..… 59

Figure 4.6: Temporal dynamics of visual and proprioceptive error processing ……..... 66

Figure 4.7: Functional activation across proprioceptive ROI's……..68

Figure 4.8: Functional activation across visual ROI's ……...……69

Figure 4.9: Spatial localization of proprioceptive and visual sources ……...……71

Figure 4.10: Mahalanobis distances across proprioceptive and visual centroids. …….72

LIST OF TABLES

Table 4.1: Task-related source onset times (mean ± SE) for proprioceptive and visual ROI's across subjects …….65

LIST OF ABBREVIATIONS

AC	Anterior commissure
ACC	Anterior cingulate cortex
AIP	Anterior intraparietal area
BA	Brodmman area
BEM	Boundary element method
CSD	Current source density
DAQ	Data acquisition
EEG	Electroencephalogram
EOG	Electrooculogram
E_p	Proprioceptive error
ERP	Event-related potential
E_v	Visual error
fERN	Feedback error-related negativity component
fMRI	Functional magnetic resonance imaging
FOV	Field of view
IH	Interhemispheric line
LIP	Lateral intraparietal area
M1	Primary motor cortex
MEG	Magnetoencephalography
MIP	Medial intraparietal area
MNE	Minimum Norm Estimation
MRI	Magnetic resonance imaging
N100	Negative EEG peak at 100 ms
OAR	Ocular artifact rejection

P300	Positive EEG peak at 300 ms
PC	Posterior commissure
PPC	Posterior parietal cortex
PRR	Parietal reach region
ROI	Region of interest
SE	Standard error
SMA	Supplementary motor areas
SNR	Signal-to-noise ratio
VEOG	Vertical electrooculogram
VIP	Ventral intraparietal area

1 INTRODUCTION AND SPECIFIC AIMS

Error signals play an integral role in sensorimotor adaptation to rapid changes in environmental loads and task goals to encourage efficient motor planning and smooth limb coordination. Although the cerebellum, parietal, and premotor cortices have been implicated as playing an important role in visuomotor control processes, the specific region(s) within the brain that process error signals during goal-directed movement remain unclear. The objective of this research is to characterize the neural sources that underlie the computation of visual and proprioceptive error during goal-directed movement. With the recent finding that neural function scales with the magnitude of applied error (Anguera, Seidler, Gehring 2009), we test the hypotheses that i) sensorimotor errors during goal-directed movements are computed in regions of the brain that are distinct from the motor areas that utilize them; and ii) visual and proprioceptive errors are processed in separate regions within the posterior parietal cortex and are later combined to provide an integrated estimate of sensory error during tracking.

In the current study, the high temporal resolution of electroencephalography (EEG) was used to study the temporal dynamics of large scale neural activity associated with the computation and processing of visual and proprioceptive error. Specifically, EEG recordings were used to analyze the temporal sequence of activation of cortical sources (using source localization techniques in conjunction with MRI anatomical data) to determine whether sensory processing of visual and proprioceptive errors involve different cortical areas within PPC.

Accordingly, the specific aims of this project were to:

i. Design and implement an experimental paradigm to dissociate visual and proprioceptive error signals in a tracking task using an electromechanical robot.
ii. Use EEG to obtain high temporal resolution measurements of brain function during the experimental task.
iii. Use distributed cortical source modeling to characterize the cortical networks active during visual and proprioceptive error processing

2 BACKGROUND & SIGNIFICANCE

2.1 Motivation

Studies that have investigated the role of the brain in sensory error processing have either examined the temporal response of event-related potentials (Krigolson and Holroyd 2007), or the blood-oxygen level dependent (BOLD) response to externally-applied error (Suminski et al., 2007). When evaluated independently, either knowledge of the timing of ERP responses in EEG, or spatial maps generated in response to an event in fMRI, alone cannot determine how different areas of the brain function together in space ant time during sensorimotor error processing. Therefore, examining *both* the spatial and temporal dynamics of neural correlates during sensorimotor error processing would allow us to understand how the brain responds to error.

fMRI studies examining the differences in processing for proprioceptive and visual error have found similar areas activated in response to both types of error (Diedrichsen et al., 2005). However, due to its relatively poor temporal resolution, fMRI does not provide a measure of the sequence of activation across brain areas; thus, it is possible that although similar areas may be recruited, the cortical networks that mediate error processing for vision and proprioception may be different. In this study, we combined the high temporal resolution of EEG with distributed source modeling techniques to image the spatiotemporal dynamics of error processing in cortex to evaluate differences spatiotemporal processing of vision and proprioceptive error.

2.2 Types of Sensory Error

Multiple neural systems have been shown to be involved in the sensorimotor processing for *different types of error* during goal-directed movements. For example, a study by Suminski et al. (2007) observed differences in the neural correlates of *moment-by-moment* error and *trial-by-trial* error when applying torque perturbations to the wrist using a manipulandum (Suminski et al., 2007). They showed that a cerebello-thalamo-cortical network (including the precentral and postcentral gyri and inferior and superior parietal lobules) was involved in the online correction of moment-by-moment error or 'transient' error that resulted in discrete corrective adjustments to the reference wrist angle when stabilizing against perturbations during the trial. A separate group of cortical and subcortical areas, conversely, was activated in response to trial-by-trial error or 'persistent' error (including the posterior parietal cortex, prefrontal cortex, dorsal premotor cortex, and supplementary motor areas (SMA)), to monitor feedback performance and update performance goals over a longer timeframe.

Krigolson and Holroyd (2007) discovered a hierarchical organization of error processing involving different neural regions that responded to correcting '*low-level*' error versus '*high-level*' error (Krigolson and Holroyd 2007). To study different levels of error, the authors designed a manually aiming task wherein subjects used a joystick to place a cursor on a visual target while target position was perturbed in two types of trials: i) correctable trials that induced displacements in target position that could be corrected for by moving the joystick in the direction of the target; and ii) uncorrectable trials wherein the cursor position was unresponsive to displacements of the joystick thus preventing subjects from achieving the task goal. (The low-level error trials in Krigolson and Holroyd's study are similar to the moment-by-moment error trials in Suminski et al.'s study). Through EEG, Krigolson and Holroyd observed parietal

activation in response to low-level error (i.e. correctable error) whereas the frontal areas were involved in processing and evaluating high-level error (i.e. uncorrectable/uncorrected error). The authors believe the high-level error system is used to evaluate behavioral goals over a longer time frame.

Diedrichsen et al. (2005), additionally reported the involvement of separate areas in the processing of *'target'* and *'execution'* errors in a target tracking task using a robot (Diedrichsen et al., 2005). Similar to the study by Krigolson and Holroyd, subjects were asked to place a cursor on a target while displacements were either introduced in the target position (as target error – similar to the 'low-level' error condition discussed in Krigolson and Holroyd's study) or as visual rotations of cursor position (execution error). Through fMRI, the authors observed activation of the striatum and posterior superior parietal lobule during the processing of target error, while the cerebellum, motor cortex, and subregions of the parietal cortex were said to be involved in the processing of execution error.

Although these studies have investigated different classes of error, their results suggest that well-defined cortical and cerebellar networks are used to process different types of sensorimotor error. Section 2.4 outlines evidence supporting the roles of the posterior parietal cortex, cerebellum, and premotor, motor, and medial-frontal cortices in sensory error processing.

2.3 Brain Areas Involved in Sensorimotor Error Processing

2.3.1 The Posterior Parietal Cortex

Understanding of the function of the posterior parietal cortex (PPC) has evolved considerably over time: scientists initially considered it to be primarily a sensory association area, but studies have shown that damage to the PPC in humans can lead to hemispatial neglect

(Gentilini et al., 1989; Karnath, Niemeier, Dichgans 1998), ideomotor limb apraxia (Haaland 2000), and optic ataxia (Gréa 2002), that result in impairments in the sensory guidance of goal-directed movements. As a result, the PPC is now understood to play a primary role in sensorimotor transformation – that is, the transformation of sensory information encoded in an extrinsic coordinate system into an intrinsic representation of motor output used to successfully achieve a task goal. Lesion studies in human parietal cortex have enabled scientists to draw understanding of the visuomotor functions of the PPC. For example, damage to the PPC has been shown to result in more pronounced errors during reaching movements (Rondot, de Recondo, Dumas 1977), an inability to properly plan and execute movements, and increased difficulty in configuring the shape of the hand (e.g. to perform a grasping action) (Perenin and Vighetto 1988).

The PPC and Multisensory Integration

Neurophysiological research in the macaque monkey brain has revealed that neurons in the lateral intraparietal area (LIP), a subregion within the PPC specialized for saccadic eye movements, encode spatial information in retinotopic coordinates (Andersen, Essick, Siegel 1985) and can modulate their receptive fields by shifting the location of their receptive fields to a predicted location of visual input before a saccade is initiated (Duhamel, Colby, Goldberg 1992). Duhamel et al. (1992) proposed the early shift (of receptive field location for parietal cells) could be used to provide a continuously accurate and stable percept of visual space to enable smooth eye-hand coordination. Other studies report that LIP neurons also encode information such as eye position and the proprioceptive sense of head position in eye- and head-centered units to create a distributed representation of space in body-centered coordinates (Brotchie et al., 1995;

Mullette-Gillman, Cohen, Groh 2005). While LIP is specialized for saccadic eye movements, other subregions situated in the wall of the intraparietal sulcus of the PPC, are involved in movement planning for different types of goal-directed movement: medial intraparietal area (MIP) of the parietal reach region (PRR) in the monkey brain responds to reaching movements, ventral intraparietal area (VIP) is activated during target pursuit (Colby, Duhamel, Goldberg 1993), while anterior intraparietal area (AIP) encodes grasping movements (Cohen and Andersen 2002).

Recent experiments have discovered partially-shifted response fields between eye- and head-centered representations for neurons in the VIP (Duhamel et al., 1997) and between eye- and limb-centered representations for neurons in area 5 of the PPC (Buneo et al., 2002), which may suggest that the PPC plays a direct role in computing coordinate transformations between different frames of reference. Consistent with this understanding, studies have reported that subregions of the macaque PPC tend toward a particular sensory modality: areas 7a and LIP are primarily visual in terms of sensory input, area 5 primarily somatosensory, areas 7b, MIP, and VIP both visual and somatosensory, while a percentage of LIP and MIP neurons process auditory spatial information (Mullette-Gillman, Cohen, Groh 2005). Across the PPC, subsets of neurons have been found to respond to input that is either somatosensory, visual, or a combination of the two (Colby and Duhamel 1991), which suggests the role of the PPC in multisensory integration.

The PPC and Goal-Directed Movement

Several research studies have suggested that the PPC plays an important role in processing (Culham et al., 2003; Culham, Cavina-Pratesi, Singhal 2006; Diedrichsen et al., 2005) and correcting (Krigolson and Holroyd 2007) online sensory error during goal-directed

movements. Specifically, the PPC has been implicated in monitoring motor commands to correct for minor discrepancies in movement. Research suggests this evaluation process either stems from a forward model of control in which position and velocity movement parameters are estimated to initiate faster movements (Desmurget and Grafton 2000; Grafton et al., 2008; Wolpert and Ghahramani 2000); or a feedback-model of control wherein an efference copy of motor command is used to correct for moment-to-moment errors (Grafton et al., 2008; Gréa 2002; Krigolson and Heath 2004).

Within PPC, fMRI studies have shown there to be a lateralization of visuomotor function within the PPC during motor control tasks that is dependent upon the type of movement being performed – the left parietal cortex is associated with tool manipulation and usage, while the right parietal cortex is specialized toward the spatial processing of information and attention (Johnson-Frey, Newman-Norlund, Grafton 2005). A study by Wheaton et al. (2009) further indicates the left parietal cortex is dominant when planning, executing or suppressing a movement (Wheaton et al., 2009).

Areas 5, 7, and 40 of the PPC

Our experimental results reveal the relative contributions of areas 5, 7, and 40 in the human PPC. The following paragraphs, however, highlight their roles in sensory error and visuomotor processing in the monkey brain. Areas 5 and 7 represent the superior parietal and inferior parietal lobules of the monkey brain but both occur on human brain in the superior parietal lobe. Area 40 is located on the inferior parietal lobe of the human brain (Zilles and Palomero-Gallagher 2001).

Area 5 receives a large input from the somatosensory cortex, and in turn, projects to SMA and premotor cortex, both of which are involved in the processing of visuospatial information to plan and execute movements during goal-directed tasks (Halsband and Lange 2006). Area 5 has also been shown to be involved in the processing of execution error, that is, error induced through rotation of visual feedback or through force fields applied to the task-performing limb to alter movement dynamics (Diedrichsen et al., 2005). Here, area 5 showed a greater response to kinematic error (visual rotation) than to dynamic error (force field) despite evidence that the area responds primarily to tactile stimuli and is involved in *guiding* limb movements (Maimon 2006). Maimon and Assad (2006) discovered a slow ramp-up and ramp-down of neural activity in area 5 cells through single neuron electrophysiological readings while monkeys were trained to make a self-timed movement. The slow activity preceded the phasic discharge associated with the movement itself, and is believed by the authors to drive the initiation of movement. Mountcastle et al. (1975) additionally showed that area 5 neurons tended to be significantly activated when a limb was actively rotated but were insensitive to passive rotations about the same joint. Their study further observed that a small percentage of area 5 neurons discharged strongly only while the monkey made reaching movements or manipulated an object in a motivational task – the activity of these neurons was, however, uncorrelated to similar movements (using the same muscles) in which a target of motivational interest was not provided (Mountcastle et al., 1975). These ‘arm projection’ and ‘hand-manipulation’ neurons, as named by Mountcastle et al. (1975), also occur in area 7 of the PPC.

Unlike the neurons in area 5, area 7 of the PPC is driven largely by visual input and projects to premotor cortex and the frontal eye fields, an area involved in the control of eye movements (Robinson and Fuchs 1969). Area 7 neurons also encode properties for objects that

are of motivational interest during reaching or hand manipulation (Mountcastle et al., 1975), with the majority of activated neurons encoding properties contralateral to the moving limb (Hyvarinen and Poranen 1974). For example, Mountcastle et al. (1975) observed activation in area 7 neurons while monkeys visually explored the environment but discovered a stronger discharge of activity in area 7 when the monkey fixated on food (i.e. a motivational object). Different classes of area 7 neurons were responsive to different types of visual tasks, such as performing saccadic eye movements, visual fixation, smooth pursuit tracking of a target to be acquired, and some showed stronger activation when an object was presented in the immediate extrapersonal space (Mountcastle et al., 1975).

Anterograde and retrograde tracer studies performed in the macaque monkey brain (Faugier-Grimaud and Ventre 1989) show projections from area 7 neurons to various layers of the superior colliculus, which has been implicated in the sensory guidance of arm movements (Buneo and Andersen 2006; Glickstein 2000) and in multisensory integration (Meredith and Stein 1986); as well as to the pontine nuclei, which has been shown to be involved in visuomotor control (Stein and Glickstein 1992). A study by Ferraina et al. (1997) probed deeper into the functional role of area 7 neurons during reaching – in their study, single neuronal activity was measured in monkeys trained to fixate and reach toward peripheral targets (Ferraina et al., 1997). The authors discovered a population of neurons that responded only to eye movement, others to hand position and movement, and a majority toward a combination of visual and oculomotor sensory information. These observations are consistent with results in a similar study in which visual, somatic, and oculomotor sensory activity converged in area 7 neurons (Hyvarinen and Poranen 1974). The authors of this study proposed that area 7 is involved in integrating visual

information with the somatsensory input it receives from parietal area 5 to provide a integrated estimate of spatial perception to drive motor output.

The neuronal properties of area 40, however, have been much less documented in the scientific literature. In a MEG study, Nishitani et al. (1999) showed that both areas 7 and 40 were strongly activated during abrupt tracking changes in an eye-finger pursuit task where subjects tracked a moving visual target with their index finger and eyes (Nishitani et al., 1999), thus possibly suggesting their involvement in online error detection. This interpretation is consistent with the results of an fMRI study by Suminski et al. (2007) that demonstrated the activation of parietal areas, 5, 7, and 40, during a wrist stabilization task against random torque perturbations applied to the wrist (Suminski et al., 2007). These studies collectively suggest parietal areas 5, 7, and 40 are involved in the online processing of sensory error during goal-directed movements.

2.3.2 The Cerebellum

The cerebellum has been shown to play an important role in the sensorimotor coordination of multi-joint movements (Serrien and Wiesendanger 2000), and eye-hand visuomotor tasks such as reaching, pointing, and target tracking (Miall, Imamizu, Miyauchi 2000; Vercher and Gauthier 1988). The cerebellum has also been linked to the formation of internal forward models to predict and control sensorimotor activity (Imamizu et al., 2003) by comparing actual movement (from somatic receptor signals) to intended movement from signals received via pyramidal tract collaterals for the processing of error (Iacoboni and Dapretto 2006). Studies have shown the area to be activated during motor learning (Criscimagna-Hemminger, Bastian, Shadmehr 2010; Thach, Goodkin, Keating 1992) and have demonstrated its involvement

in the sensory processing of externally applied perturbations to correct for changes to online movement (Kitazawa, Kimura, Yin 1998; Nadig et al., 2010; Suminski et al., 2007). Cerebellar activation has also been shown to encode end-point position errors (i.e. at the end of a movement) (Kitazawa, Kimura, Yin 1998) rather than moment-to-moment error in order to evaluate and update behavioral performance and task goals when performance in a task is inadequate (Suminski et al., 2007).

2.3.3 The Premotor, Motor, and Medial-Frontal Cortices

Premotor, motor, and medial-frontal cortices are not known to play a direct role in online error correction, but work together with the PPC and other areas to plan, execute, and evaluate goal-directed movements.

The Premotor and Motor Cortices

Early studies concerning premotor cortex suggested its involvement in movement intention and awareness. Libet et al. (1983) measured brain activity during initiation of movements and discovered signals that were generated hundreds of milliseconds prior to consciously intending to move (which subjects self-reported as the time they felt an urge to move) (Libet et al., 1983). Researchers believe this early activity to be a product of a premotor-parietal circuit that is involved in structuring a movement plan before action (Haggard 2005). In fact, Naranjo et al. (2007) observed nearly simultaneous activation of the premotor and parietal regions from 140 ms during a reaching task before movement onset at 353 ms, further implicating the role of the premotor-parietal circuit in planning for reaching movement (Naranjo

et al., 2007). In goal-directed movements, the premotor cortex has been shown to encode movement parameters in hand-centered coordinates (Caminiti et al., 1991) unlike parietal areas that primarily encode movement vectors with respect to the eye and head (Andersen and Buneo 2002)(Andersen, Essick, Siegel 1985)(Andersen and Buneo 2002). In their study, Bernier et al. (2009) observed sustained premotor activity from 140 ms relative to stimulus onset until time of movement (at 365 ms) that occurred only in the somatosensory target condition which may indicate a preference toward integrating information of the arm and non-visual targets (reaching to a point of sensation on the hand) rather than visual targets (reaching to an LED on a screen). This could be due to the fact that premotor neurons have receptive fields that encode limb-centered representations and not retinotopic-centered representations of sensory information (Graziano, Yap, Gross 1994). Studies have shown that the primary motor cortex (M1) is also activated during movement preparation in conjuction with premotor areas (Zang 2003). M1 is known to control and execute goal-directed and skilled voluntary movements (Sasaki and Gemba 1987) through input from other cortical regions such as the primary somatosensory cortex, parietal area 5, basal ganglia, and cerebellum, all of which are involved in motor planning (Scott 2004).

The Medial-Frontal Cortex

Medial-frontal cortex has been shown to be involved in monitoring goal-directed movements and performance outcomes during motivational (i.e., reward-based) tasks (Debener et al., 2005), and is associated with detecting unfavorable outcomes to make necessary adjustments in behavior and learning (Garavan et al., 2002). The medial-frontal cortex also plays a role in error processing. Mars et al. (2005) found that activity in the medial-frontal cortex was

highly correlated with early phases of visuomotor learning (during which error was high) after which medial-frontal activity gradually decreased over the length of the trial (Mars et al., 2005). Additionally, the area has also been implicated in the processing of 'high-level' errors that cannot be corrected or are left uncorrected. In their study, Krigolson and Holroyd (2007) observed frontal-central activation 248 ms after a high-level error was introduced via target perturbation (Krigolson and Holroyd 2007). The study results suggest that the medial-frontal system has access to error information during the trial but only processes errors if they accumulate over time and transform into high-level errors. The authors postulate this could occur to train forward models used by the posterior parietal areas to correct for low-level errors and modify motor output.

2.4 Event Related Potentials in Sensory Error Processing: the N100, P300, and fERN

The N100, P300, and a feedback error-related negativity component (fERN), are three event-related potentials (ERP's), or evoked neuronal responses, associated with sensory error processing during goal-directed movements. The N100 has been studied largely in the auditory literature and is described as a prominent negative peak that occurs roughly 100 ms following stimulus onset (e.g. the presentation of an auditory tone). The N100 has also been found to occur in visuomotor tasks and is associated with an early discrimination of the stimulus (Naatanen and Michie 1979). In sensory goal-directed movements the N100 has been observed to peak 140 ms following target trajectory deviation when subjects tracked a moving visual stimulus (target) with a joystick while displacements in target location were randomly introduced throughout the trial (Krigolson and Holroyd 2007). For visual deviations the N100 was lateralized over the

contralateral visual cortex, which is consistent with other studies (Kasai et al., 2003; Pazo-Alvarez et al., 2004), and is believed to encode higher-order visual processing of the stimulus in the environment (e.g. stimulus location and/or magnitude). The N100 is evoked both in the presence of and absence of any changes in sensory stimuli (i.e. it appears both during the presentation of standard and oddball stimuli) (Polich 2007), which suggests that it may not necessarily encode the properties differentiating oddball stimuli from standard stimuli.

The P300, conversely, is a positively-peaked ERP that appears anywhere from 250 to 500 ms post-stimulus, and is largely thought to reflect a detection in the change of environment based upon a working memory of previous stimuli (e.g. the presentation of a high frequency tone following several low frequency tones), (Polich 2007). With each occurrence of a P300, the neural representation of the sensory environment is updated, and there is increase an in attention to the stimulus (Lindin, Zurron, Diaz 2005; Polich 2007), whereby more attention is given to larger detections of sensory change in the environment (Hill and Raab 2005a). Krigolson and Holroyd (2007) attribute the P300 to a low-level error evaluation process that results in a revision of the internal forward model in response to unpredictable events (Krigolson and Holroyd 2007). In their study, they observed the P300 component of the ERP over the parietal region 328 ms after deviations were applied to target trajectory. P300 components were seen to occur at roughly the same time in the premotor, motor, and parietal areas following the presentation of rarely occurring targets in a pointing task (McDowell et al., 2002); and in the parietal area following target trajectory deviations in a visuomotor tracking task (Hill and Raab 2005a).

The fERN appears as a negative ERP deflection that is maximal at the fronto-central electrodes. It has been localized to occur within the anterior cingulate cortex (ACC) (Swick and

Turken 2002) from 200 to 300 ms following the feedback of a subject's erroneous response (Miltner, Braun, Coles 1997). The fERN is elicited in response to high-level tracking errors, i.e. displacements in target trajectory that cannot be corrected for (Krigolson and Holroyd 2007), and is typically associated with error monitoring in the ACC to evaluate motor command feedback and determine whether system goals can be successfully achieved with the given resources (Holroyd and Coles 2002).

2.5 Visual and Proprioceptive Sensorimotor Processing

Studies have suggested the involvement of a bilateral fronto-parietal network in the multimodal integration of cross-sensory spatial representations (Felician et al., 2004; Galati et al., 2001). For example, Galati et al. (2001) observed activation of the same posterior parietal and frontal areas during two experimental conditions wherein subjects indicated the location of an object sensed visually and proprioceptively in relation to the midline of their body. The task inherently required them to perform an internal (body-centered) coding of stimulus position which was found to overlap for the two sensory conditions in the intraparietal sulcus, and precentral and superior frontal gyri (Galati et al., 2001). Additionally, Blangero et al. (2007) found that patients with parietal lesions that have optic ataxia, exhibit movement deficits both when reaching toward visual targets (targets placed within the contralesional visual space) or somatosensory targets (reaching toward the ataxic or contralesional limb), implicating PPC in the coordination of movement across sensory modalities (Blangero et al., 2007).

In order to uncover differences in visual and proprioceptive sensorimotor processing, Bernier et al. (2009) compared the spatiotemporal dynamics of movement planning toward visual and somatosensory targets (Bernier et al., 2009). The authors measured EEG recordings in

subjects that initiated movements, matched in direction and amplitude for the two conditions, toward LED targets (visual) or toward the sensation of vibrations applied to the contralateral limb (somatosensory). The areas involved in processing both types of sensory-driven movements appeared to be the same, with differences both in the degree of neural activation and in the temporal dynamics of activation across areas. Within the visual condition itself, Bernier et al. (2009) observed a temporal transition of reach-related activities from the parietal electrodes (187 ms) to premotor cortex (from 220 ms until movement onset at 317 ms), which is consistent with previous studies that have observed an early representation of movement encoded in an eye-centered reference frame within PPC (Andersen and Buneo 2002; Batista et al., 1999) followed by a limb-centered reference frame of movement within the precentral areas (Batista et al., 2007; Kalaska et al., 1997). The proprioceptive condition, on the other hand, showed early centrally-located activity at 55 ms followed by reach-related activation at the left premotor and sensorimotor areas beginning at 140 ms and 180 ms until movement onset (at 365 ms), and subsequently parietal activation at 200 ms.

2.6 Significance

The purpose of this study was to characterize the spatial and temporal dynamics of processing visual and proprioceptive sensory error during goal-directed movements and to determine the role of cortical areas involved in sensorimotor error processing: namely, the parietal cortex, the premotor cortex, the motor cortex, and the medial-frontal cortex. Although several studies have investigated the cortical areas activated in response to externally-applied error, most have been unable to clearly distinguish areas involved in the processing of error, per

se, versus processing for other aspects of the task not directly tied to the error (such as target motion in tracking tasks). Our study aimed to identify brain areas that were correlated with error and to understand the differences in error processing that occur when errors are sensed differentially via visual and proprioceptive pathways.

Overall this study will improve understanding of how error feedback for different sensory modalities are used in tandem to guide limb movement in a visuomotor task. For example, it is possible that separate estimates of error-related activity are first computed in sensory cortices (i.e. visual and somatosensory cortices) and later reconciled in the parietal and motor cortices to drive the motor response to the error. Alternatively, a unified multimodal estimate of limb state could be computed in parietal cortex prior to comparison to the desired state – this error signal could then be relayed to the motor cortex to move the limb accordingly. Differences in the spatiotemporal dynamics of error processing for vision and proprioception could suggest that error information pertaining to movement outcome is used independently across different sensory modalities.

This information could possibly be useful in designing rehabilitative strategies in stroke patients – for example, for stroke patients with lesions affecting the somatosensory cortex which could result in large movement errors, it would be useful to identify alternate pathways of error processing (say in the visual feedback pathway). Thus, by probing deeper into the fundamentals of error processing, we seek to not only further scientific understanding in how the brain responds to error, but also to inspire research in this area with the goal of improving rehabilitation strategies and the design of adaptive neuroprosthetic devices.

3 METHODS

3.1 Overview

The experimental aim of this study was to characterize the temporal and spatial properties of the cortical networks used to process visual and proprioceptive errors during goal-directed movement. A parametric experimental approach was used to identify neural sources whose activity was correlated with the magnitude of visual or proprioceptive errors applied during a motor tracking task. Electroencephalography (EEG) during the task was used in conjunction with subjects' structural brain anatomy and distributed source modeling to identify the cortical areas activated in response to online processing of visual and proprioceptive errors. Cortical sources correlated with the magnitude of visual or proprioceptive perturbation were separated into regions of interest (ROIs) on the cortical surface and the spatiotemporal patterns of activation were characterized to determine the cortical networks involved in the processing and online correction of sensorimotor errors.

3.2 Experimental Apparatus

The subjects' task was to track a moving visual target on a screen using a custom-made one degree of freedom robot. Wrist position, velocity and acceleration were measured and recorded on a trial-by-trial basis using a 19-bit optical encoder attached to the robot motor shaft. As part of the manipulandum, a Kollmorgen D061A brushless DC motor was used to apply user-controlled torques to the robot handle which were measured internally by a six-degree-of-freedom load cell (Model 67M25A-I40-A-200N12, JR3 Inc., Woodland, CA). Electrical and

mechanical safety switches in the robot were set at 35- and 40-degree limits respectively to automatically terminate the motor output and prevent subject injury. A target PC in the robot was used to collect real-time information of the robot handle's position and forces applied using data acquisition (DAQ) boards inside the computer chassis of the robot. The robot contained three DAQ boards: a PC104-DAS16JR/16 board and a VSBC-6 board, both with analog input and digital I/O channels; and a PC104-DAC06 board that was used to provide analog input to the motor of the robot. The target PC was interfaced with a host computer (used to display the task and write out the data) over an Ethernet connection and using the Simulink®, Stateflow®, and xPC Target™ toolboxes in MATLAB®. Simulink® was used to provide a graphical interface of the robot hardware, Stateflow® was used to control data flow between the robot hardware and host PC, and xPC Target™ was used to execute the Simulink® and Stateflow® models in real-time.

EEG data was collected using a Neuroscan™ SynAmps^2 system together with a 64-channel sponge-based electrode cap (with one additional bipolar channel used to capture eye movements). The SynAmps^2 system consisted of a power unit with an internal 1000-watt isolation transformer and an amplifier/head box unit that provided signal amplification, A/D conversion, trigger synchronization, electrode impedance measurement and internal calibration. A Hammond Manufacturing 171G step-down isolation transformer was used to remove additional power-line noise. Synchronization of EEG data was performed using a separate trigger cable connecting the proprioceptive (robot) and visual (host computer screen) stimulus output devices – see Figures 3.2 and 3.3.

3.3 Subjects

Seven healthy subjects with no neurological defects and normal or corrected-to-normal vision were recruited for the study (4 female; mean age 26.4 years). All subjects were right-handed and used their dominant hand to perform the tracking task. Written informed consent was obtained from each subject in accordance with the institutional guidelines approved by Marquette University and the Medical College of Wisconsin.

3.4 Experimental Design

In the EEG experiment, subjects were asked to place a user-controlled visual cursor on a circular target moving horizontally on a computer screen by operating a 1D robotic manipulandum. Target motion was modeled as Gaussian band-limited white noise (0.2-0.7 Hz). The position of the subject's wrist on the robot was yoked to a circular cursor shown on the screen with a 3.5:1 ratio between the wrist angle and visual angle of the cursor on the screen. The diameter of the cursor was set slightly larger than the diameter of the target to allow subjects to track the target by placing the cursor directly over the target. During the tracking task, external displacements of the wrist (Proprioceptive trials) or the cursor (Visual trials) were applied to create a positional error between the target and cursor/wrist position. The perturbation sequence and delays used are discussed in Section 3.4.1.

The neural evoked response to the error measured via EEG was analyzed following the onset of each positional displacement to characterize the spatiotemporal differences in cortical activity resulting from positional errors sensed proprioceptively (Proprioceptive trials) and visually (Visual trials). Previous studies have shown that neural activity scales with the

magnitude of perturbation applied (Anguera, Seidler, Gehring 2009). Here we made use of this phenomenon to dissociate error-related activity from noise, by characterizing EEG activity across five levels of displacements (ranging from approximately 0.3 to 20.1 degrees of visual angle displacement on the screen). The following sections discuss the two types of trials presented to the subjects: Proprioceptive and Visual.

3.4.1 Trial Structure

A total of 15 runs in each condition (Visual and Proprioceptive) were presented per subject. Each run lasted for 3.5 minutes and consisted of 50 trials (i.e. perturbations) that were presented in 5 blocks of 10 trials each. At the end of each block, the robot handle was brought to the home position (center of the screen) with a 1 minute rest period between blocks. This was done to minimize baseline drift (i.e. the drift in the proprioceptive sense of the robot handle relative to the home position), and prevent muscle fatigue. An illustration of the experimental trial sequence is shown in Figure 3.1.

In Proprioceptive trials position displacements were induced using force perturbations (Levels 1-5: 0.3 Nm, 0.5 Nm, 0.7 Nm, 0.9 Nm, 1.1 Nm) applied to the wrist by the handle of the robot while in Visual trials position displacements were presented by shifting the visual location of the cursor on the screen. Figure 3.1 C shows a sample Proprioceptive and Visual run sequence. Proprioceptive and Visual perturbations were selected to produce displacements that were matched in magnitude for the two conditions across perturbation levels (see Sections 1.3.2 and 1.3.3). Perturbations were either applied in the direction of the target motion or in the direction opposite to the target motion. Each block was presented with an equal number of perturbations in both directions and an equal number of perturbation levels to keep the overall

mean displacement to zero. Specifically, each block contained 5 perturbations (Levels 1 to 5) to the right of target motion and 5 perturbations (Levels 1 to 5) to the left of target motion. Trial order was randomized within subjects and across runs to control for possible bias in the EEG response towards a particular sequence of perturbation levels. Visual and Proprioceptive runs were interleaved over the experiment to ensure that the subject properties (e.g. attention to the task, muscle fatigue) were not compromised nor biased toward any particular condition in the experiment. Robot data (wrist position, target position, cursor position) was transferred from the robot to the host computer and saved between runs. Data was saved in units of volts and was converted to degrees of wrist angle in the analysis by using a conversion factor of 13.71. The specific structure of Proprioceptive and Visual perturbations is described below in Sections 1.3.2 and 1.3.3.

3.4.2 Proprioceptive Trials

In Proprioceptive trials, external force perturbations were applied to the wrist handle at pseudo-random intervals throughout the tracking task. Force perturbations (100 ms each) were applied to induce a discrepancy between the target position on the screen and the subject's wrist position on the robot. Subjects were asked to correct the perturbations (by bringing the wrist back to the target position) and continue tracking the target between perturbations. Visual feedback of the cursor position was not provided; only the target was displayed on the screen during Proprioceptive trials. Thus, subjects were required to rely on their proprioceptive sense of wrist position on the robot in order to track the target accurately. Each force perturbation lasted 100-ms (see Figure 3.1 C), and the trial-to-trial interval between perturbations was set randomly

between 2-5 s to prevent the subject from anticipating the forces, and also to allow sufficient time for the error (i.e. the positional difference between the target and cursor) to return to baseline between perturbations. Force perturbations were applied at five levels; 0.3 Nm, 0.5 Nm, 0.7 Nm, 0.9 Nm and 1.1 Nm (Levels 1 – 5 respectively), (corresponding to 0.45, 5.74, 9.68, 15.33, and 19.7 degrees of displacement for Subject MD9904 shown in Figure 4.1).

3.4.3 Visual Trials

In Visual trials, position displacements were presented as a constant offset in the cursor position to ensure that subjects actively corrected for the induced error. Preliminary tests showed that subjects quickly learned they did not need to initiate a correction if impulse perturbations were used since the cursor would return to its correct position. Thus, in order to force subjects to actively correct for the induced visual error between the cursor and target locations, visual perturbations were presented as constant visual displacements at five levels (e.g., Figure 3.1 C). The levels of visual displacement were matched in magnitude to the levels of displacement in the Proprioceptive trials to ensure that the same level of error was applied in both conditions. Displacements for the five error levels were determined prior to the experiment by measuring the average displacement in cursor position induced by the five force perturbations in a separate series of tracking tests. Although visual feedback of the cursor was not shown in these trials, the equivalent cursor location associated with the subject's wrist position was measured by the robot and processed offline. In each trial the cursor position was subtracted from the target position to determine the instantaneous position error.

Overall EEG Experiment

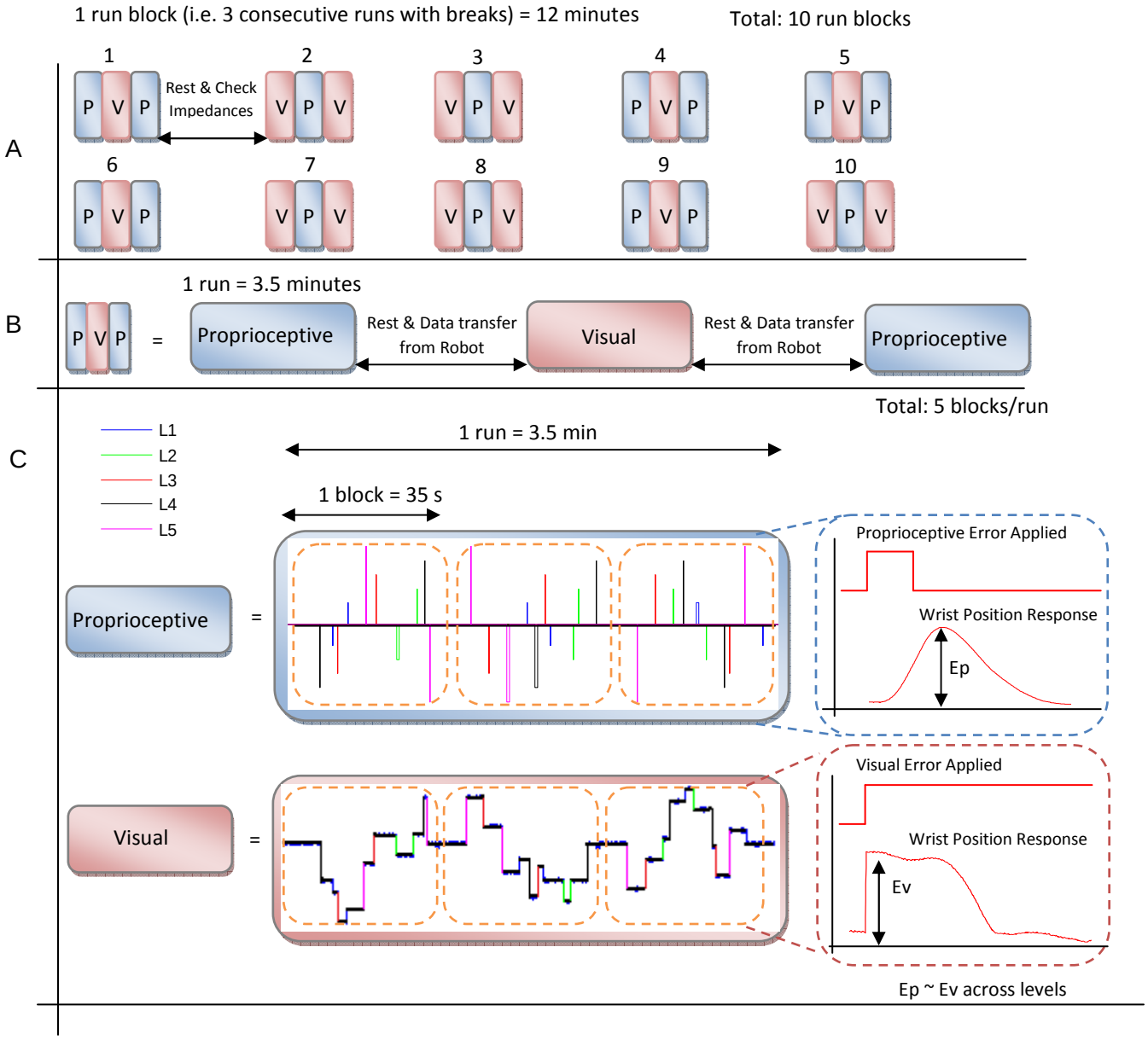

Figure 3.1: Experimental trial sequence presented to subjects during the tracking experiment. (A) Proprioceptive (blue) and Visual (red) runs (15 each) interleaved over the experiment. Electrode impedances were checked after a sequence of 3 runs while subjects rested to prevent muscle fatigue. (B) Example sequence within a run block (3.5 minutes in duration). Data was transferred from the robot to the host computer after each run. (C) shows a subset of 50 Proprioceptive (blue) and Visual (red) trials presented in 5 blocks per run. Subjects rested for approximately one minute between blocks during which the robot handle was brought to the home position. Each block contained 10 trials with 2 trials per level (1 in each direction so the overall mean displacement was zero). Visual trials were presented as continuous offsets rather than 100-ms impulse perturbations as in Proprioceptive runs to ensure subjects initiated a correction toward cursor displacements. On the right, a snapshot of a sample behavioral response is seen to a single Proprioceptive or Visual perturbation. Although the error profiles appear different across conditions, the magnitude of the error (E_p and E_v) was matched across levels (see Sections 1.3.2 and 1.3.3 respectively). The specific amount of force to be applied was

determined in the following way: preliminary subjects reported that a force of 0.3 Nm was the minimum torque applied to the handle for which they could feel the handle moving (i.e. the displacement caused by the perturbation was larger than the stiction of the robot and the compliance of the subjects' wrist). The maximum torque (11 Nm) was identified qualitatively as the upper bound for which subjects self-reported that they could comfortably perform the experiment.

The absolute position error was then averaged across trials (by level) from perturbation onset to 1s following onset to determine the peak displacement in cursor position for each level (see Figure 3.1 C for the behavioral wrist response in Proprioceptive trials).

3.4.4 Triggering

A trigger cable was passed from the Neuroscan™ amplifier to the EEG-recording computer to 'flag' the EEG data on each trial. Flags were registered on the EEG plot by a number marker (see Figure 3.5: 'Top View') and were used to determine the time of perturbation onset. Proprioceptive trials were flagged using Simulink® to control a digital output port on the PC104-DAS16JR/16 DAQ board in the target PC. A digital signal was sent to the digital port each time a command torque signal (i.e. a force perturbation) was sent to the analog output port of the PC104-DAC06 board controlling the motor (see Section 1.1). This ensured that a trigger signal was generated at the same time the motor was signaled to apply a torque to the wrist. Torque commands delivered by the host computer were applied to the wrist with an average delay of 13-ms (see Figure 3.4). A DB25 port cable was used to connect the DAQ output from the PC104-DAS16JR/16 board to the Neuroscan™ SynAmps^2 system (see Figures 3.2 A & B). In order to register an input as a trigger signal, Neuroscan™ required a clean 5 V square pulse.

Due to inherent motor noise in the DAQ output, a Schmitt Trigger circuit was used to output a clean trigger pulse to Neuroscan™ and register the onset of each perturbation (see Figure 3.2 C).

Visual trials were flagged using a photodiode circuit to detect the onset of visual perturbations using a small illuminated square displayed on the bottom right corner of the screen. A photodiode, encased in a dark circular box, was taped to the display screen such that the photodiode was in direct contact with the illuminated square. The encasing was used to ensure that external lighting was not sensed by the photodiode and to hide the illuminated square from view by the subject. The illuminated square was black in color but briefly flashed to white (for 200 ms) at the onset of each cursor displacement in Visual trials. Due to its higher luminosity, the white square resulted in a higher voltage output from the photodiode that was matched in time to the visual onset of the displacement on the screen. Two non-inverting amplifier circuits were used to amplify the output gain of the photodiode to 5V and the resulting output was passed to the Neuroscan system using channel 7 (digital input pin) on a DB25 port cable (Figure 3.3).

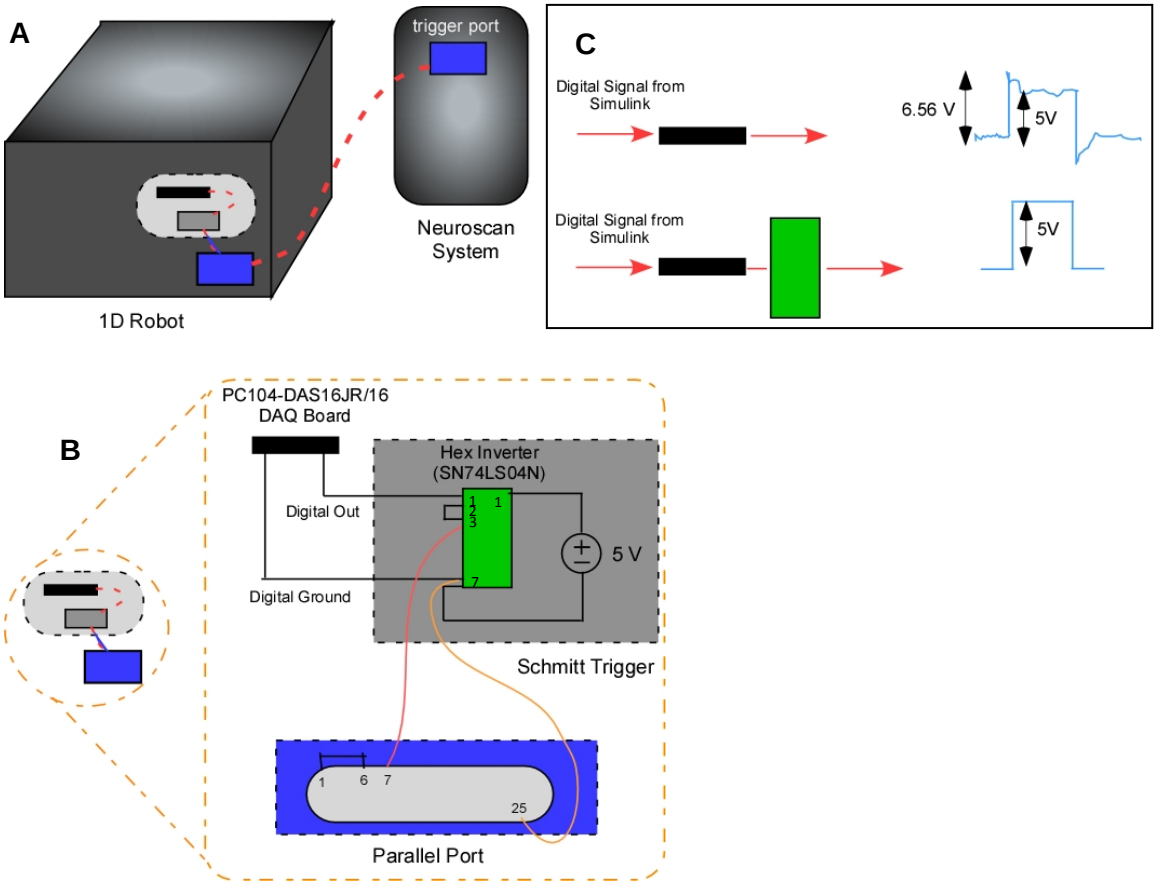

Figure 3.2: Proprioceptive trigger circuit. A schematic illustration of the proprioceptive trigger circuit (light gray box marked by dashed black lines) is shown in (A). The black bar represents the digital I/O DAQ board, which is connected to the Schmitt Trigger (medium gray box), which is in turn connected to a DB25 port (blue box) attached to the robot casing. A DB25 port cable was used to connect the DAQ output from the robot to the trigger port of the Neuroscan™ SynAmps[2] system. (B) An overview of the circuitry between the DAQ and Neuroscan™. The digital output and digital ground signals were passed from PC104-DAS16JR/16 to a hex inverter (part SN74LS04N). A Schmitt Trigger circuit was used to output a 5V square pulse every time the input signal exceeded a threshold (set to 5 V at pin 14 of the hex inverter). Output at pin 4 was passed to channel 7 of the DB25 port (a digital input channel in the Neuroscan™ trigger port) and the digital and power ground signals were referenced to the Neuroscan™ ground at pin 25 of the DB25 port. Channels 1 through 6 of the DB25 port were connected to ground to prevent noise leakage from the unused digital I/P channels. (C) Due to high baseline noise, reading the output from the DAQ board generated a variable 5V square pulse, which was too noisy to be recognized as a trigger signal by Neuroscan™. With the use of the hex inverter (green), a clean 5V pulse was generated whenever a digital signal of 1 was received by the DAQ.

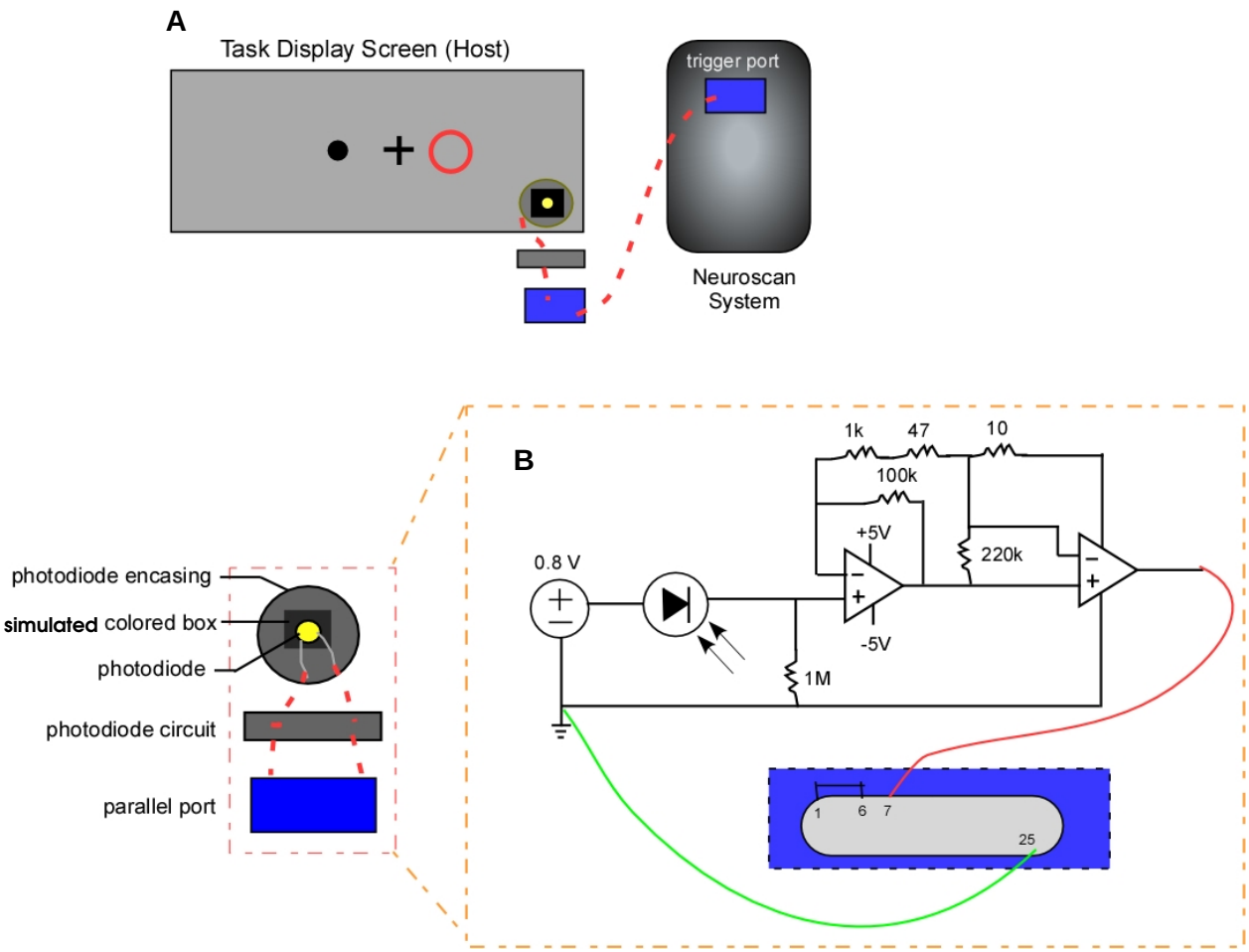

Figure 3.3: Visual trigger circuit. Visual triggers marking the timing of a cursor displacement were detected using a photodiode circuit. (A) Schematic diagram illustrating the visual trigger presented on the screen. A photodiode was placed in direct contact with the illuminated square region of the screen. The square briefly flashed to white at perturbation onset, resulting in a voltage output to the Neuroscan system. (B) Schematic of the photodiode circuit. Two op-amps were used to amplify the photodiode gain to 5 V, which was then passed to a DB25 port cable (channel 7 for digital input and channel 25 for Neuroscan ground).

Measuring Motor Delay for Proprioceptive Trials

In order to account for the delay associated with the generation and *application* of the torque to the wrist (and distinguish it from proprioceptive trigger onset – the time at which a command torque was *sent* to the motor), the motor delay of the robot was measured. The handle of the robot was locked using three physical constraints (as similarly shown in Figure 3.5), and the torque applied to the handle of the robot was measured during 100 force perturbation trials (i.e. 5 levels with 20 trials/level). Torque responses were averaged across all trials/levels. Figure 3.4 shows the timings of the average measured torque relative to the time the command torque was sent.

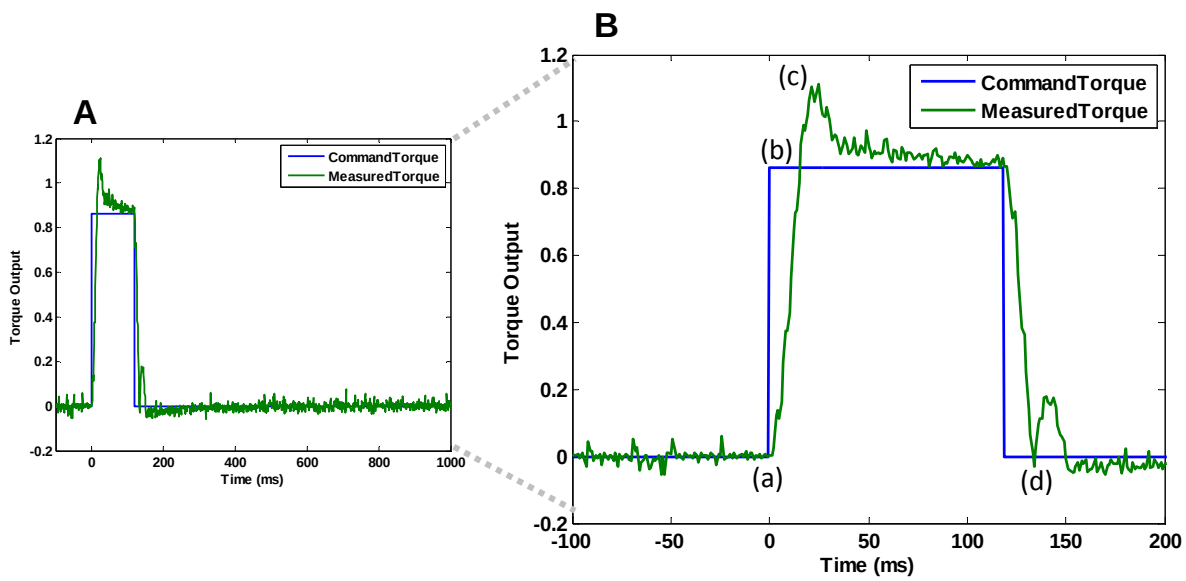

Figure 3.4: Motor torque delay. Applied torques measured by the load cell at the handle ('Measured Torque') and command torque signals sent to the motor ('Command Torque'). (A) Average values for measured and command torque across 100 trials (20 trials/level). (B) Close-up of (A) to show the delay in onset. (a) – (d) indicate delays: (a) τ_{onset} , the time at which the measured torque was significantly different from noise (>4σ); (b) $\tau_{commandTorqueMax}$, the time at which the measured torque equaled the the command torque; (c) τ_{peak} , the time at which

measured torque reached its maximum value; and (d) $\tau_{baseline}$, the time at which measured torque returned to baseline (<4σ).

To measure the delays τ_{onset} , $\tau_{commandTorqueMax}$, τ_{peak} , and $\tau_{baseline,}$ the standard deviation of the measured torque from -100 ms to 0 ms (i.e. baseline distribution or 'noise') was measured. Subsequent values of measured torque (0 ms – 1000 ms) were defined as significant in they were greater than four standard deviations of the baseline torque. Across trials, latencies in torque application relative to the torque signal were:

τ_{onset} : 4 ms
$\tau_{commandTorqueMax}$: 17 ms – 4 ms (onset) = 13 ms
τ_{peak} : 26 ms – 4 ms (onset) = 22 ms
$\tau_{baseline}$: 135 ms – 4 ms (onset) = 131 ms

To account for the motor delay in he analysis of the Proprioceptive condition, **13 ms** (i.e. $\tau_{commandTorqueMax}$) was chosen as a conservative measure of the motor delay**.**

The following sections describe the experimental setup that was used to collect EEG and MRI data.

3.5 Experimental Setup and Protocol

Prior to the EEG experiment, several steps were taken to prepare the electrode cap and calibrate the system:

i) Preparation of the EEG electrolytic solution: 1 packet of proprietary electrolyte powder was mixed with 56 ml of distilled water and mixed until dissolved. The electrolytic

solution was used to increase the conduction of brain signals over the scalp and allow better contact of the EEG cap sponges over the head.

ii) Insertion of sponges in all EEG channels on the EEG cap. A medium-sized EEG cap was used for all subjects.

iii) EEG calibration: the EEG cap was internally calibrated by attaching a shorting plug to the Neuroscan™ head box and running the calibration process through the software. The purpose of the calibration was to scale potential values to microvolt units and make software adjustments across channels to compensate for small differences in amplifier gains.

Subjects participated in three separate experimental sessions: a) a *digitization* session, 2) an *EEG experimentation* session, and 3) an *MR Imaging* session. Sessions I and II took place consecutively at Cramer Hall, Marquette University, and Session III was performed at the Medical College of Wisconsin separately. The details of the three experimental phases are provided below.

A) Digitization

During digitization, the 3D locations of the EEG sensors on the subjects' scalp were measured to account for intra-subject differences in scalp size and the resulting stretching properties of the cap over the head. Subjects were seated in the Falk Rehabilitation Laboratory at Cramer Hall in a calibrated workspace region within view of an optical imaging system. An Optotrak 3020 motion analysis system (Northern Digital, Inc., California) was used to measure the 3D locations of the EEG electrodes on the subject's scalp using an optical imaging camera

and digital probe embedded with infrared reflective markers. Subjects were positioned facing away from the Optotrak system with their heads resting on a chin-rest table such that the backs of their heads were visible to the camera. The chin-rest was used to reduce variation in the measured positions by minimizing the subject's head movement. The tip of the digital probe was held over each electrode (for 10 s to ensure stable recordings) such that a minimum of three (out of six) markers were visible to the cameras. The origin of all electrode positions was referenced (by default) to a point along the bottom-left corner of the workspace. All electrode positions (in centimeters) within the 3D space were recorded in one continuous recording along with three additional fiducial points – the nasion, the left preauricular, and the right preauricular. The fiducials were used to co-register the electrode locations to the 3D coordinate system used to define the BrainStorm surface space (i.e. the locations of the cortex and scalp estimation models in BrainStorm (University of Southern California)). Electrode location data was collected at 50 Hz and electrode positions measured as the average location in the x-, y-, and z-planes measured over the last 6 seconds of each position measurement.

B) EEG Experiment

Following digitization, subjects were seated in a height-adjustable chair facing a computer screen that was used to display the task. The 1D robot was placed on their hand-dominant side and subjects were asked to place their arm on the robot and grip the handle of the manipulandum (see Figure 3.5). Positional adjustments of the robot were made until subjects were able to grip and control the robot comfortably, after which, the robot wheels were locked to minimize movement of the robot during the experiment. An opaque screen was placed alongside

the subject between the robot and the subjects' task-performing arm and chest to prevent direct visual feedback of the subject's wrist position during the task.

Prior to testing, subjects practiced tracking the target using the cursor to gain familiarity operating the robot. While subjects practiced the task, the EEG electrodes were each hydrated with approximately 0.13 ml of electrolyte solution. Additional electrodes were taped above and below the left eye to capture blink artifacts and on the right and left mastoids (behind the ears) as EEG references. The electrode impedances were monitored and minimized to 5kΩ in two ways: i) by injecting sufficient solution to ensure proper contact with the scalp, and ii) by gently massaging the electrode on the scalp to remove any interference of hair between the scalp and sponge. For subjects that displayed high electrode impedance due to loosened contact of the electrodes on the scalp, an additional porous gauze-net was strapped over the head to encourage stronger contact between the cap and the scalp. The hydration process required 45 minutes on average. An illustration of the EEG setup is shown in Figure 3.5.

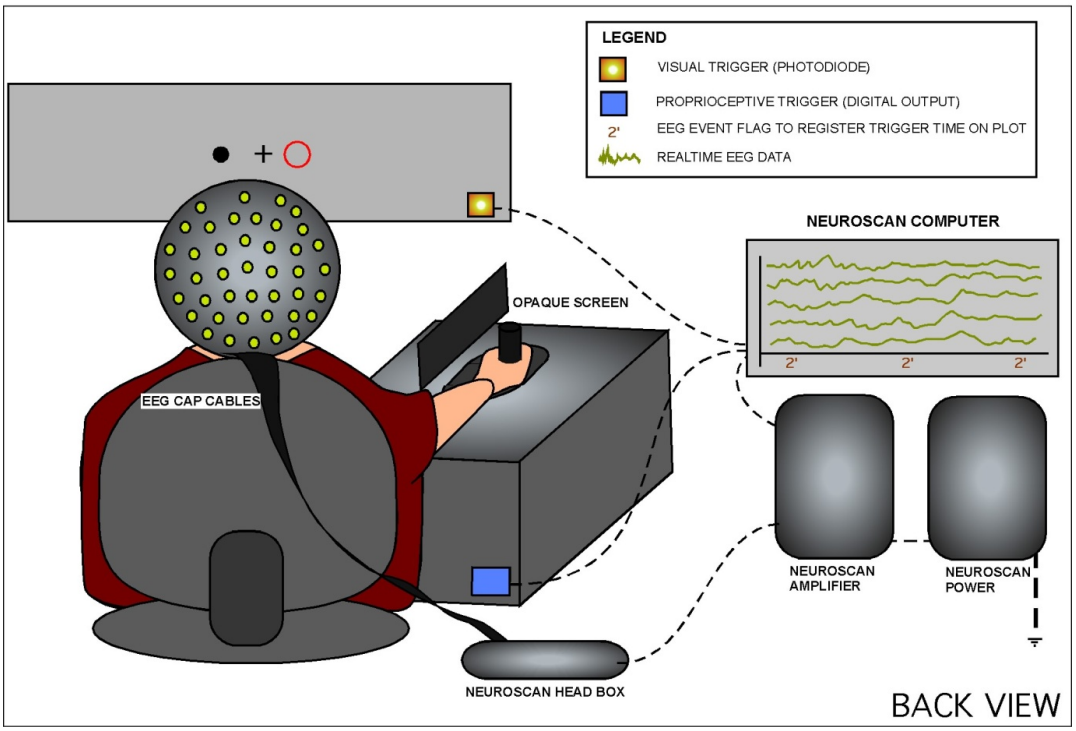

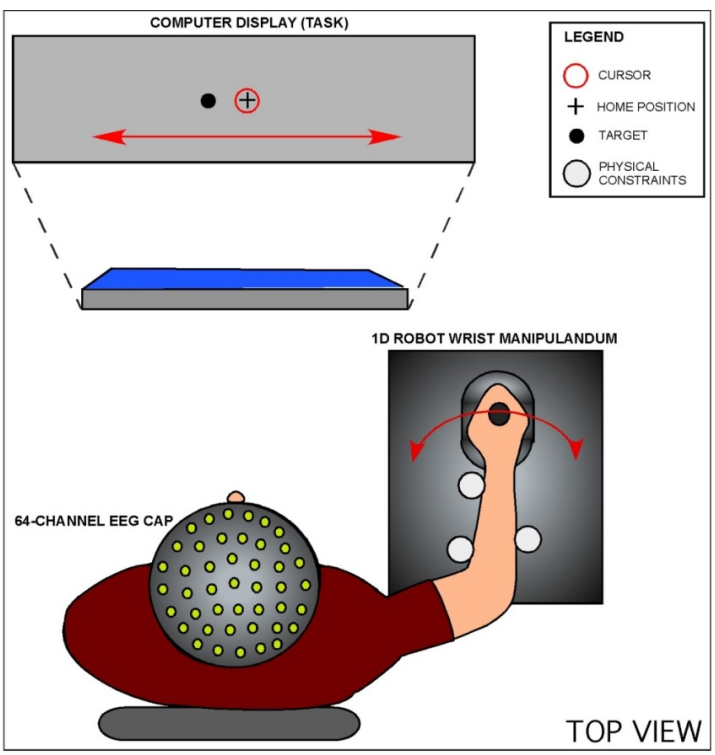

Figure 3.5: Overview of EEG setup. The top figure shows the back view of subjects performing the tracking task displayed on a screen using the 1D wrist robot. A moving target (black dot), a cursor representing their wrist position in Visual trials (red circle), and a marker to display the home position (black crosshair) were displayed on the screen. Visual (yellow patch on screen) and Proprioceptive (blue square on robot) trigger circuits were used to mark the onset of perturbations across trials. EEG data was acquired from 64 electrodes positioned in a cap on the subject's head. An opaque screen was used to block visual feedback of the wrist position on the robot.

The bottom figure shows the top view of the experimental task. The angular rotation of the wrist was translated to a 1D horizontal movement of the visual cursor on the screen. The subject's arm position was locked on the robot using three physical constraints to ensure subject's used their wrist to perform the tracking task (while stabilizing the positions of their shoulders and elbows).

EEG data was collected at 5k Hz and saved after each run. Measured EEG signals were automatically low-pass filtered at 1000 Hz by Neuroscan™ to prevent aliasing of higher frequency signals. Behavioral data for wrist position, target position, cursor position, and robot-applied and subject-exerted torques were measured at 1000 Hz by the target PC in the robot and saved after each run. In order to synchronize EEG activity with the behavioral response, EEG data was down-sampled to 1000 Hz (after low-pass filtering: see Section 3.6.2) and both sets of data were analyzed relative to perturbation onset (with timings defined by the trigger flags).

C) The MR Imaging Session

During the MRI imaging session a 3-Tesla MR scanner was used to obtain a 3D anatomical MRI from the subject. The anatomical data was subsequently used to create 3D cortical and outer skull models as part of the distributed source analysis (Section 1.6.3). Prior to the scan, subjects were separately consented and were asked to complete a MR-screening form to foresee any complications that could result while in the scanner (e.g. injury in the scanner due to metallic objects in or on the body). They were then asked to rest within the scanner bore in a supine position with their heads locked firmly in a head coil. Sponge blocks were added to the sides of their head to minimize movement during the MRI scan. Subjects were given ear plugs to be worn throughout the scan to minimize the risk of ear damage due to scanner noise. During the scan subjects were given an emergency squeeze ball that allowed them to terminate the scan at any point should they feel uncomfortable or unfit. Two scans were performed: 1) a 2-minute localizer scan to ensure the subject's head was centered within the field of view (FOV) without significant rotation; and 2) a 8- to 10-minute high-resolution full-volume structural MR anatomy scan using fast SPGR imaging to image the brain using axial, saggital, and coronal slices. A total

of 172 image slices were obtained with 1-mm thickness. The 3-T scan was acquired using a 8-channel head coil with the following parameters: TE 4 ms, TR 9.7 ms, FOV 24 cm, 256 x 244 image matrix, 12° flip angle.

3.6 Analysis Methods

3.6.1 Behavioral Data

Error in position, velocity and acceleration were measured across trials and within conditions following a Proprioceptive or Visual perturbation. Positional error in proprioceptive trials was measured as the absolute difference between the target and equivalent cursor location of the wrist position on the robot (for Proprioceptive trials) or between the target and cursor position on the screen (for Visual trials). Epochs were measured from -100 ms to 1 s after perturbation onset as measured with respect to the respective triggers timings. Epochs were measured out to 1 s to ensure that the entire behavioral response to the displacement (from error onset back to baseline) was captured for both Proprioceptive and Visual trials. Epochs were averaged trial-wise and low-pass filtered at 30 Hz with a 4th order Butterworth (zero-phase) filter. Velocity and acceleration were measured as the first and second derivatives of the positional response and all measurements were multiplied by a factor of 13.71 to convert internal voltage measurements into equivalent degrees of wrist angle.

3.6.2 EEG Data

The EEG analysis was performed using the following steps:

EEG Pre-processing: Vertical eye movement artifacts were removed using the Ocular Artifact Rejection (OAR) algorithm in Neuroscan™. The OAR uses a regression analysis and artifact averaging method validated by Semlitsch et al. (Semlitsch et al., 1986) that constructs an average artifact response based upon the highest movement potentials in the VEOG channel. The algorithm then estimates the covariance of the averaged artifact response with the EEG channels and subtracts the electrooculogram (EOG) from the EEG on a sweep-by-sweep, point-by-point basis.

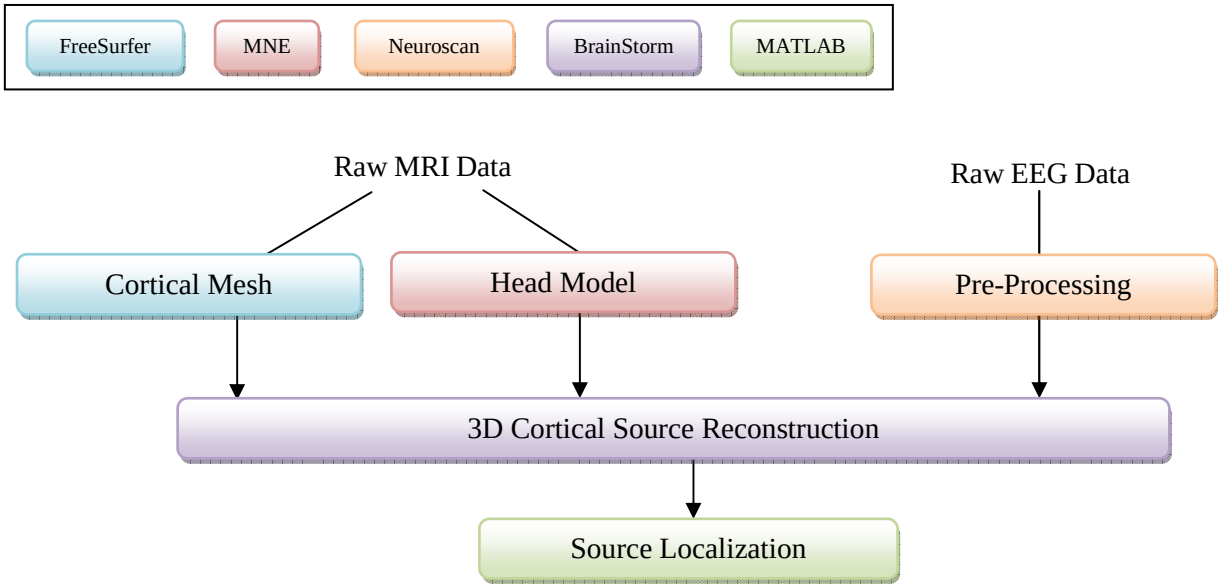

Figure 3.6: Overview of the experimental analysis performed on the raw EEG and MRI data. Raw MR images were converted into 3-D cortical and head models, using FreeSurfer and MNE respectively, to reconstruct cortical source currents on a single-subject anatomy. The raw EEG data was pre-processed in Neuroscan before being imported into Brainstorm to generate current source density (CSD) profiles across perturbation levels for each condition. The CSD profiles were then analyzed in MATLAB® to determine the cortical sources that were significantly correlated with error across levels.

On trials contaminated with high frequency noise in the VEOG channel (possibly due to loosened contact of the VEOG electrode(s)), a low-pass 4th order zero-phase filter was applied at 10 Hz to obtain a clean blink signal. The filtering enabled the algorithm to better distinguish true blink signals from noise. The VEOG channel was then removed from further analysis and the remaining 64 EEG channel output (i.e. eye artifact corrected data) was imported into MATLAB®.

Preliminary analysis showed that the filtering algorithms in Neuroscan™ were not sufficient to completely remove the 60 Hz power line noise and its harmonics. Thus, all subsequent filtering was performed in MATLAB®. The EEG signals at each electrode were low-pass filtered at 100 Hz, and band-stop filtered from 58 to 62 Hz, 118-122 Hz, and 238-242 Hz (6th order zero-phase Butterworth) to remove effect of the 60 Hz noise and its harmonics.. The data was then imported back into Neuroscan™ and epoched from 100 ms *before* to 1000 ms *after* displacement onset. Epochs were then sorted according to trial type (i.e Levels 1 – 5) and the baseline signal was measured from -100 to 0 ms.

The mean amplitude over the epoch length (i.e. -100 ms to 1 s) was subtracted from the signal on a point-by-point basis to remove large DC offsets that occurred over the entire trial. This was done to ensure that the artifact rejection algorithm only removed epochs that contained actual noise and not true signals masked by a large DC signal. Epochs containing voltages outside a set threshold of ± 50 uV were automatically rejected from further analysis to prevent particularly noisy epochs from lowering the signal-to-noise (SNR) ratio of the averaged EEG response. Two frontal electrodes, F1 and F2, were generally selected as artifact rejection electrodes across subjects (i.e. epochs would be rejected if the activity in F1 and F2 fell outside the set threshold) unless they showed high impedance in which case other frontally-located

electrodes with lower impedances were used. In order to remove offsets in the pre-stimulus mean (i.e. -100 ms to perturbation onset at 0 ms), the mean DC offset in the pre-stimulus interval of -100 to 0 ms was subtracted from the epoch length (0 ms to 1 s) on an epoch-by-epoch basis. For each perturbation level, all trials were averaged in each condition to obtain a series of average evoked response (Levels 1-5) for both Proprioceptive and Visual trials. The averaged epochs were then imported into BrainStorm for further analysis.

3.6.3 Cortical Source Reconstruction

In order to project the EEG data onto the cortical anatomy, structural MRIs were used to generate 3D cortical and scalp models using FreeSurfer (http://surfer.nmr.mgh.harvard.edu) and MNE (http://www.nmr.mgh.harvard.edu/martinos/userInfo/data/MNE_register/index.php). The raw individual MRI slices were first concatenated into a 3D MR-image using AFNI's *to3d* command and imported into FreeSurfer. The 3D MR volume was then registered with the Talairach atlas, skull-stripped using a deformable template, and intensity-normalized at each voxel in order to classify the voxels as white or grey matter. The cortical surface was inflated to define the sulci and gyri and head and skull models were subsequently created using MNE.

The left and right pial surfaces (merged together to form the full cortical surface), outer skull model and original MRI were then imported into BrainStorm and six fiducials (the nasion, left and right preauriculars, interhemispheric point, and the anterior and posterior commissure) were defined on the MRI image volume to align the imported surfaces into a common reference frame and co-register the cortical surface to the Talairach atlas.

The digitized locations of the EEG electrodes were used together with the cortical model to compute the forward model mapping cortical source activity onto the surface of the scalp

using a 3-shell spherical Berg model (Mosher, Leahy, Lewis 1999). The three concentric shells in the 3-shell Berg model are used to account for differences in the spreading of EEG signals through three primary mediums: the brain, skull, and scalp. The forward model was used to compute the scalp potentials for a set of neural current sources located on the cortex and oriented orthogonal to the surface. Brain, skull, and scalp boundaries (from the subject MRI) were applied using a boundary element method (BEM) to measure the forward fields or potentials at every point on the head. The inverse solution was then used to perform a least-squares (minimum-norm) localization of the current sources (for a particular potential field map on the scalp). This was done using a Tikhonov-regularized minimum-normalization estimation in Brainstorm based on the estimates of the forward model (Baillet et al., 2001). The inverse source projection matrix was subsequently applied to the averaged EEG epochs (L1 to L5) for Proprioceptive and Visual trials to generate current source density (CSD) maps across subjects.

It is important to note that although individual MR scans were collected for each subject, during the data analysis each subject's EEG data was projected on a single anatomical volume (Subject 1) to generate and image cortical source currents. This was done to facilitate group comparisons on a single cortical surface as there were both differences in the number of tessellated points and the corresponding coordinates for those vertices across subjects. Furthermore, no major differences were found in the current source density profiles generated using the subject's own anatomical when compared to those of the default anatomical. This observation is reasonable considering that all subjects were presented with the same experimental task and that EEG activity correlated with the magnitude of error was separated from baseline neural activity or noise (thus, we can assume the neural generators of the error response would remain consistent across subjects). Furthermore, the spatial localization of EEG

is not very accurate and would therefore not be as sensitive to minor variations in the cortical structure.

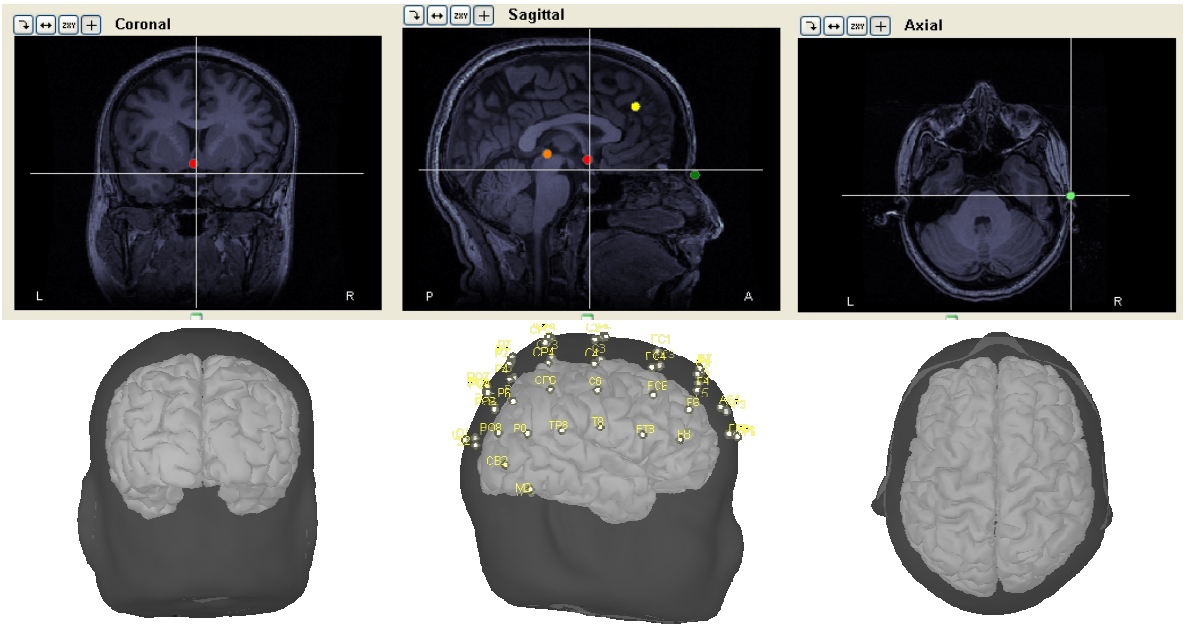

Figure 3.7: Transformation of MRI into 3D scalp and cortical models. The top row shows a single coronal, sagittal, and axial brain slice of a single subject's anatomy (Subject PU7493). The coronal slice contains a red dot marking the location of the anterior commissure (AC) and the saggital slice additionally shows the locations of the posterior commissure (orange), interhemispheric point (yellow), and nasion (green). The axial slice displays the right preauricular. The bottom row illustrates the corresponding coronal, sagittal, and axial views of the scalp and cortical models generated from the subject's MR volume (15003 vertices). The middle figure also shows the locations of the digitized electrodes on the subject's scalp.

3.6.4 Source Localization within ROI's

The distributed source model estimated the source currents at each point of the tessellated cortical mesh (i.e. vertices). To identify vertices with activity that was correlated significantly with displacement error (or 'error-correlated' vertices), we applied two additional analyses: a

‘source’ analysis and a ‘permutation’ analysis. In the source analysis we compared the cortical source activity across levels on a vertex-by-vertex basis, while the permutation analysis was used as a statistical method to correct for the effect of multiple comparisons in the dataset.

The multiple comparisons problem occurs when many statistical inferences are made from a set or family of data samples, wherein the likelihood of observing false positives, or the probability of incorrectly rejecting the null hypothesis, is increased. Highly conservative statistical measures that are more commonly used to address this issue, such as the BonFerroni method or Holm method, produce extremely stringent significance thresholds (or alpha values) that are inversely proportional to the sample size. Thus, these methods are more suitable for smaller datasets. In BrainStorm, the sample size (total number of tessellated points on the reconstructed cortical surface) was on the order of 15k which would result in extremely small alpha values. Additionally, as the current sources were estimated using a minimum-norm inverse solution of the scalp activity across 64 electrodes the variability at each point on the cortical surface was not statistically independent, violating the parametric assumptions underlying a statistical t-test (and the corresponding use of the BonFerroni correction). The use of permutation statistics is advantageous in this regard since it does not make *a priori* assumptions regarding the statistics of the dataset, instead using the statistics of the specific dataset to determine the nonparametric threshold for significance. For the analysis in this study, permutation statistics was used to measure the distribution of vertices that would pass as significantly correlated with error based upon random chance.

A. Source Analysis

For each condition, the CSD profiles for all levels were loaded into MATLAB®. Under the assumption that the baseline distribution across epochs (i.e. -100 to 0 ms) was task-irrelevant, or for our purposes "noise," a threshold was set to separate 'noise' vertices from 'signal' vertices. The threshold was set at the 95% significance level (two-tailed) of the averaged baseline distribution for Level 5 (see Figure 3.8 B). A 50-ms window with a 10-ms sliding scale was then used to compute the averaged CSD for each vertex over time. Within each time window, vertices with averaged CSD values below the threshold were removed from further analysis. A 50-ms window was chosen here to balance out the extensive computation time associated with shorter window lengths while minimizing the loss of SNR associated with larger window lengths.

For those vertices above threshold, the CSD profiles in each time window were summed to measure the area of the CSD across levels – the values of the area for levels 1 to 5 of each significant vertex were then correlated with the peak positional error across levels at each time window to identify vertices whose activity was highly correlated with error. The slopes, p-values, and r-values of the correlations across vertices were than saved and processed offline. Permutation analysis was then performed to measure the probability of particular correlations occurring within a randomized dataset in order to determine vertices whose correlations were significantly above chance.

B. Permutation Analysis

The event flag labels on the epoched EEG data (i.e. Levels 1 – 5) were rearranged randomly across the dataset, keeping the total number of trials/level and trial-to-trial intervals the same as the real dataset (refer to Figure 3.8 A). The epochs were then re-averaged across levels and imported into BrainStorm to generate new CSD profiles which were subsequently imported into MATLAB® for analysis. Similar to the source analysis, time window averages of permutation CSD profiles were summed to measure the area in each time window which was then correlated with the peak positional response to generate a new set of correlation slopes, p-values, and r-values. The distribution of the fitted slopes (refer to Figure 3.8 B) indicated the likelihood of obtaining a particular proportional relationship between the CSD and position error from a random set of data. Using the 95% confidence bounds of the slope distribution, we were able to parse out vertices with high correlation and large slopes from those with high correlations but slopes close to zero, indicating little if any relationship between the CSD and position error. Thus, the 95% slope threshold on the permutation distribution (two-tailed) was used in the original data analysis to identify "significant" vertices exhibiting high linear correlations (p-values above 0.05) and fitted slopes above 95% bounds of the permutation slope distribution (see Figures 3.8 B and C).

Determining ROI's of Significant Vertices

To identify the cortical regions involved in error processing, significant vertices were separated into regions of interest (ROI's) based on their Talairach positions on the cortical surface. These ROI's were chosen based on the initial cortical locations of significant vertices across subjects and were drawn from the corpus of areas in the literature associated with on-line

error-processing during reach: BA 8 (frontal), BA 2, 3 (somatosensory), BA 17, 18 (visual), BA 4 (motor), BA 6 (premotor), BA 5, 7, and 40 (parietal).

Temporal and Spatial Analyses of ROI's

The temporal sequence of activation across ROI's was determined with respect to the leading edge of the sliding window based on the first occurrence of significant activity within the ROI. The mean and standard error across subjects was measured for each ROI to illustrate the average temporal relationship between the neural sources.

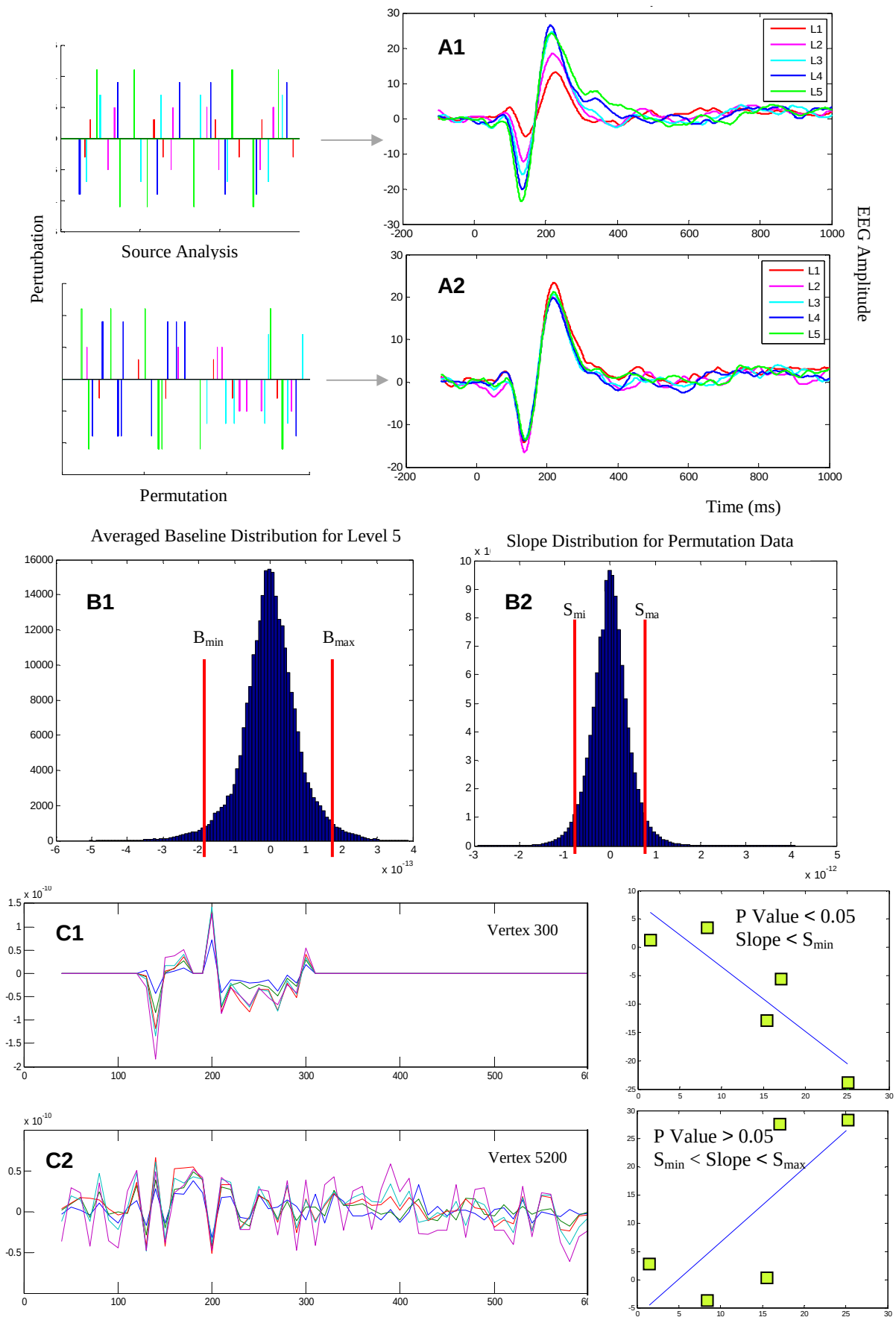
A1
A2
L1
L2
L3
L4
L5
Perturbation
Source Analysis
Permutation
EEG Amplitude
Time (ms)
Averaged Baseline Distribution for Level 5
B1
B_{min}
B_{max}
Slope Distribution for Permutation Data
B2
S_{mi}
S_{ma}
C1
Vertex 300
C2
Vertex 5200
P Value < 0.05
Slope < S_{min}
P Value > 0.05
S_{min} < Slope < S_{max}

Figure 3.8: Overview of cortical source analysis. The figure above illustrates the experimental analysis applied to separate cortical vertices whose activity correlated with error from vertices unrelated to the task. (A) shows differences in a sampled EEG epochs derived from the experimental study (A1) when compared to the same EEG sequence after subjected to permutation (A2). An increase in the peak magnitude with level can be seen in (A1) but not (A2). The histograms in (B) show two distributions that were used to eliminate vertices uncorrelated with the task error. (B1) shows average baseline cortical activity (i.e. -100 ms to 0 ms) in Level 5 for a single subject. An upper and lower threshold (2.5% and 97.5%) was set to determine vertices that had source activity above or below the noise threshold (i.e. they fell outside the baseline or noise distribution). (B2) illustrates the permutation slope distribution with an upper and lower threshold used to determine vertices whose fitted slopes were significantly above chance. The figures in (C) show sample vertices that were either correlated (C1) or uncorrelated (C2) with error based on the p-value and slope magnitude of the correlation. (C1) shows negatively-correlated CSD activity across levels with significant linear correlation (p-value < 0.05) and with a large slope outside the permutation slope threshold. Conversely, the vertex in (C2) has a poor correlation (p-value > 0.05) and a slope that falls within the permutation slope threshold. Thus, in this case, vertex 300 would be considered correlated with error, whereas vertex 5200 would be eliminated from further analysis.

Spatial differences between proprioceptive and visual sources were determined by measuring the relative differences between the centroid locations of the vertices that were significantly correlated with the task. Centroids locations (x, y, z) in Talairach space, were weighted by the strength of the magnitude of each vertex (i.e. the current source density value for Level 5 at that vertex) using the following equations (at each time window):

$$X_{centroid} = \frac{1}{\Sigma W_n} \sum_{N}^{n=1} (X_n W_n) \; ; \; Y_{centroid} = \frac{1}{\Sigma W_n} \sum_{N}^{n=1} (Y_n W_n) \; ; \; Z_{centroid} = \frac{1}{\Sigma W_n} \sum_{N}^{n=1} (Z_n W_n)$$

$$\text{Centroid} = [X_{centroid} \; Y_{centroid} \; Z_{centroid}]$$

where for the ith observation (time window), *n* is the index of each significant vertex, *N* is the total number of significant vertices, and *W* is the magnitude of the current source density (CSD) for Level 5 of the nth vertex.

For the purpose of displaying the centroid on the cortical surface, the closest tessellated point to the x, y, z location of the centroid was identified by measuring the vertex with the

closest Euclidean distance to the actual centroid (Figure 4.9). In order to compare spatial distributions of the centroids within each ROI for the Proprioceptive and Visual conditions, the centroid locations from the three non-overlapping time windows centered around the N100 response (measured independently for each subject for Proprioceptive and Visual conditions) were examined. For example, for a representative subject, MD9904, the N100 occurred at 135 ms and 201 ms for Proprioceptive and Visual conditions respectively. For the Proprioceptive condition, the three time windows chosen for this subject were 60-110 ms (1st), 110-160 ms (2nd – centered around the N100 at 135 ms), and 160-210 ms (3rd). For the Visual condition, the time windows were, 130-180 ms (1st), 180-230 ms (2nd – centered around N100 at 201 ms), and 230-280 ms (3rd).

Centroids were computed for each ROI in each time window to examine the spatial distribution of cortical activity for visual and proprioceptive error processing. To measure differences in the spatial distributions on the cortex, the Mahalanobis distance between Visual and Proprioceptive conditions was measured across subjects for each ROI. The Mahalanobis distance, unlike Euclidian distance, measures the distance between the mean vectors of two groups relative to the covariance of the two distributions. To understand differences in spatial distributions, histograms of Mahalanobis distance measures were compared qualitatively across ROI's.

4 EXPERIMENTAL RESULTS

4.1 Behavioral response to proprioceptive and visual displacements

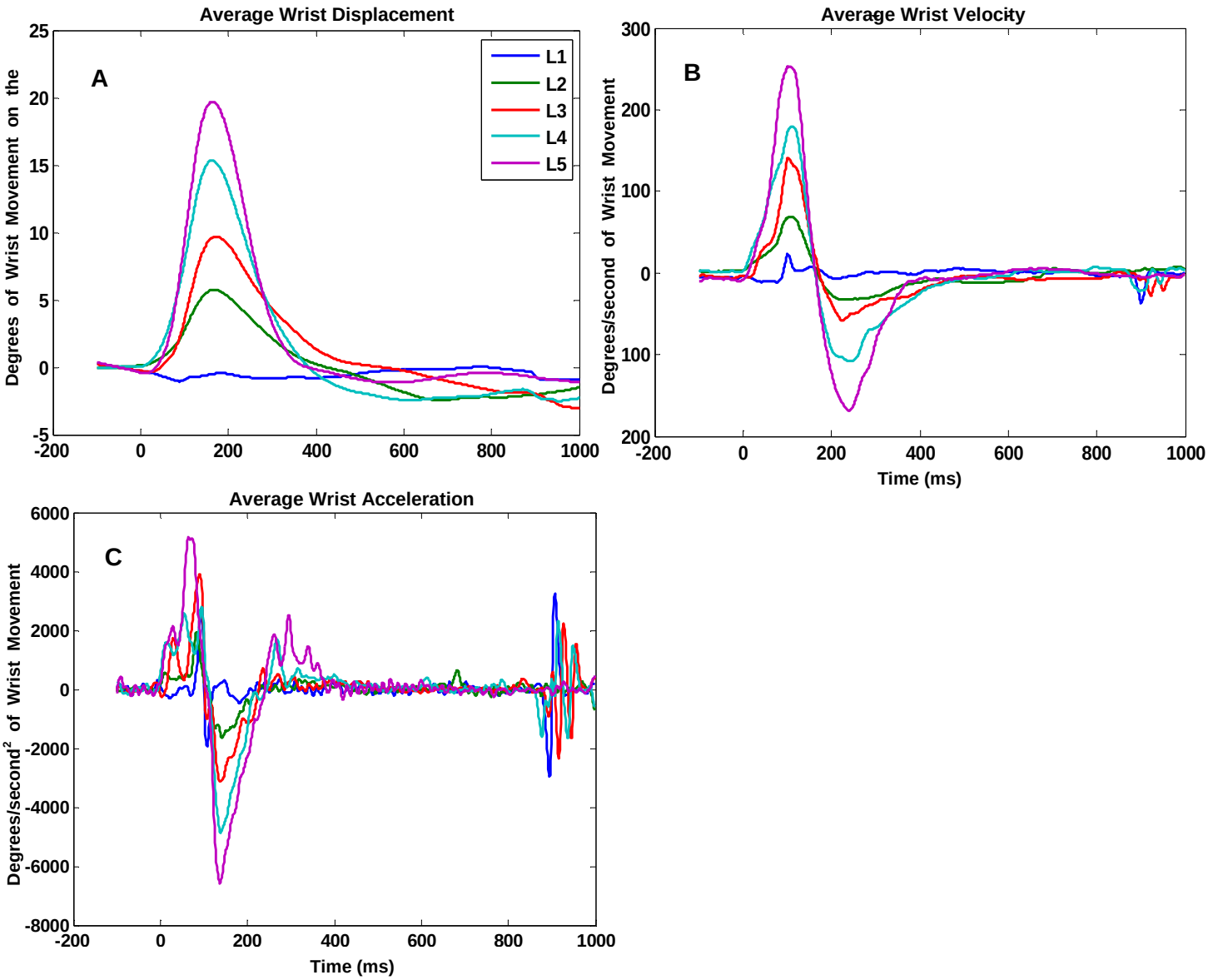

Figure 4.1: Behavioral responses to force perturbation of the wrist during tracking. Averaged behavioral responses of (A) wrist displacement (in visual coordinates), (B) velocity, and (C) acceleration in response to a force perturbation are shown above for a representative subject (MD9904). Responses were averaged across trials for the five levels of force perturbation (L1-L5). Wrist displacement was calculated as the difference between the target and virtual cursor position relative to perturbation onset and low-pass filtered at 30 Hz (4th order, zero-phase, Butterworth) to remove electromechanical noise (A). Wrist velocity (B) and acceleration (C) were obtained by calculating the first and second derivatives of the wrist displacement response.

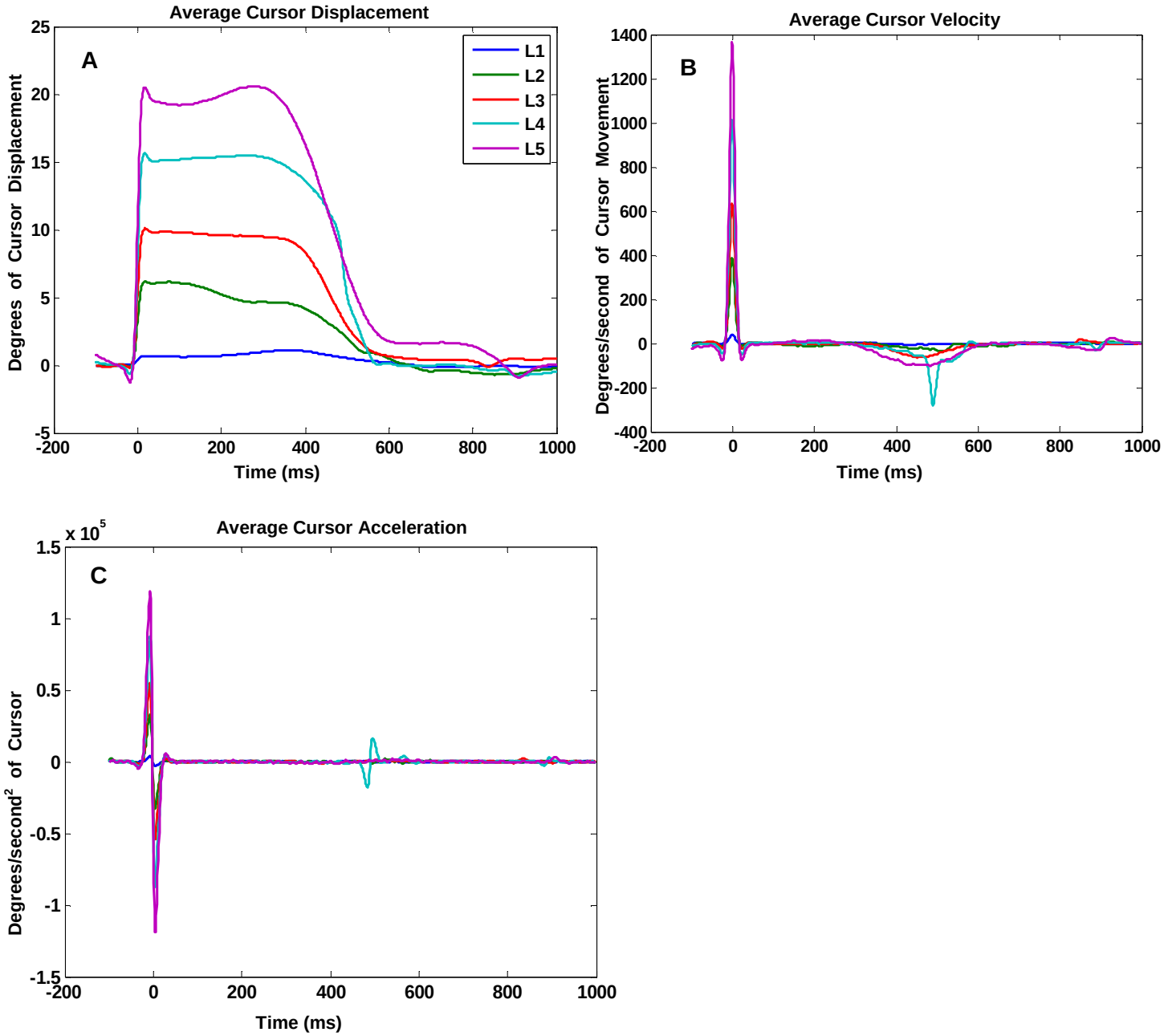

Figure 4.2: Behavioral responses to visual displacement of the cursor during tracking. Averaged behavioral responses of (A) cursor displacement, (B) velocity, and (C) acceleration (in visual coordinates) in response to visual perturbations are shown above for a representative subject (MD9904). For each level, the applied cursor displacement was matched in amplitude to the average peak displacement generated in corresponding Proprioceptive trials. Responses were averaged across trials for the five levels of visual perturbation (L1-L5). Cursor displacement was calculated as the difference between the target and cursor position relative to perturbation onset and low-pass filtered at 30 Hz (4th order, zero-phase, Butterworth) to remove quantization noise induced by the lower frequency display (A). Cursor velocity (B) and acceleration (C) were obtained by calculating the first and second derivatives of the cursor displacement response.

Figure 4.1 shows the average wrist position, velocity, and acceleration in response to force perturbations (Proprioceptive trials) for a single representative subject. Subject MD9904 is presented here as a representative subject to illustrate the single subject neural and behavioral responses for all results presented henceforth in this thesis. Results for the other subjects can be found in Appendices A-C. In Proprioceptive trials, wrist displacement was measured as the positional difference (in degrees of visual angle) between the target and virtual cursor on the screen rather than between the target and the wrist (in degrees of wrist angle). This was done for two reasons: i) in Proprioceptive trials the wrist position corresponded directly to the position of the virtual cursor on the screen (see Methods section 3.5.1). This relationship was not maintained in visual trials as each visual displacement generated a mismatch between the subject's actual wrist position and the visual cursor on the screen. The mismatch was generated by the fact that visual displacements were presented as *continuous* visual offsets applied only to the cursor position and not to the wrist; this was not the case for proprioceptive trials where applied torques were 'turned off' after 100 ms. Therefore, if we converted visual cursor position from visual angle to wrist angle in visual trials, we would not necessarily obtain the actual wrist position on the robot (due to the mismatch); ii) Thus, in order to compare differences in proprioceptive and visual displacements, the comparison was performed in visual coordinates and not wrist coordinates. *To avoid confusion, virtual cursor displacements of the wrist for proprioceptive trials are henceforth referred to as wrist displacements (in visual coordinates) rather than cursor displacements since the perturbations were in fact applied to the subject's wrist and not the cursor per se.*

Proprioceptive wrist displacements were measured from 100 ms prior to perturbation onset to 1000 ms post onset and averaged across trials to obtain average wrist displacements for

each level. Averaged wrist displacements were then low-pass filtered at 30 Hz using a zero-phase Butterworth filter to remove high-frequency noise contributed by the robot (Figure 4.1 A). Wrist velocity and acceleration responses were obtained by computing the first and second derivatives of the position response in (Figure 4.1 B, C).

Externally applied force perturbations (L1 – L5) were used to induce five levels of wrist displacement whose peak value was in turn used to define the five levels of cursor displacement applied in the Visual condition (see Methods section 3.3.3). Consequently, displacement errors (target position minus cursor position) in Visual trials were comparable in magnitude to virtual cursor displacements applied in the proprioceptive trials with a mean difference of 0.63 ± 0.6 degrees across levels (Figures 4.1 A and 4.2 A).

As can be seen in Figure 4.1 A, each force perturbation caused the wrist to deviate from the target until it reached maximum displacement (at 167.8 ± 4.1 ms across levels). Subjects then corrected for the error in position by bringing the wrist back onto the target (baseline). Similar errors in cursor position are seen across levels in the visual trials (Figure 4.2 A) wherein displacements in cursor position (relative to the target) required subjects to make a correction to bring the cursor back onto the target. Unlike Proprioceptive trials, visual errors reached their maximal displacement instantaneously (at 0 ms: perturbation onset) and remained maximal up to 379.6 ± 43.96 ms following onset after which they returned to baseline. In proprioceptive and visual trials, error in cursor position returned to baseline by 467.6 ± 104.4 ms and 657.4 ± 39.2 ms respectively. These values were measured by calculating mean and standard deviations of proprioceptive and visual baselines across behavioral L1-L5 responses (-100 ms to 0 ms; Figures 4.1 A and 4.2 A) and then measuring the time required in the Proprioceptive and Visual trials for the displacement error to return within two standard deviations of mean baseline. The time taken

to return to baseline was approximately 189.8 ± 22.3 ms longer in the visual condition than the proprioceptive condition which can be accounted for by the longer feedback delay associated with visual (200-250 ms) versus proprioceptive (80-150 ms) processing (Flanders and Cordo 1989).

The average wrist velocity profiles for Proprioceptive and Visual trials show a more detailed aspect of the subject's response. Following the application of a force perturbation, wrist velocity spiked before the wrist eventually slowed down to a stop due to the passive dynamical properties of the hand; the first turnaround point of bringing the wrist to a stop occurred at 107.2 ± 5.1 ms (maximum peak). Wrist velocity increased again at roughly 168 ms as subjects moved their wrists back toward the target (to minimize the displacement between target and cursor position) after which wrist velocity again returned to baseline. The second turnaround to slow wrist velocity occurred at 335.2 ± 9.1 ms (minimum peak). This is different from visual trials, which only show one peak (at 0 ms) in the cursor velocity profile (see Figure 4.2 B). This is because visual perturbations were induced instantaneously as deviations in cursor position (thus, there was high velocity associated with the jump in cursor position at 0 ms) followed by a corrective action performed by the subject to bring the cursor back onto the target.

4.2 Evoked neural response to proprioceptive and visual displacements

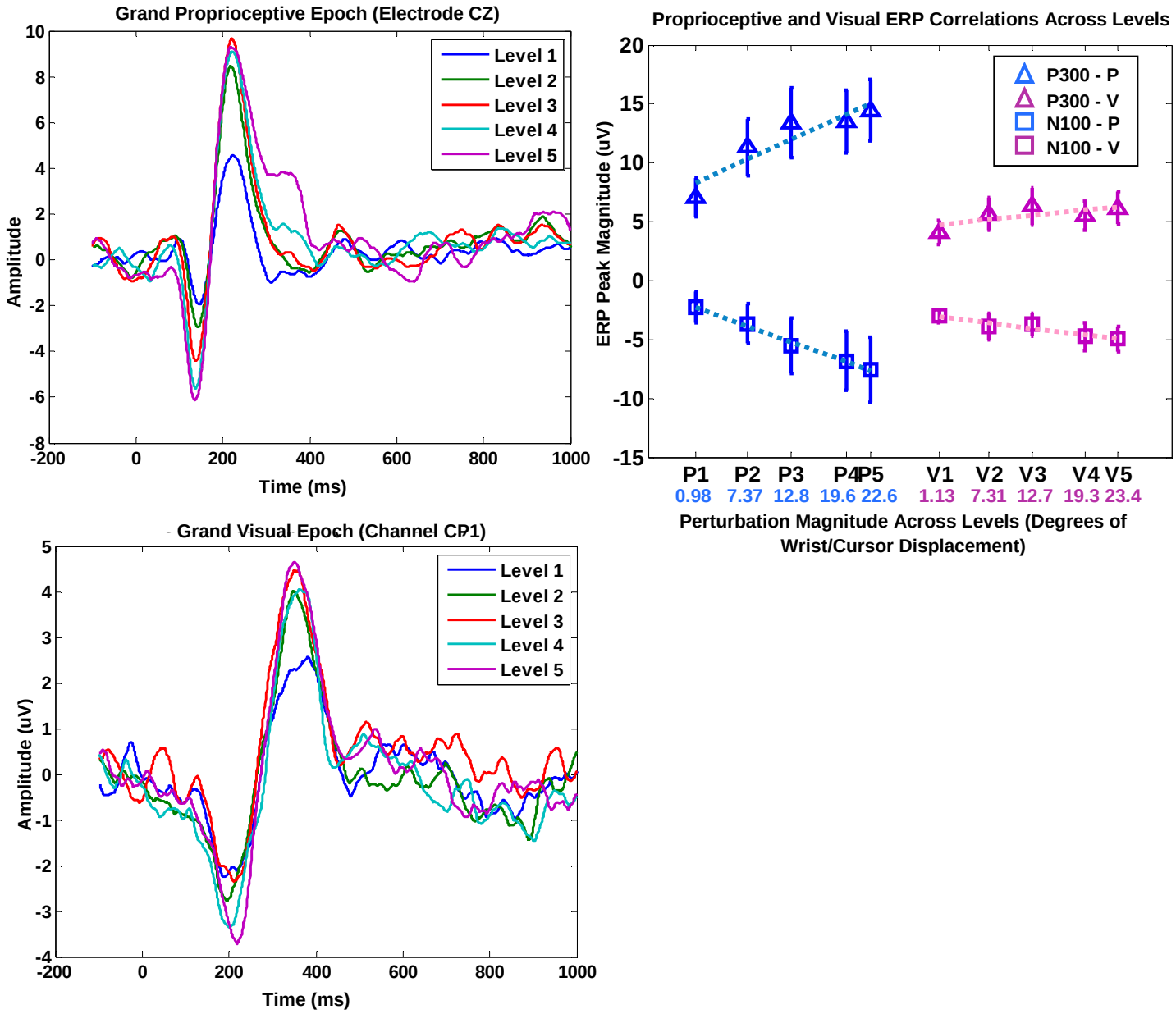

Figure 4.3. Grand average evoked potentials measured across subjects (N=7) in response to force displacements of the wrist and visual displacements of the cursor. Evoked responses are shown at electrode CZ for (A) Proprioceptive trials and electrode CP1 for (B) Visual trials. EEG epochs were measured relative to perturbation onset at 0 ms. For each condition, trials were averaged across perturbation levels. The minimum and maximum peaks seen in the evoked responses reflect the N100 and P300 components of the event-related response (ERP) in each condition. Correlations of the ERP peaks with displacement magnitude (i.e. maximum wrist/cursor displacements seen in Figures 4.1 A and 4.2 A) were quantified across perturbation levels (C). N100 peaks were highly correlated across levels for both types of displacement (P: r=-0.996, p<0.001*; V: r=-0.957, p=0.01*) and P300 peaks for Proprioceptive but not Visual (P: r=0.923, p<0.05*; V: r=0.719, p>0.05). Error bars indicate standard error across subjects. In (C), blue colored blocks indicate proprioceptive ERP's, and red reflect visual ERP's of the N100 (squares) and P300 (triangles) peaks respectively.

Figure 4.3 illustrates the grand average evoked response to force (Proprioceptive trials) and Visual (visual trials) perturbations across subjects. Two different electrodes are shown to illustrate the evoked responses for the two conditions: electrode CZ for the Proprioceptive condition which is more centrally based, and electrode CP1 for the Visual condition which is maximal over the left occipitoparietal area. These electrodes were chosen specifically as they were able to extract a clean temporal response of the EEG for visual and proprioceptive trials across subjects.

The evoked responses to force and visual perturbations appear similar in form: both have a negative peak from 100 to 200 ms from perturbation onset followed immediately by a positive peak located between 200 to 400 ms across levels. The two peaks resemble the N100 and the P300, two sensory evoked potentials largely implicated in sensorimotor processing. The N100 is a negatively-peaked ERP that is said to occur from 100 to 200 ms following stimulus onset and is associated with early stimulus discrimination in tasks that involve target tracking while the timing of the positively-peaked P300 ranges from 250 to 500 ms following stimulus onset and is associated with the detection of a change in the sensory stimulus based on working memory of previous stimuli (Polich 2007). In this study, the N100 occurred at 146.9 ± 4.5 ms in proprioceptive trials and at 200.7 ± 6.5 ms in visual trials whereas the P300 occurred at 243.1 ± 15.9 ms and at 351 ± 6.6 ms in proprioceptive and visual trials respectively. The mean values were measured by calculating the average N100 and P300 peak timings across levels and subjects (standard error is shown across subjects). Although the evoked responses in Figures 4.3 A and B appear similar in form, they are shifted in time (the visual N100 response is shifted ~ 60 ms later), which could be associated with the longer feedback delay in processing visual information.

The magnitudes of the N100 and the P300 were correlated across perturbation levels in the Proprioceptive and Visual conditions. Figure 4.3 C illustrates the linear relationship between applied perturbations (L1 to L5 in proprioceptive and visual trials) and the corresponding peak evoked responses. Proprioceptive and visual ERP's were highly correlated with the magnitude of position displacement applied across levels for the N100 (P: r=-0.996, p=0.0004*; V: r=-0.957, p=0.01*) and less so at the P300 (P: r=0.923, p=0.03*; V: r=0.719, p=0.17). This is consistent with a study of visually-guided tracking that found scaling of EEG activity (with externally applied error), when visual rotations were introduced in the task (Anguera, Seidler, Gehring 2009). The proprioceptive N100 response also shows a time to peak across levels was inversely proportional to the magnitude of perturbation applied.

Closer inspection of the P300 in proprioceptive and visual trials shows two peaks for proprioceptive trials whereas only one peak is seen in visual trials. The two peaks for the proprioceptive P300 evoked response represent two subcomponents of the ERP: the larger P3a response typically associated with the allocation of attentional resources to salient stimuli in a task (Hill and Raab 2005b), and the P3b response thought to represent the visual detection and processing of target and deviant stimuli (Menon et al., 1997). In proprioceptive trials, the P3a occurred at 227.8 ± 8.2 ms and the P3b at 326.8 ± 10.9 ms.

4.3 Cortical source reconstruction across proprioceptive and visual ROI's

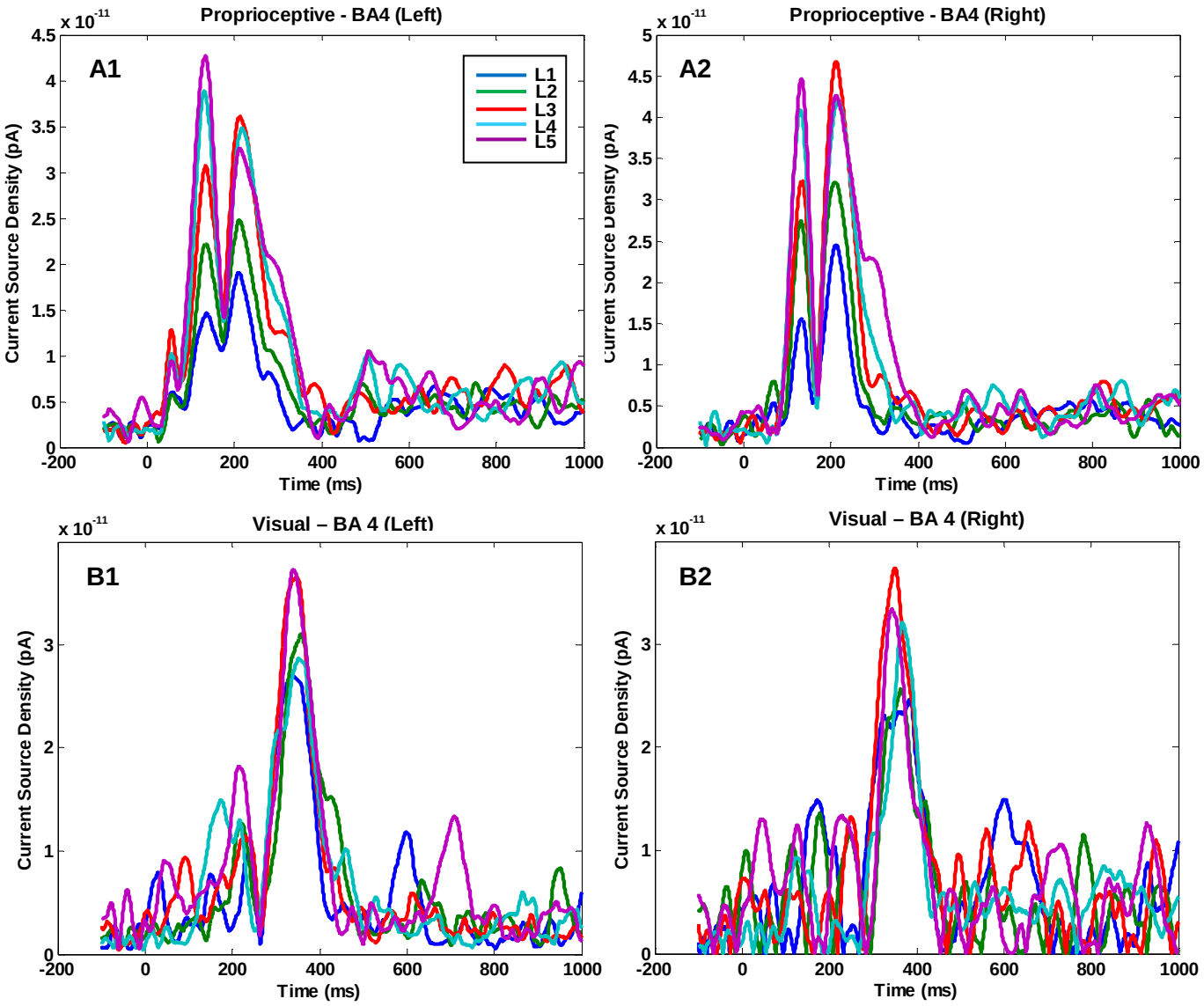

Figure 4.4: Current source density (CSD) profiles for left and right Brodmann Area 4 in subject MD9904. CSD profiles across levels are shown separately for BA 4 in the left and right hemispheres for the proprioceptive condition (A1 & A2 respectively) and the visual condition (B1 & B2 respectively). The plots reflect the current density response of all significantly-activated vertices within a 50-ms sliding time window with 40 ms overlap. Plots A1 and A2 show the entire time course of cortical activity of significant vertices in the 110-160 ms (centering around the timing of the N100 for Proprioceptive) whereas plots B1 and B2 display activity in the 180 – 230 ms (centering around the timing of the N100 for Visual) time window.

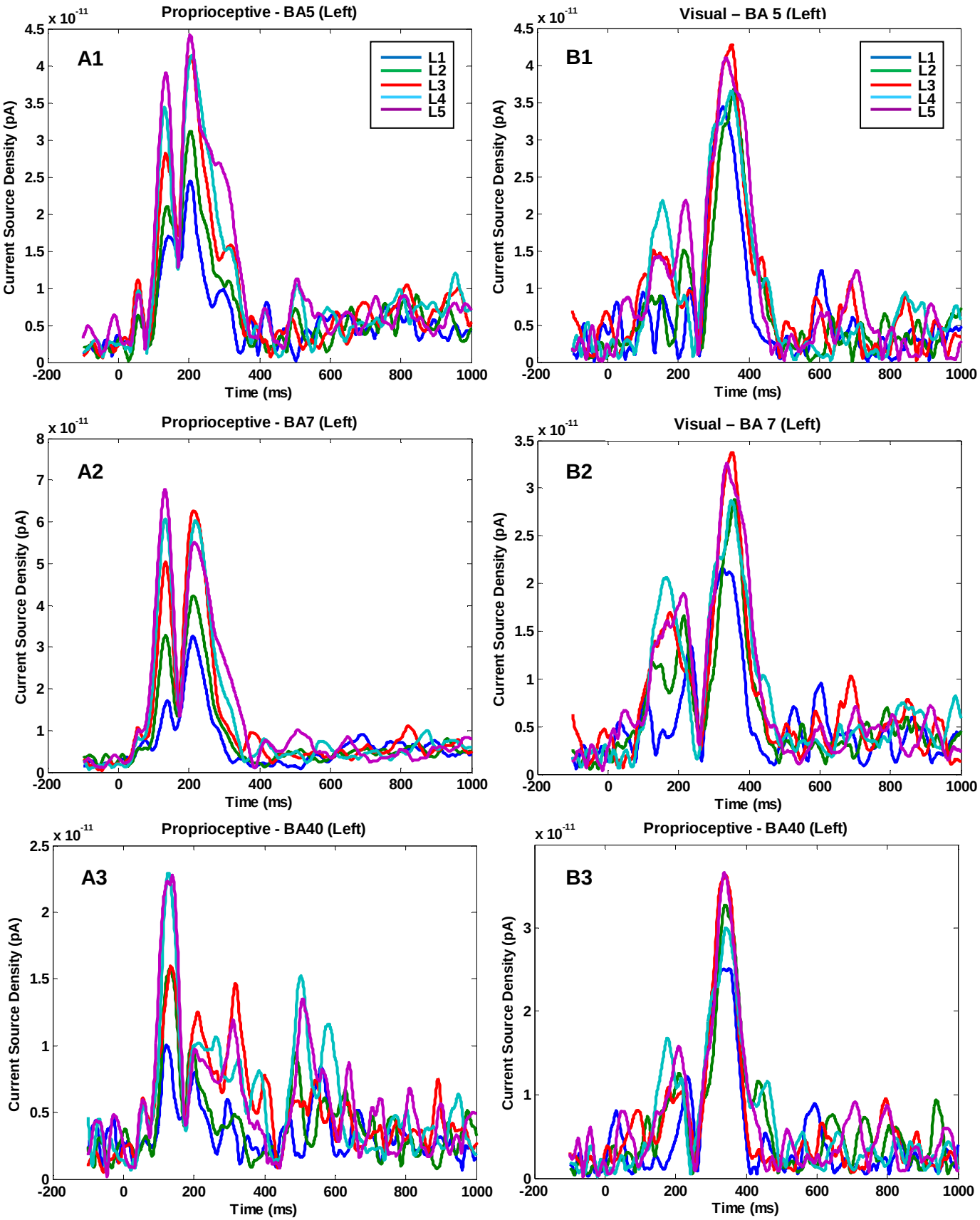
Proprioceptive - BA5 (Left)
A1
Visual – BA 5 (Left)
B1
Proprioceptive - BA7 (Left)
A2
Visual – BA 7 (Left)
B2
Proprioceptive - BA40 (Left)
A3
Proprioceptive - BA40 (Left)
B3
L1
L2
L3
L4
L5
x 10^-11
Current Source Density (pA)
Time (ms)

Figure 4.5: Current source density (CSD) profiles for left parietal areas (BA's 5, 7, and 40) in subject MD9904. CSD profiles across levels are shown separately for left parietal BA's 5, 7, and 40 in the BA 4 in the proprioceptive (A1 – A3) and visual (B1 – B3) conditions. The plots reflect the current density response of all vertices within a 50-ms sliding time window (40 ms overlap) whose activity was correlated significantly with error. Plots A1 – A3 show the entire time course of cortical activity of significant vertices in the 110-160 ms (centering around the timing of the N100 for Proprioceptive) whereas plots B1- B3 display activity in the 180 – 230 ms (centering around the timing of the N100 for Visual) time window.

The EEG data measured across subjects (Figures 4.3 A and B) was analyzed in Brainstorm together with the MRI anatomical data to estimate the spatiotemporal sequence of activity constrained to the cortical surface (see Section 3.6.3) to determine brain regions that were significantly correlated with task error. The cortical source density (CSD) profile for each tessellated point (vertex) on the cortical mesh was measured using the distributed source reconstruction approach detailed in Section 3.6.3. ROI's containing error-correlated vertices were mapped with their Talairach coordinates and include: BA's 8 (frontal), 2&3 (somatosensory), 17&18 (visual), 4 (motor), 6 (premotor), 5, 7, and 40 (parietal). Figures 4.4 and 4.5 show a subset of current source density activity in motor (BA 4) and parietal areas (BA's 5, 7, and 40) for a representative subject. Similar figures illustrating CSD profiles across all Brodmann areas and time windows are displayed in Appendix C for all subjects. However, it must be noted that cortical reconstruction results for Subject CL2426 did not yield significant correlations to error across parietal and visual ROI's in the Visual condition (refer to Appendix C) – therefore, subject averages for mean error onset times displayed in Figure 4.6 were measured across subjects that contained significant vertices across all time windows in that ROI.

Cortical activity in BA's 4 and 5, 7, and 40 are shown here for two reasons: i) temporal results showed early activity in motor cortex (BA 4) before parietal activation in proprioceptive trials (Figure 4.6). Thus, we were interested in understanding the significance of this early

activity in BA 4; ii) our experimental hypotheses predicted a major role of the parietal areas in computing and processing sensorimotor error. The parietal CSD profiles would therefore indicate any differences in cortical source currents in the two conditions during peak error in the behavioral response. The CSD profiles shown here (and Figure 4.5) display the entire time course of current density (of significantly activated vertices averaged in a selected time window). Due to differences in proprioceptive and visual sensory processing times, time windows were centered around the N100 response for both conditions (see Figures 4.3 A and B). This allowed us to directly compare cortical activity during the period wherein peak cortical activity was significantly correlated with the magnitude of error applied across both proprioceptive and visual trials. As a result, for representative subject MD9904 shown in Figures 4.4 and 4.5, we examined proprioceptive activity in the 110-160 ms time window (to capture proprioceptive N100 at 135 ms) and visual activity in the 180-230 ms time window (to capture visual N100 at 201 ms).

Qualitatively, visual CSD profiles across ROI's contain much noisier baselines (Figures 4.4 and 4.5 B) which may be reflective of the poorer correlations in neural activity for visual versus proprioceptive trials (see Figure 4.3 C). Left cortical motor activity in proprioceptive trials shows three peaks (which is similarly seen in right BA 4): the first (a) situated at 58.6 ± 1.34 ms, the second (b) at 137.8 ± 2.28 ms, and the third (c) at 213.8 ± 2.86 ms (Figure 4.4 A1). Three similar peaks are seen in the Visual condition: the first (a) appearing at 211.8 ± 19.6 ms, the second (b) at 341.4 ± 9 ms, and the third (c) at 606.8 ± 1.62 ms. When correlated with the magnitude of position displacement applied (L1 – L5), proprioceptive peak (b) was significantly correlated to error ($r=0.99$, $p<0.001$*) while peaks (a) and (c) were not (a: $r=0.72$, $p=0.16$; c: $r=0.82$, $p=0.08$). In visual trials, similarly, peak (b) was highly correlated with displacement ($r=0.95$, $p<0.05$*) while peaks (a) and (c) were not (a: $r=0.85$, $p=0.06$; c: $r=0.53$, $p=0.36$).

Figures 4.5 A and B show the estimated parietal CSD in the Proprioceptive and Visual condition for the same subject. CSD activity in BA 5 was correlated significantly with perturbation at two peaks: (a) at 139.4 ± 5.2 ms, r=0.93, p<0.05*, and (b) at 210.2 ± 1.79 ms, r=0.92, p<0.05* in proprioceptive trials; and at a single peak: (a) at 343.4 ± 8.74 ms, r=0.87, p=0.05* in visual trials. Left BA 7 (Figure 4.5 A2) contained three highly-correlated overlapping peaks: (a) at 139.4 ± 3.6 ms (r=0.99, p<0.001*); (b) at 208.4 ± 2.9 ms (r=0.94, p<0.05*); and (c) at 313.8 ± 15.5 ms (r=0.91, p<0.05*) in proprioceptive trials. This sustained period of correlated cortical activity from 139 ms to 314 ms is also observed later in Figure 4.7 A showing the functional activation of the ROI across time. Also, peak (a) of BA 7 coincided in timing with peak (b) of proprioceptive BA 4, just before maximal displacement is seen in the behavioral wrist position across trials. In visual trials, peaks (a) and (b) in left BA 7 were correlated with error (a: 200.8 ± 23.1 ms, r=0.41, p=0.49; b: 357.4 ± 16.6 ms, r=0.94, p<0.05*). On the other hand, BA 40 was extremely noisy in both proprioceptive and visual trials for this subject, with only one discernable peak in proprioceptive trials (136.6 ± 7 ms, r=0.98, p<0.05*), and two peaks in visual trials: (a) at 194 ± 19.8 ms, r=0.8, p=0.1; and (b) at 343.8 ± 14.6 ms, r=0.89, p<0.05*. Across all three parietal areas, proprioceptive peaks that are highly correlated with error seem to occur simultaneously at 138.5 ± 1.62 ms with motor activation at 137.8 ± 2.28 ms which may suggest that both parietal and motor areas work together to compute a detailed estimate of error.

4.4 Temporal activation of sources correlated with proprioceptive and visual error

Figure 4.6 shows the temporal onset times of task-related activity within ROIs averaged across subjects for the Proprioceptive (blue) and Visual (red) conditions (see also Table 4.1). "Error-related activity" was identified as source activity (i.e. current source density) that was significantly correlated with the magnitude of position displacement (L1 – L5) as determined from the permutation analysis.

Brain areas correlated with error were determined qualitatively by observing the spread of significantly activated vertices on the cortex in the first few time windows displaying average cortical activity in a 50-ms time window. Regions containing error-related vertices in these time windows defined based on their Talairach coordinates to determine their functional Brodmann Areas (BA's). The ROI's investigated in this study were BA's 2&3 (somatosensory), 17&18 (visual), 8 (frontal), 4 (motor), 6 (premotor), and 5, 7 and 40 (parietal). BA's 2&3 were only correlated to error in the proprioceptive condition (since the displacement was applied to the wrist), whereas visual areas (BA 17&18) were only correlated with the task when the displacement was applied visually. Overall, source activity correlated to the task occurred bilaterally in frontal (BA 8), motor (BA 4), and premotor (BA 6) cortices but was restricted to the left hemisphere in the case of parietal areas (BA's 5, 7, and 40).

Error onset times across ROI's were computed as the first measurable significant activity (i.e. the presence of at least one significantly correlated source) within a single time-window. All ROI's in the proprioceptive condition were activated significantly earlier than those in the visual condition. With force-induced errors, early sensory activation in left somatosensory cortex (42.7±4.8 ms) was followed by premotor (45.6±6 ms), motor (47±6.9 ms), and frontal activation (48.4±6 ms), and finally by activation in parietal cortices (69.9±7.8 ms in BA 40). A similar

pattern of activity was seen in the right cortex where premotor activation was followed by frontal and motor activity. Temporal relationships in the Visual condition were much less consistent across left and right cortices – in left cortex, parietal activation in areas BA7 (113.3±8 ms) and BA40 (121.7±17.8 ms) were followed by sensory (123.3±41.4 ms), motor (125.7±14.3 ms), and premotor activity (131.4±22.3 ms) and much later by frontal activation (212.9±48.6 ms). Right cortical activity, conversely, showed early visual (88.57±14.87 ms), premotor (100±19.5 ms), frontal (125.7±36.4 ms), and motor activation (187.1±42.9 ms) followed later by frontal activation (211.7±39.3 ms). Refer to Table 4.1 and Figure 4.6.

Although Figure 4.6 provides an illustration of the relative onset timings of error-related activity across ROI's, it does not discriminate against the total number of vertices that achieved significance within a particular time window (i.e. a single significant vertex within an ROI can signal the error onset time). Figures 4.7 and 4.8 show the peak functional activation of all error-correlated vertices within ROI's over time both across subjects and for a single subject (MD9904). Here, a normalized measure of functional activation is used, wherein the integrated CSD across error-correlated vertices for each time window is divided by the total number of error-correlated vertices across all time windows for each ROI. In Figures 4.7 and 4.8 A and B (i.e. single subject data), the color bar indicates a minimum level of functional activation at 0 and a maximum at 1 – a peak of 1 can be seen in all ROI's indicating the time of maximum activity within the ROI.

Table 4.1: Task-related source onset times (mean ± SE) for proprioceptive and visual ROI's across subjects. Cortical sources that were significantly correlated with magnitude of the displacement error were separated into ROI's to characterize the spatiotemporal dynamics of error-related activity. The first instance significant error-related activity within each ROI is reported as the mean ± SE across subjects.

	Brodmann Areas (BA's)	**Mean (ms)**		**Standard Error (ms)**	
		Proprioceptive	**Visual**	**Proprioceptive**	**Visual**
Left Cortex	Frontal (8)	48.43	212.86	5.95	48.63
	Somatosensory (2&3)	42.71		4.81	
	Visual (17&18)		123.33		41.36
	Motor (4)	47	125.71	6.90	14.29
	Premotor (6)	45.57	131.43	5.95	22.30
	Parietal (5)	74.14	173.33	7.47	35.84
	Parietal (7)	72.71	113.33	6.85	8.03
	Parietal (40)	69.86	121.67	7.78	17.78
Right Cortex	Frontal (8)	61.29	125.71	12.88	36.44
	Visual (17&18)		88.57		14.86
	Motor (4)	72.71	187.14	9.22	42.86
	Premotor (6)	47	100	8.45	19.52

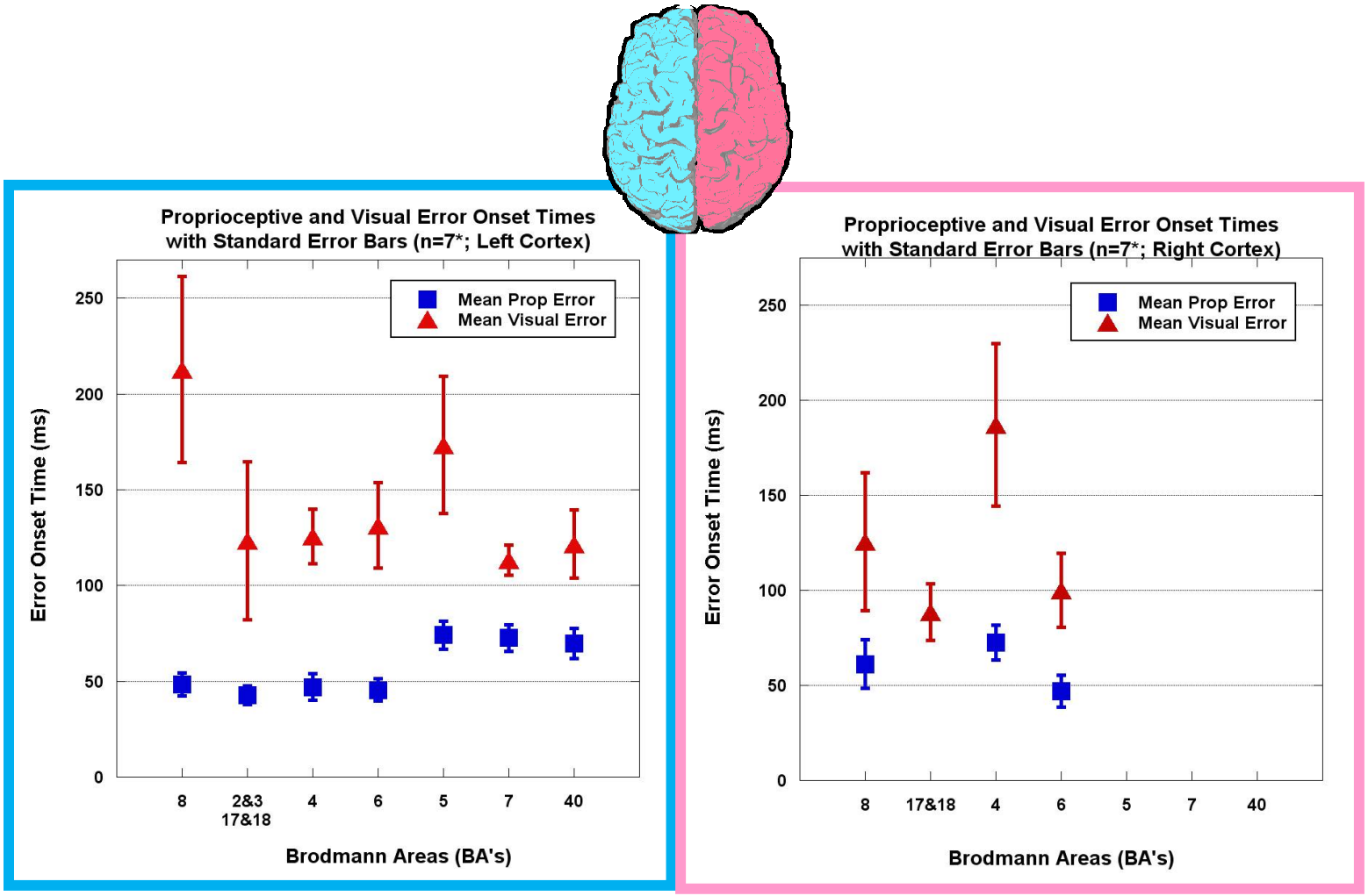

Figure 4.6: Temporal dynamics of error processing across ROI's for left and right cortices. Source responses were correlated with the applied position displacement to determine vertices that displayed significant error-related activity. The times shown in the plot correspond to the first time window in which vertices with significant error-related activity were detected within each ROI. The blue square and red triangles illustrate mean proprioceptive and visual error onset times respectively across subjects (n=7*). Error bars denote ± standard error across subjects (n=7)*. The motor delay of 13 ms was accounted for in all Proprioceptive teamporal measures. * For BA 17&18 (left) and parietal areas, 5,7 and 40, Subject CL2426 did not achieve statistical significance, and thus, for these areas, standard error represents a measure of 6 samples.

Figures C and D, show the average functional activation across subjects. Since the peak ROI activation does not necessarily occur at the same time across subjects, the peak activity is typically less than 1. In proprioceptive trials, functional activation peaked consistently across ROI's at 150 ms, and again at 275 ms (Figures 4.7 C and D). Interestingly, there was a sustained period of high functional activation in BA 7 shortly after the time of the first peak (150 ms) until the second peak (275 ms), which is also seen in BA 5, although at a lower level of activation. This pattern of activation for BA 7 is also seen for the Proprioceptive condition (although at a lower level of activation) and was consistent across subjects (Figure 4.7 C). In the Visual condition there was less synchronization of peak activation across ROI's. Peak functional activation in visual ROI's fell within two time windows, ~210 ms and 415 ms after displacement, although here there was less temporal bridging of activation in BA 7. Overall, in the Proprioceptive condition functional activation within the ROI's extended out to 374 ms, whereas for the Visual condition activation was seen well beyond 600 ms.

Proprioceptive Condition

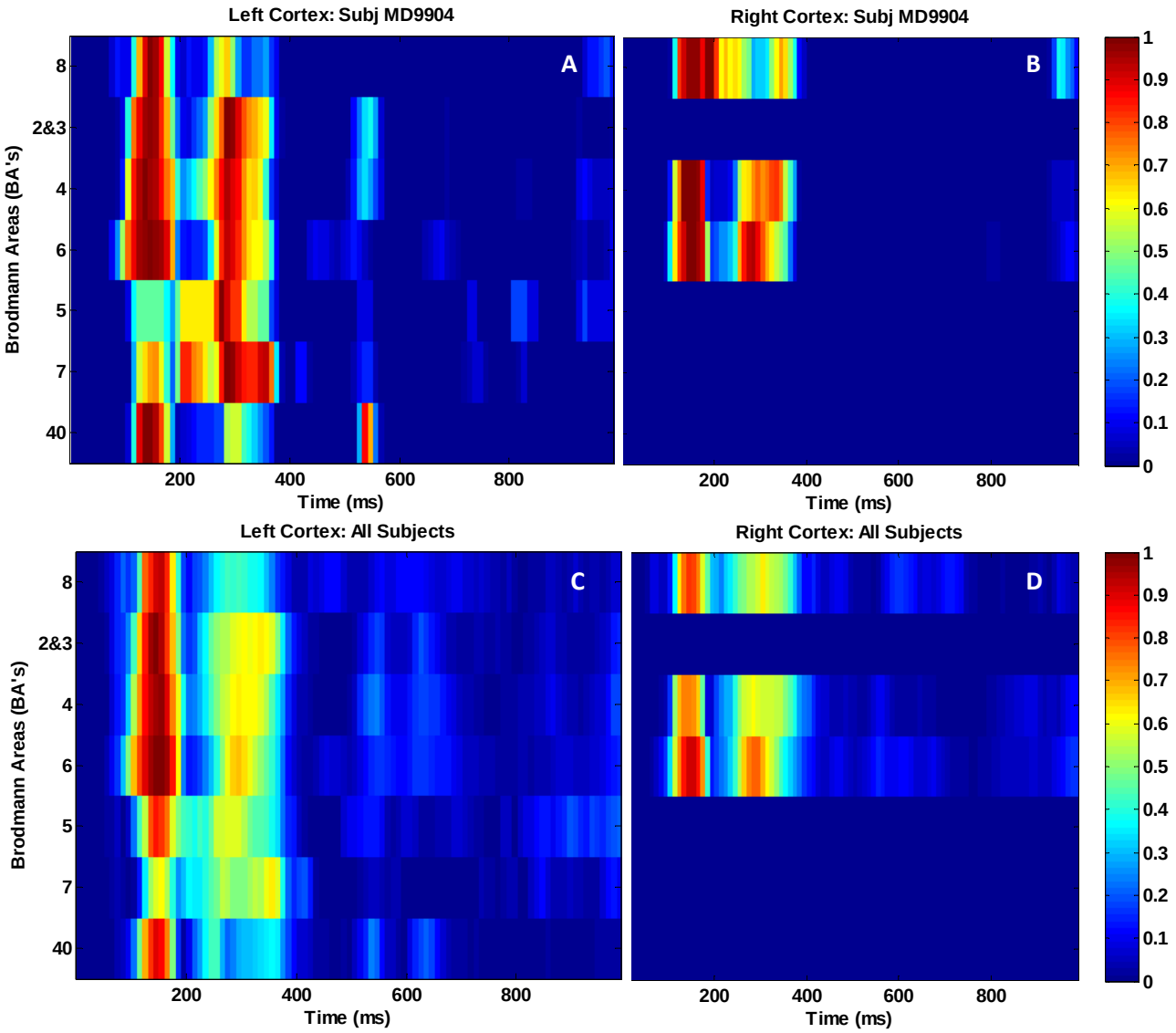

Figure 4.7: Functional activation across proprioceptive ROI's for a single subject (MD9904) and averaged across subjects. (A) and (B) show the integrated cortical activation of error-correlated vertices in left and right proprioceptive ROI's within each time window for a single subject. The magnitude of activation was computed as the total number of significantly activated vertices within each 50-ms time window and normalized by the total number of vertices in the ROI. (C) and (D) show results across all subjects for the proprioceptive condition.

Visual Condition

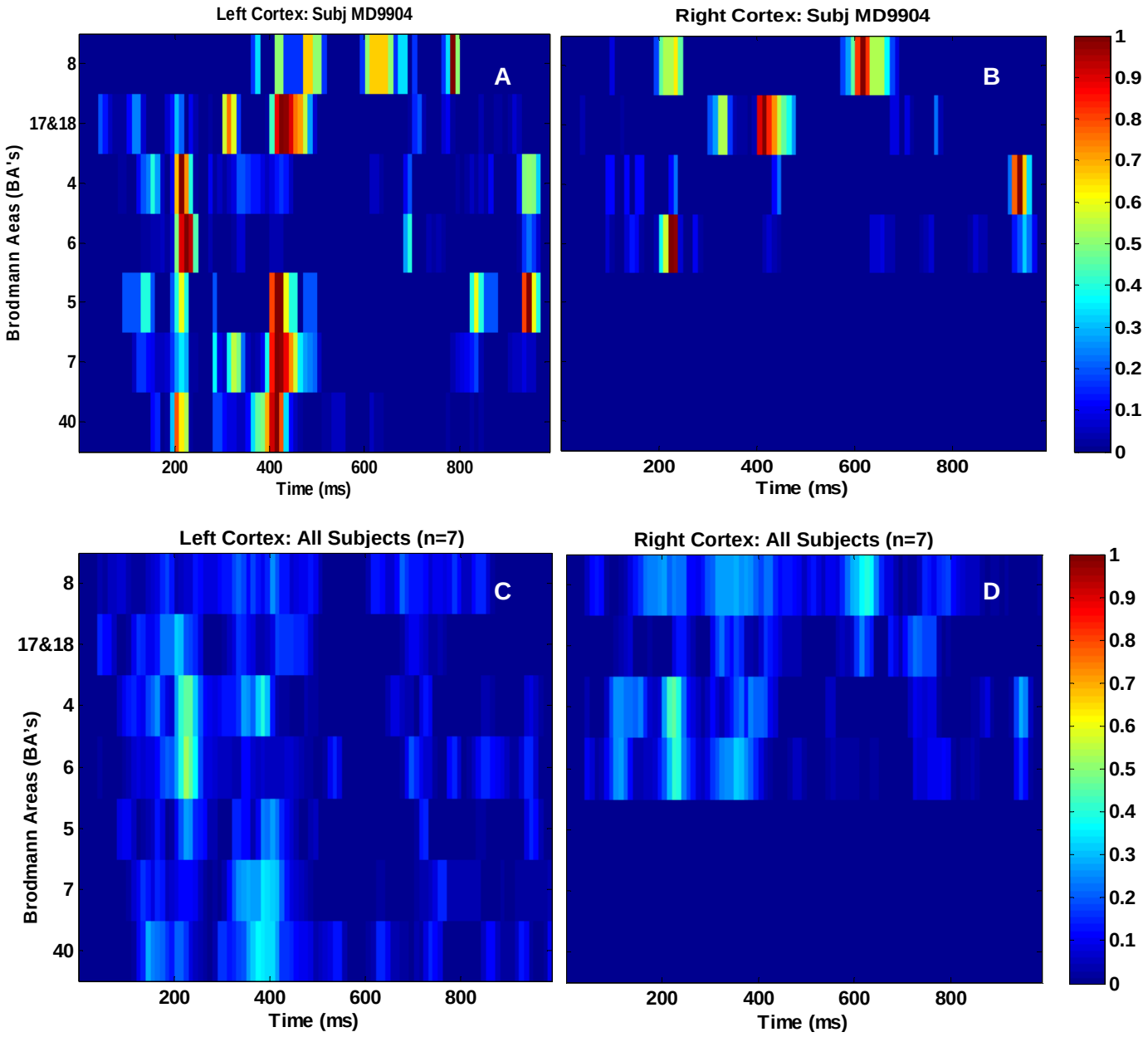

Figure 4.8: Functional activation across visual ROI's for a single subject (MD9904) and averaged across subjects. (A) and (B) show the integrated cortical activation of error-correlated vertices in left and right visual ROI's within each time window for a single subject. The magnitude of activation was computed as the total number of significantly activated vertices within each 50-ms time window and normalized by the total number of vertices in the ROI. (C) and (D) show results across all subjects in the Visual condition.

4.5 Spatial activation of cortical sources correlated with proprioceptive and visual error

To examine the spatial distribution of early source activity across subjects and conditions the centroids of significant activity within each ROI were calculated for three non-overlapping 50-ms time windows centered on the N100 response (Figure 4.9). ROI's are distinguished based on the centroid color (see figure caption) where darker colored centroids indicate centroids for the Proprioceptive condition and lighter colors indicate centroids for the Visual condition. Only centroids representing the unimodal sensory modalities (BA's 2&3 for proprioceptive and BA's 17&18 for visual) are depicted in a single color (black and white) as ROI responses were only measured within their respective modalities.

For perturbations sensed proprioceptively and visually there was a large overlap in centroid locations across all Brodmann areas. In order to provide a more quantitative measure of spatial differences between conditions, the Mahalanobis distance between Proprioceptive and Visual centroid distributions was calculated across subjects for each ROI (see Section 3.5.4). Figures 4.10 A through F show the distributions of Mahalanobis distances between proprioceptive and visual centroids for each ROI across subjects. The Mahalanobis measure of distance is similar to that of Euclidean with the exception that Mahalanobis takes into account the covariance of the two distributions. For our results, we used the interpretation of t-statistic distributions to identify areas with 'significant' mean separations. Of the 8 areas that were examined, areas 8 (left frontal), 5 & 7 (left parietal) were found to have large separations of mean distance above 2.5 units of distance (at 3, 4.5, and 2.5 units of distance respectively). This possibly suggests that error information may be computed in spatially distinct subregions of the frontal (BA 8) and parietal (BA's 5&7) areas.

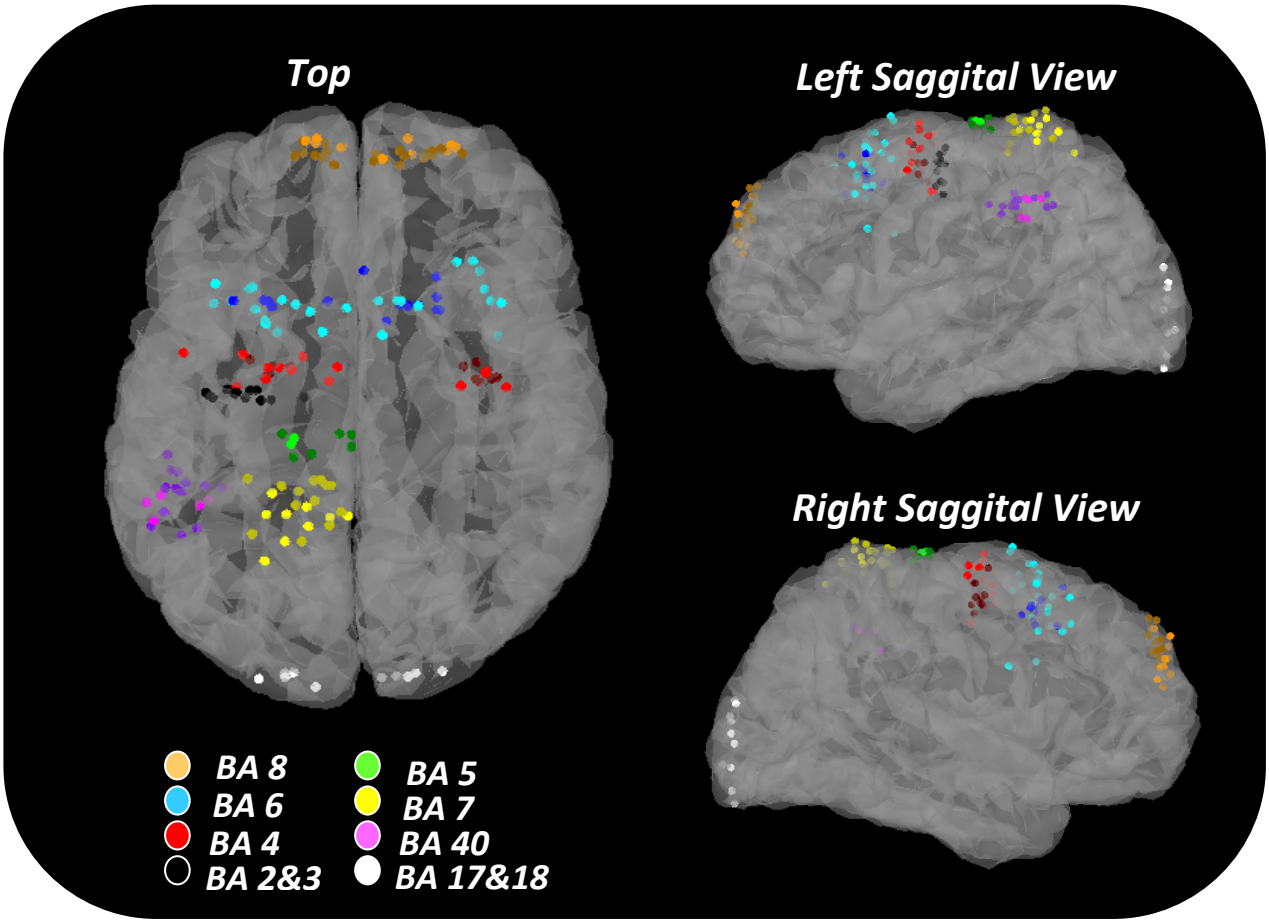

Figure 4.9: Spatial localization of initial source activity across ROI's in the Proprioceptive and Visual perturbation conditions. The cortical locations of centroids that were significantly correlated with error are shown across subjects. Centroids were measured as the average location of significantly activated vertices for each of the first three non-overlapping time windows (1st, 4th, and 9th time windows from the first point of significant activity). Centroid locations for the top (A), left saggital (B), and right saggital (C) views are shown with the ROI's distinguished by color (BA 8: orange; BA 6: blue; BA 4: red; BA's 2&3: black; BA's 17&18: white; BA 5: green; BA 7: yellow; and BA 40: purple). Visual and Proprioceptive conditions are distinguished by the shade of color (Proprioceptive: dark; Visual: light).

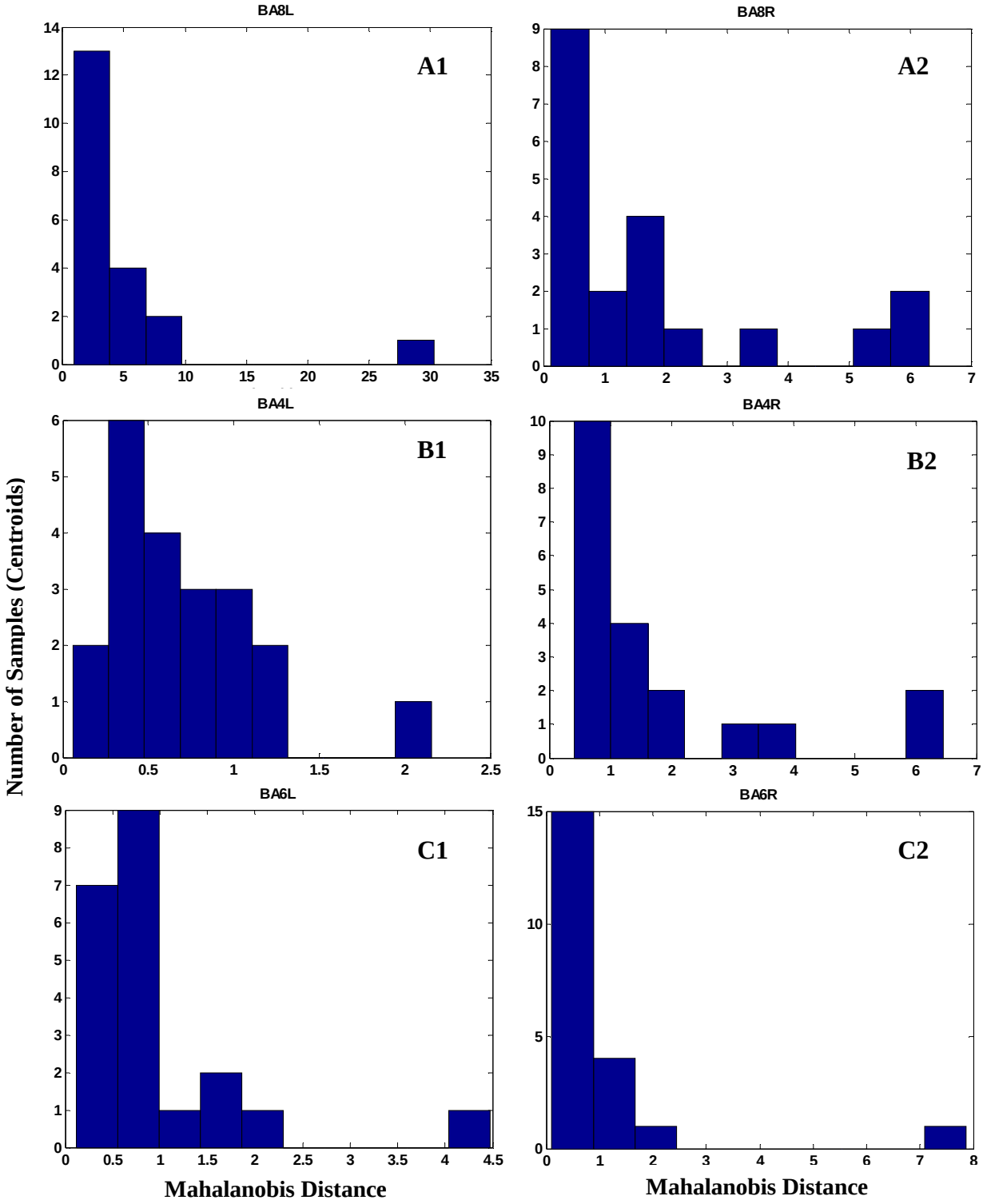
BA8L
A1
BA8R
A2
BA4L
B1
BA4R
B2
BA6L
C1
BA6R
C2
Number of Samples (Centroids)
Mahalanobis Distance
Mahalanobis Distance

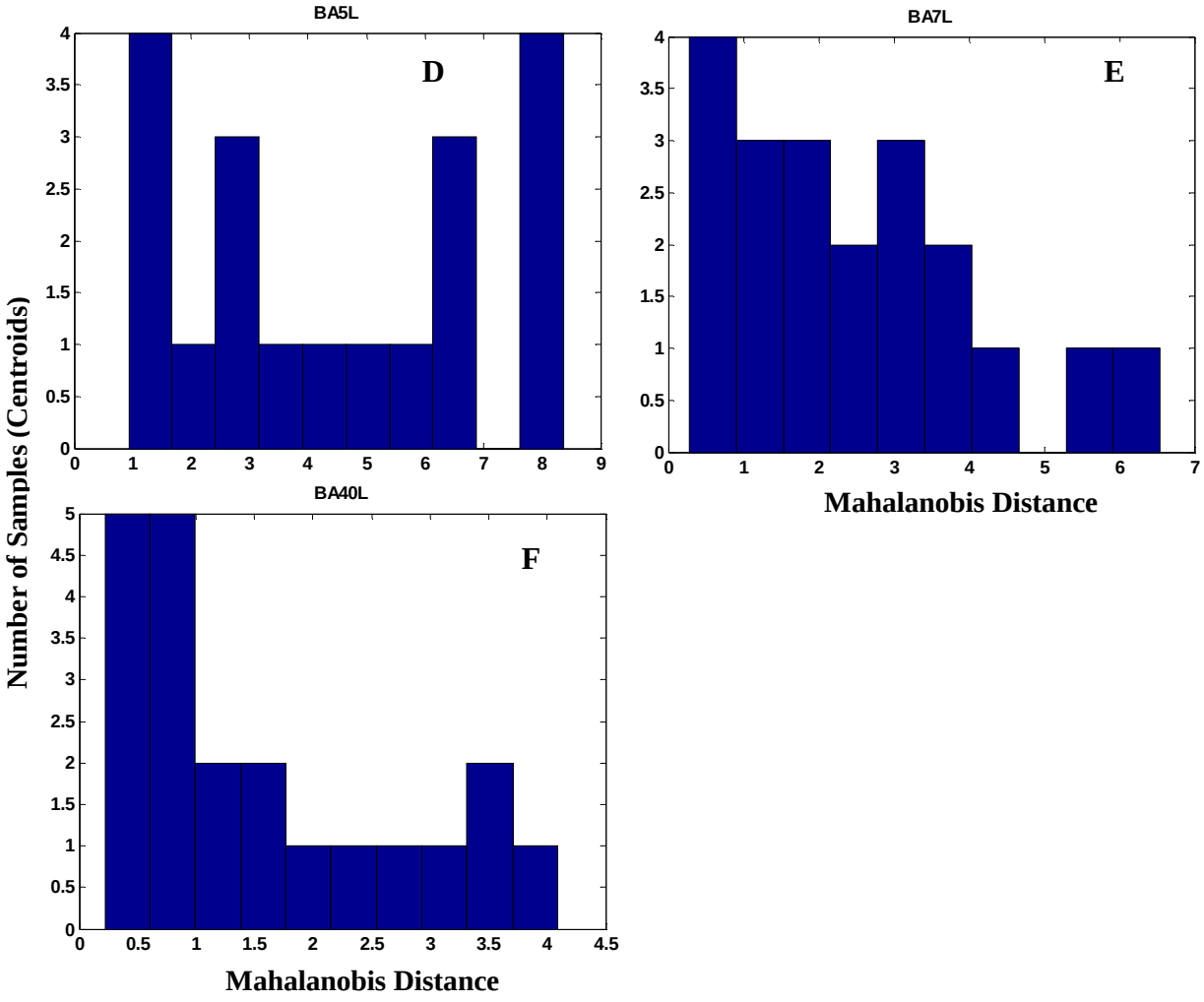

Figure 4.10: Distributions of Mahalanobis distances between centroids of activity in the proprioceptive and visual conditions across subjects. (A1&A2) Left and right frontal areas, BA8 ; (B1&B2) Left and right motor areas, BA 4; (C1&C2) Left and right premotor areas, BA6; (D) Left parietal, BA 5; (E) Left parietal, BA 7; (F) Left parietal, BA 40.

5 DISCUSSION

The purpose of this study was to characterize the cortical networks involved in the processing of and online correction of visual and proprioceptive errors during goal-directed movements. Thus, our experimental task was designed to dissociate error processing within the individual sensory pathways based on the type of external perturbation applied to the subjects as they performed a tracking task. The first type of perturbation applied forces to displace the subjects' wrist from the intended position, thereby generating a positional error which was sensed proprioceptively but not visually. The second applied visual position offsets to the subjects' cursor used to track the target, thus inducing a visual error in position which was sensed visually but not proprioceptively. We hypothesized that cortical processing, in response to the error, would result in early sensory activation of the unimodal sensory cortices, followed by parietal activation, and later still by premotor and motor activation tied to the subjects' subsequent correction. Based on the inherent differences in sensory processing times and how sensory information is represented in cortex, we expected to observe differences in the temporal and spatial dynamics of the cortical network involved in the online correction of visual and proprioceptive errors. Moreover, due to representation in the brain of visual and proprioceptive information in different coordinate frames; retinotopic coordinates in the case of vision (Andersen, Essick, Siegel 1985) and body-centered coordinates for proprioception (Brotchie et al., 1995; Mullette-Gillman, Cohen, Groh 2005), we hypothesized that unimodal estimates of error from the visual processing centers and somatosensory cortex would be integrated in the PPC to provide a combined representation of error.

Research that has examined the functional role of cortical activity relating to sensorimotor control of goal-directed movement has typically inferred neural function by relating observations of evoked neural responses (such as the N100 and P300) to the literature. Our research study aimed to probe deeper into the cortical control of movement by examining the sources that are activated in processing and correcting for externally applied error. Thus, we related EEG evoked responses to the activation of cortical source currents imaged on the scalp. This allowed us to directly compare the spatiotemporal dynamics of cortical activity resulting from external error to the functional roles of the brain areas examined. Another important distinction of our study to other studies in the literature that have applied source localization methods to image cortical activity is that they have typically made apriori assumptions on the number of sources and their locations in the brain. Our approach uses distributed source modeling to relax assumptions about the number of sources by assuming they are restricted in location to the cortical surface.

Temporal analyses of the relative timings in the sequence of ROI activation in response to displacement errors sensed proprioceptively and visually showed very different patterns of cortical activity than those predicted. In Proprioceptive trials, the first onset of error-related activity occurred in somatosensory cortex, followed by premotor, motor, and frontal activation, and finally by parietal activity. Visual trials resulted in parietal activation followed by sensory, premotor, and motor activation, and finally frontal activity. These results suggest that error is processed differently for proprioception and vision possibly to account for differences in how sensory information is relayed from the primary sensory cortices to higher processing areas.

While the temporal sequence of activation differed, spatial analyses of the cortical sources correlated to the task error showed significant commonalities in the cortical networks

involved in both conditions with the possible exception of parietal cortices. The spatial analyses were however unable to measure any differences between visual and proprioceptive distributions of centroid locations.

5.1 Differences in Evoked Responses to Visual and Proprioceptive Displacements

Across subjects, the evoked responses to an externally applied error produced two distinct phases of synchronous neural activity characterized by separate N100 and P300 peaks. The N100 occurred at 146.9 ± 4.5 ms in proprioceptive trials and 200.7 ± 6.5 ms in visual trials. The P300, on the other hand, was evoked 243.1 ± 15.9 ms following proprioceptive perturbation and at 351 ± 6.6 ms following visual perturbations. In a similar task, Krigolson and Holroyd (2007) observed the N100 and P300 in response to external displacements of a target during a visually-guided aiming task (Krigolson and Holroyd 2007). In their study a joystick was used to control the position of a visual cursor on the screen while subjects were exposed to either correctable diagonal displacements in target position (where displacements of the joystick produced a diagonal movement of the cursor on the screen) or uncorrectable displacements (where the joystick was unresponsive to diagonal displacements in cursor position thereby not allowing subjects to place the cursor on the target). The displacements introduced in the task initiated two types of error responses: ‘high-level’ errors that activated frontal brain regions to update performance goals and acknowledge the ‘failure’ of a system goal (i.e. not being able to correct for a displacement), and ‘low-level’ errors, involving parietal cortex, used to correct for small deviations in movement trajectory in order to bring the cursor back onto the target.

The evoked response to low-level errors measured in Krigolson and Holroyd’s experiment is structurally similar to our visually evoked response (Figure 4.3 B). Krigolson and

Holroyd observed the N100 response at 140 ms and the P300 at 324 ms, compared to 204 ms and 362 ms respectively in our visual trials. The timing of the ERP responses to visual perturbations in both studies appears to be similar for the P300 but different for the N100 (by ~ 64 ms). The differences in timing of the evoked responses could be due to several reasons including the manner in which visual perturbations were applied. In Krigolson and Holroyd's study, movement to the target was horizontal while visual displacements were applied vertically (i.e. the target moved diagonally upward or downward from its original position) which may have been easier to detect visually. Additionally, subjects were given a visual cue at the start of each trial to perform a reach toward the target and, as a result, were attentionally primed to perform a movement which may have allowed them to initiate quicker corrections to the perturbations. In our study, visual perturbations to cursor position were applied along the same plane of tracking movement (i.e. horizontally); thus, the detection of these perturbations may have been dependent to the velocity of cursor movement on the screen (e.g. smaller displacements would have been less easier to detect during faster movements of the wrist as their appearance may have been lost in the motion of the cursor on the screen). The increased delay in the N100 response to visual perturbations in our experiment could be indicative of additional time required to initiate a correction due to the delay in detecting visual displacements on the screen.

Comparison of evoked responses in Proprioceptive and Visual conditions shows a delay in the relative timings of the N100 and P300 across conditions (~ 60 ms). This delay in evoked responses stems from the different delays in processing for each sensory modality; visual processing occurs on the order of 200-250 ms and proprioceptive processing at 80-150 ms following stimulus onset (Flanders and Cordo 1989). In our experiment, position displacements were sensed earlier in the Proprioceptive condition, generating a neural response to the error and

a corrective movement toward the displacement earlier in time than for Visual trials. This interpretation is supported by the behavioral results which show that error corrections were completed 189.8 ± 22.3 ms earlier in Proprioceptive when compared to Visual trials.

In addition to the timing, proprioceptive and visual perturbations produced differences in the structure of the P300 peaks. The P300 in Visual trials contained a single peak while in Proprioceptive trials two subcomponents of the ERP were visible: the P3a and the P3b (Figure 4.3 A). Previous studies have typically associated the P3a with frontal activation and the allocation of attentional resources toward salient sensory stimuli while the P3b has been linked to activation of temporal-parietal cortical structures in response to the visual processing and detection of a target stimulus (Hill and Raab 2005b).

In our study, the application of impulse force perturbations was abrupt and may have disrupted the subject's attention to the task thus requiring additional attention towards performing the task accurately. The visual perturbations, although matched in magnitude to the proprioceptive perturbations were generally less disruptive in performing the tracking task. This could be due to the fact that the task required subjects to attend to the display screen (on which visual perturbations were applied), while the application of the forces in Proprioceptive trials caused subjects to shift their attention from the task presented on the screen to the displacement applied to their wrist. Polich and Criado (2006) found that single-peaked P300's were evoked with standard oddball paradigms. Separate P3a and P3b components were only visible in tasks that contained infrequent distracters which disrupted attention toward the task (Polich and Criado 2006). For the results reported here, error-related activity in response to force perturbations occurred first in sensory areas (at 42.7 ms), followed by premotor and motor (at 45.6 and 47 ms respectively) and frontal (at 48.4 ms) before any activity was measured in parietal areas, while

frontal activation in response to visual perturbations occurred much later than motor and parietal activation (at 212.8 ms). This is consistent with the interpretation that early frontal activity (corresponding to the P3a) in Proprioceptive trials reflects a shift in attentional demand (related to the size of the error) before error-related activity is processed in other areas.

The P3b response has been shown to be modulated by infrequent target stimuli (Menon et al., 1997), which in our study could correspond to unexpected displacements in wrist position. Hill and Raab (2005) showed that the amplitudes of the P3a and P3b were correlated with the magnitude of error applied. They proposed that larger errors elicited a higher attentional demand to ensure larger deviations in sensory stimuli were properly corrected for while small errors could be corrected quickly without allocating additional attentional resources to the task. Similar correlations of P300 magnitude to external proprioceptive and visual error are seen here, though the correlations are not as significant as those for the N100. This could suggest that the N100 response encodes the magnitude of externally-applied errors to correct for a large part of the error caused by the displacement, while the P300 may reflect later processing of the error to initiate smaller corrections to stabilize wrist response. This theory is revisited in the discussion of temporal source activation results in the following section.

5.2 Temporal Dynamics of Error Processing for Proprioceptive and Visual Conditions

Our initial hypothesis was that error-related activation would occur first in primary sensory cortices, then parietal areas to integrate sensory estimates of error and finally in motor or premotor cortices to initiate a correction to the error. Instead we found very different temporal pattern of activation between the Proprioceptive and Visual conditions. In the Proprioceptive condition, motor and premotor activation consistently occurred before parietal activation. Similar

activation times are seen across BA's 8, 4, and 6 in the left and right cortices for proprioception. The early motor (~ 47 ms) and premotor (~ 45.6ms) activity occurred well before a kinematic correction was initiated at the wrist (167.8 ms).

This initial representation of error could be associated with the initiation of a coarse error correction (i.e. moving the wrist in the direction of the target) before more detailed information pertaining to the magnitude and velocity of the target error is processed in parietal cortex. Day and Lyon (2000) showed that online reaching during visual displacements of a target evoked two types of kinematic responses following perturbation: one that occurred early (~ 125-160 ms) and a late response (after 160 ms (Day and Lyon 2000)). The early responses occurred in the direction of the target even when subjects were asked to consciously move opposite to the direction of target perturbation. Thus, subjects were unable to counter this early response by conscious will, which the authors suggest may be due to a preset neural mechanism for motor output to sensory stimuli in the environment. In their theoretical model, the authors propose that attention is first directed toward the target shift, which locks the automated visuomotor processing system onto the target and executes an automated adjustment of limb trajectory in the direction of the target (Day and Lyon 2000).

The CSD profiles in motor cortex (BA 4) show a similar pattern of activation in our results (Figure 4.4 A1) where an initial response at 58.6 ± 1.34 ms uncorrelated to the magnitude of error ($p=0.16$) is followed by two peaks (137.8 ± 2.28 ms and 213.8 ± 2.86 respectively), both of which are correlated to the error ($p<0.001$* and $p=0.08$). Interestingly, the timing of the first peak corresponds to the first estimate of error-related activity seen in BA 4 (at 60 ms), while timings of the second and third peaks in the Proprioceptive condition coincided with the occurrence of the N100 and P300 responses. Based on our working theory that the N100 is

representative of a major corrective response to the perturbation, we see that highly correlated activity in the motor cortex at 138 ms is followed by a kinematic correction at 168 ms. The difference in timing is consistent with the delay between the generation of a movement command in cortex and the corresponding kinematic response following the propagation of neural signals to the wrist and subsequent generation of muscle torques about the wrist.

The third less-correlated peak at 214 ms could be representative of a corrective stabilization response to the perturbations which allow fine-tuning of corrective wrist movements to bring the wrist back to baseline. In support of this theory, we see kinematic corrections to the perturbation subsequently returned to baseline following the third peak at 468 ms across levels. The low significance in correlation to displacement magnitude for this peak may be indicative of the fact that at the timing of the third peak, the applied displacement has been largely corrected for. Thus, relative differences in position of the wrist to the target across levels are less distinguishable across levels at the time of the third peak.

Functional activation plots displaying the time-course of error-related activity within each ROI for the Proprioceptive and Visual conditions further strengthen these observations (Figures 4.7 and 4.8). In the Proprioceptive condition, functional activation of error-correlated vertices within ROI's showed two waves of high error-related activity: one at 150 ms and another at 275 ms (see Figure 4.7). The first wave consists of synchronous activity between the frontal, motor, premotor, somatosensory, and parietal cortices, and occurs near the timing of the N100 response (at maximal wrist displacement) but before a kinematic correction is initiated. This suggests that premotor, motor, and parietal cortices work in concert to produce a motor output to correct for the error as functional activity across ROI's (except BA 7) is decreased after a correction is made (at 168 ms). The fact that BA 8 is only active during the first peak (when a correction is made)

supports the interpretation that it is involved in attending to the error, as by the timing of the second peak, the subject has already initiated a correction (Figure 4.1 A).

The second wave of activity occurs near the timing of the P300 and involves BA's 4, 6, 2&3, 5, and 7 (on the left) and BA's 4 and 6 (on the right). Studies have found P300 components to occur in the premotor, motor, and parietal areas (McDowell et al., 2002) and believe they are involved in evaluating the internal forward model in response to unpredictable events (Krigolson and Holroyd 2007). This may suggest that the brain evaluates the state of error in the motor system, and uses premotor, motor, and parietal cortices to initiate a second corrective response (during the second wave of activity) to stabilize the wrist and return it to baseline. Information may then be relayed to error processing centers (possibly the cerebellum) to update the internal forward model. In line with this theory, we see there is virtually no functional activation across ROI's following the second wave of corrections which is used to return wrist response to baseline (at 468 ms). Functional activation plots averaged across subjects (Figures 4.7 and 4.8 C and D) emphasize that the timing of the two waves of activity and involvement of the ROI's during peak functional activation is highly consistent across subjects.

BA 7 (and to a lesser degree BA 5) display a period of sustained error-related activity from the first wave to the second (Figure 4.7 A) which is also seen in the CSD profile during peak wrist displacement (i.e. from 140 to 190 ms – see Figure 4.5 A2). With the understanding that the first wave corresponds to a major corrective response to the perturbation while the second to a finer correction, this sustained activity in the parietal areas suggests that BA's 7 and 5 are more involved (compared to other ROI's) in processing error from the period of maximal wrist displacement through the majority of the corrective response initiated to return the wrist to baseline.

In the Visual condition, the temporal sequence of ROI activation differed from Proprioceptive trials: left parietal activation in areas 7 and 40, was followed by sensory activation in left visual cortex, and then bilateral motor, and premotor activation.

Current source density in BA 4 showed similar peaks of activity associated with a major corrective response to the perturbation (i.e. the peak at 341 ms corresponded to kinematic corrections initiated at 380 ms) and a finer corrective response at 607 ms allowed the cursor position to return to baseline at 657 ms. Unlike the Proprioceptive condition, however, the first correlated peak at 341 ms ($p<0.05$*) corresponded in timing to the P300 evoked response (at 362 ms) rather than the N100 (at 204 ms). These observations are supportive of the understanding that this pattern of corrective stabilization occurs across sensory modalities for both proprioceptive and visual error processing.

Peak functional activation across visual ROI's also showed two waves of activity at 210 ms and 415 ms, although the activity across ROI's was less consistent than in the Proprioceptive condition across subjects. Functional activation plots averaged across subjects show that the timings of peak activation seen in the single subject response (Figure 4.8 A and B) does not occur consistently in time across ROI's for all subjects (Figures 4.8 C and D). This may be due to the fact that CSD responses in the Visual condition contained a lot of noise and were highly variable (see Figures 4.4 B1 and B2). Thus, it is possible that the high variability in the number of significantly activated vertices in the Visual condition (that occurred randomly in time) may have averaged out actual signal responses correlated to the two waves of activity seen in subject MD9904.

Left motor, bilateral premotor, and left parietal (BA 40) were highly activated with the first wave of activity, followed by activation of the visual cortices and parietal BA's 5, 7 and 40

at the second wave of activity. The timings of the waves of activity coincide with the N100 and P300 evoked responses in the Visual condition (at roughly 204 and 362 ms). Although high activity was seen in motor and premotor at 204 ms, initiation of a corrective movement only occurred at 380 ms which may suggest that the first wave corresponded to a coarse representation of visual error in the motor and premotor areas (to plan and execute a correction to the perturbation). This coarse representation of error is also seen in the CSD for left BA 4 (Figure 4.4) at 212 ms (p=0.06).

The second wave of activity involved near-simultaneous activation of parietal areas BA's 5, 7, and 40, visual cortices BA's 17&18, and frontal areas and coincided to the timing of kinematic correction to the visual perturbation (~ 380 ms). The activation of frontal areas may indicate that additional attention was applied during the correction response (to ensure the correction occurred smoothly) while high parietal activation may indicate the areas were involved in evaluating the state of error in the system to bring the cursor back to baseline.

Interestingly, activation of parietal area 7 occurs first in the Visual condition before sensory or motor activation – the timing of this activation is ~40 ms after activation of area 7 in the Proprioceptive condition (i.e. 72.7 ms for Proprioceptive versus 113.3 ms for Visual). This could suggest that parietal area 7 is involved in the integration of individual sensory representations to compute a single multimodal estimate of error. Hyvarinen and Poranen observed a similar convergence of visual, somatic, and oculomotor activity in cells from area 7 of monkeys. They proposed that area 7 may be involved in integrating visual inputs with somatsensory information from parietal area 5 to provide an integrated estimate of spatial perception (Hyvarinen and Poranen 1974).

An important missing link in the analysis of these results is the relative contribution of the cerebellum which was not analyzed in this study. Studies have demonstrated the involvement of the cerebellum during visuomotor error processing of goal-directed movement (Kitazawa, Kimura, Yin 1998; Nadig et al., 2010; Suminski et al., 2007) and have implicated its role in error detection and correction (Criscimagna-Hemminger, Bastian, Shadmehr 2010; Thach, Goodkin, Keating 1992). It is possible that a representation of the error may have first been computed in the cerebellum and relayed to the motor and premotor cortices to form a coarse correction to the error while acquiring additional information pertaining to error magnitude and direction.

5.3 Spatial Dynamics of Proprioceptive and Visual Error Correlates

Although the low spatial resolution of EEG limits the ability to make fine spatial discriminations of neural activity, Figures 4.9 and 4.10 do show some coarse differences in the spatial distributions of the initial error-related activity across ROI's. Frontal area 8 (left) and parietal areas 5 and 7 (left) were found to have larger mean Mahalanobis distance separations for proprioceptive and visual centroids than other ROI's (above a threshold of 2). This may suggest that representations for error activity are computed/processed in distinct regions of the frontal and parietal areas across sensory modalities. Although our spatial analyses could not parse any significant differences from the distributions, future work could incorporate imaging modalities with high spatial resolution (such as fMRI, MEG) to measure spatial differences in visual and proprioceptive error processing.

6 FUTURE DIRECTIONS

In the current study, we sought to compare differences in processing errors sensed visually and proprioceptively during goal-directed movements. Utilizing the high temporal resolution of EEG together with source localization techniques, we were able to extract significant temporal differences between error onset times for several cortical ROI's in the two task conditions. Additionally, we were able to characterize, to a lesser extent, the spatial distribution of cortical areas whose activity was significantly correlated with the magnitude of externally applied error. Through this analysis we observed spatial differences in two subregions within the PPC: BA's 5 and 7, although the spatial sensitivity is limited by the poor spatial resolution of EEG.

Future studies could build on this approach to improve the spatiotemporal localization of sources by incorporating imaging modalities with higher spatial resolution, such as functional magnetic resonance imaging (fMRI) or magnetoencephalography (MEG), in addition to EEG. This would allow us to preserve the high temporal resolution of our results, while improving our ability to localize spatial differences in proprioceptive and visual sources not only on the cortical surface but also in cerebellum (fMRI). In order to include these imaging modalities in our study, changes to the experimental setup and task protocol would need to be made to make the system compatible with a magnetic environment. The electrical robot used in this study, for example, could not be used in either a MEG scanner (the electrical signals from the robot would disrupt the ability to record magnetic signals from the subjects' brains) nor in a MR-scanner. Thus, we could instead use a pneumatic manipulandum to apply force perturbations to the wrist.

Additional modifications can be made in the experimental design to control for external factors unrelated to active error processing. For example, the application of impulse forces to the

wrist in Proprioceptive trials introduced a possible confound: the passive properties of the wrist. Unlike the Visual condition, where we were easily able to detect the initiation of a kinematic correction to a visual displacement, proprioceptive corrections to applied forces introduced a passive correction (due to the spring-like properties of the wrist) making it dissociate the initiation of an active correction. To overcome this, we could instead apply constant force perturbations to the wrist (similar to the cursor displacements in Visual trials) at smaller levels of magnitude to counter any passive corrections of the wrist.

BIBLIOGRAPHY

Andersen RA and Buneo CA. 2002. Intentional maps in posterior parietal cortex Annual Review of Neuroscience 25:189-220.

Andersen RA, Essick GK, Siegel RM. 1985. Encoding of spatial location by posterior parietal neurons Science (New York, N.Y.) 230(4724):456-458.

Anguera JA, Seidler RD, Gehring WJ. 2009. Changes in performance monitoring during sensorimotor adaptation Journal of Neurophysiology 102(3):1868-1879.

Baillet S, Riera JJ, Marin G, Mangin JF, Aubert J, Garnero L. 2001. Evaluation of inverse methods and head models for EEG source localization using a human skull phantom Physics in Medicine and Biology 46(1):77-96.

Batista AP, Buneo CA, Snyder LH, Andersen RA. 1999. Reach plans in eye-centered coordinates Science (New York, N.Y.) 285(5425):257-260.

Batista AP, Santhanam G, Yu BM, Ryu SI, Afshar A, Shenoy KV. 2007. Reference frames for reach planning in macaque dorsal premotor cortex Journal of Neurophysiology 98(2):966-983.

Bernier PM, Burle B, Hasbroucq T, Blouin J. 2009. Spatio-temporal dynamics of reach-related neural activity for visual and somatosensory targets NeuroImage 47(4):1767-1777.

Blangero A, Ota H, Delporte L, Revol P, Vindras P, Rode G, Boisson D, Vighetto A, Rossetti Y, Pisella L. 2007. Optic ataxia is not only 'optic': Impaired spatial integration of proprioceptive information NeuroImage 36 Suppl 2:T61-8.

Brotchie PR, Andersen RA, Snyder LH, Goodman SJ. 1995. Head position signals used by parietal neurons to encode locations of visual stimuli Nature 375(6528):232-235.

Buneo CA and Andersen RA. 2006. The posterior parietal cortex: Sensorimotor interface for the planning and online control of visually guided movements Neuropsychologia 44(13):2594-2606.

Buneo CA, Jarvis MR, Batista AP, Andersen RA. 2002. Direct visuomotor transformations for reaching Nature 416(6881):632-636.

Caminiti R, Johnson PB, Galli C, Ferraina S, Burnod Y. 1991. Making arm movements within different parts of space: The premotor and motor cortical representation of a coordinate system for reaching to visual targets The Journal of Neuroscience : The Official Journal of the Society for Neuroscience 11(5):1182-1197.

Cohen YE and Andersen RA. 2002. A common reference frame for movement plans in the posterior parietal cortex Nature Reviews.Neuroscience 3(7):553-562.

Colby CL, Duhamel JR, Goldberg ME. 1993. Ventral intraparietal area of the macaque: Anatomic location and visual response properties Journal of Neurophysiology 69(3):902-914.

Colby CL and Duhamel J. 1991. Heterogeneity of extrastriate visual areas and multiple parietal areas in the macaque monkey Neuropsychologia 29(6):517 <last_page> 537.

Criscimagna-Hemminger SE, Bastian AJ, Shadmehr R. 2010. Size of error affects cerebellar contributions to motor learning Journal of Neurophysiology .

Culham JC, Cavina-Pratesi C, Singhal A. 2006. The role of parietal cortex in visuomotor control: What have we learned from neuroimaging? Neuropsychologia 44(13):2668-2684.

Culham JC, Danckert SL, DeSouza JF, Gati JS, Menon RS, Goodale MA. 2003. Visually guided grasping produces fMRI activation in dorsal but not ventral stream brain areas Experimental Brain Research.Experimentelle Hirnforschung.Experimentation Cerebrale 153(2):180-189.

Day BL and Lyon IN. 2000. Voluntary modification of automatic arm movements evoked by motion of a visual target Experimental Brain Research.Experimentelle Hirnforschung.Experimentation Cerebrale 130(2):159-168.

Debener S, Ullsperger M, Siegel M, Fiehler K, von Cramon DY, Engel AK. 2005. Trial-by-trial coupling of concurrent electroencephalogram and functional magnetic resonance imaging identifies the dynamics of performance monitoring The Journal of Neuroscience : The Official Journal of the Society for Neuroscience 25(50):11730-11737.

Desmurget M and Grafton S. 2000. Forward modeling allows feedback control for fast reaching movements Trends in Cognitive Sciences 4(11):423-431.

Diedrichsen J, Hashambhoy Y, Rane T, Shadmehr R. 2005. Neural correlates of reach errors The Journal of Neuroscience : The Official Journal of the Society for Neuroscience 25(43):9919-9931.

Duhamel, Colby C, Goldberg M. 1992. The updating of the representation of visual space in parietal cortex by intended eye movements Science 255(5040):90 <last_page> 92.

Duhamel JR, Bremmer F, BenHamed S, Graf W. 1997. Spatial invariance of visual receptive fields in parietal cortex neurons Nature 389(6653):845-848.

Faugier-Grimaud S and Ventre J. 1989. Anatomic connections of inferior parietal cortex (area 7) with subcortical structures related to vestibulo-ocular function in a monkey (macaca fascicularis) The Journal of Comparative Neurology 280(1):1-14.

Felician O, Romaiguere P, Anton JL, Nazarian B, Roth M, Poncet M, Roll JP. 2004. The role of human left superior parietal lobule in body part localization Annals of Neurology 55(5):749-751.

Ferraina S, Johnson PB, Garasto MR, Battaglia-Mayer A, Ercolani L, Bianchi L, Lacquaniti F, Caminiti R. 1997. Combination of hand and gaze signals during reaching: Activity in parietal area 7 m of the monkey Journal of Neurophysiology 77(2):1034-1038.

Flanders M and Cordo PJ. 1989. Kinesthetic and visual control of a bimanual task: Specification of direction and amplitude The Journal of Neuroscience : The Official Journal of the Society for Neuroscience 9(2):447-453.

Galati G, Committeri G, Sanes JN, Pizzamiglio L. 2001. Spatial coding of visual and somatic sensory information in body-centred coordinates The European Journal of Neuroscience 14(4):737-746.

Garavan H, Ross TJ, Murphy K, Roche RA, Stein EA. 2002. Dissociable executive functions in the dynamic control of behavior: Inhibition, error detection, and correction NeuroImage 17(4):1820-1829.

Gentilini M, Barbieri C, De Renzi E, Faglioni P. 1989. Space exploration with and without the aid of vision in hemisphere-damaged patients Cortex; a Journal Devoted to the Study of the Nervous System and Behavior 25(4):643-651.

Glickstein M. 2000. How are visual areas of the brain connected to motor areas for the sensory guidance of movement? Trends in Neurosciences 23(12):613-617.

Grafton ST, Schmitt P, Van Horn J, Diedrichsen J. 2008. Neural substrates of visuomotor learning based on improved feedback control and prediction NeuroImage 39(3):1383-1395.

Graziano MS, Yap GS, Gross CG. 1994. Coding of visual space by premotor neurons Science (New York, N.Y.) 266(5187):1054-1057.

Gréa H. 2002. A lesion of the posterior parietal cortex disrupts on-line adjustments during aiming movements Neuropsychologia 40(13):2471 <last_page> 2480.

Haaland KY. 2000. Neural representations of skilled movement Brain 123(11):2306 <last_page> 2313.

Haggard P. 2005. Conscious intention and motor cognition Trends in Cognitive Sciences 9(6):290-295.

Halsband U and Lange RK. 2006. Motor learning in man: A review of functional and clinical studies Journal of Physiology, Paris 99(4-6):414-424.

Hill H and Raab M. 2005a. Analyzing a complex visuomotor tracking task with brain-electrical event related potentials Human Movement Science 24(1):1-30.

Hill H and Raab M. 2005b. Analyzing a complex visuomotor tracking task with brain-electrical event related potentials Human Movement Science 24(1):1-30.

Holroyd CB and Coles MG. 2002. The neural basis of human error processing: Reinforcement learning, dopamine, and the error-related negativity Psychological Review 109(4):679-709.

Hyvarinen J and Poranen A. 1974. Function of the parietal associative area 7 as revealed from cellular discharges in alert monkeys Brain : A Journal of Neurology 97(4):673-692.

Iacoboni M and Dapretto M. 2006. The mirror neuron system and the consequences of its dysfunction Nature Reviews.Neuroscience 7(12):942-951.

Imamizu H, Kuroda T, Miyauchi S, Yoshioka T, Kawato M. 2003. Modular organization of internal models of tools in the human cerebellum Proceedings of the National Academy of Sciences of the United States of America 100(9):5461-5466.

Johnson-Frey SH, Newman-Norlund R, Grafton ST. 2005. A distributed left hemisphere network active during planning of everyday tool use skills Cerebral Cortex (New York, N.Y.: 1991) 15(6):681-695.

Kalaska JF, Scott SH, Cisek P, Sergio LE. 1997. Cortical control of reaching movements Current Opinion in Neurobiology 7(6):849-859.

Karnath HO, Niemeier M, Dichgans J. 1998. Space exploration in neglect Brain : A Journal of Neurology 121 (Pt 12)(Pt 12):2357-2367.

Kasai T, Morotomi T, Katayama J, Kumada T. 2003. Attending to a location in three-dimensional space modulates early ERPs Brain Research.Cognitive Brain Research 17(2):273-285.

Kitazawa S, Kimura T, Yin PB. 1998. Cerebellar complex spikes encode both destinations and errors in arm movements Nature 392(6675):494-497.

Krigolson O and Heath M. 2004. Background visual cues and memory-guided reaching Human Movement Science 23(6):861-877.

Krigolson OE and Holroyd CB. 2007. Hierarchical error processing: Different errors, different systems. Brain Research 1155:70-80.

Libet B, Gleason CA, Wright EW, Pearl DK. 1983. Time of conscious intention to act in relation to onset of cerebral activity (readiness-potential). the unconscious initiation of a freely voluntary act Brain : A Journal of Neurology 106 (Pt 3)(Pt 3):623-642.

Lindin M, Zurron M, Diaz F. 2005. Stimulus intensity effects on P300 amplitude across repetitions of a standard auditory oddball task Biological Psychology 69(3):375-385.

Maimon G. 2006. Parietal area 5 and the initiation of self-timed movements versus simple reactions Journal of Neuroscience 26(9):2487 <last_page> 2498.

Mars RB, Coles MG, Grol MJ, Holroyd CB, Nieuwenhuis S, Hulstijn W, Toni I. 2005. Neural dynamics of error processing in medial frontal cortex NeuroImage 28(4):1007-1013.

McDowell K, Jeka JJ, Schoner G, Hatfield BD. 2002. Behavioral and electrocortical evidence of an interaction between probability and task metrics in movement preparation Experimental Brain Research.Experimentelle Hirnforschung.Experimentation Cerebrale 144(3):303-313.

Menon V, Ford JM, Lim KO, Glover GH, Pfefferbaum A. 1997. Combined event-related fMRI and EEG evidence for temporal-parietal cortex activation during target detection Neuroreport 8(14):3029-3037.

Meredith MA and Stein BE. 1986. Visual, auditory, and somatosensory convergence on cells in superior colliculus results in multisensory integration Journal of Neurophysiology 56(3):640-662.

Miall RC, Imamizu H, Miyauchi S. 2000. Activation of the cerebellum in co-ordinated eye and hand tracking movements: An fMRI study Experimental Brain Research.Experimentelle Hirnforschung.Experimentation Cerebrale 135(1):22-33.

Miltner WHR, Braun CH, Coles MGH. 1997. Event-related brain potentials following incorrect feedback in a time-estimation task: Evidence for a “Generic” neural system for error detection Journal of Cognitive Neuroscience 9(6):788 <last_page> 798.

Mosher JC, Leahy RM, Lewis PS. 1999. EEG and MEG: Forward solutions for inverse methods IEEE Transactions on Bio-Medical Engineering 46(3):245-259.

Mountcastle VB, Lynch JC, Georgopoulos A, Sakata H, Acuna C. 1975. Posterior parietal association cortex of the monkey: Command functions for operations within extrapersonal space Journal of Neurophysiology 38(4):871-908.

Mullette-Gillman OA, Cohen YE, Groh JM. 2005. Eye-centered, head-centered, and complex coding of visual and auditory targets in the intraparietal sulcus Journal of Neurophysiology 94(4):2331-2352.

Naatanen R and Michie PT. 1979. Early selective-attention effects on the evoked potential: A critical review and reinterpretation Biological Psychology 8(2):81-136.

Nadig KG, Jancke L, Luchinger R, Lutz K. 2010. Motor and non-motor error and the influence of error magnitude on brain activity Experimental Brain Research.Experimentelle Hirnforschung.Experimentation Cerebrale 202(1):45-54.

Naranjo JR, Brovelli A, Longo R, Budai R, Kristeva R, Battaglini PP. 2007. EEG dynamics of the frontoparietal network during reaching preparation in humans NeuroImage 34(4):1673-1682.

Nishitani N, Uutela K, Shibasaki H, Hari R. 1999. Cortical visuomotor integration during eye pursuit and eye-finger pursuit The Journal of Neuroscience : The Official Journal of the Society for Neuroscience 19(7):2647-2657.

Pazo-Alvarez P, Amenedo E, Lorenzo-Lopez L, Cadaveira F. 2004. Effects of stimulus location on automatic detection of changes in motion direction in the human brain Neuroscience Letters 371(2-3):111-116.

Perenin MT and Vighetto A. 1988. Optic ataxia: A specific disruption in visuomotor mechanisms. I. different aspects of the deficit in reaching for objects Brain : A Journal of Neurology 111 (Pt 3)(Pt 3):643-674.

Polich J. 2007. Updating P300: An integrative theory of P3a and P3b Clinical Neurophysiology : Official Journal of the International Federation of Clinical Neurophysiology 118(10):2128-2148.

Polich J and Criado JR. 2006. Neuropsychology and neuropharmacology of P3a and P3b International Journal of Psychophysiology : Official Journal of the International Organization of Psychophysiology 60(2):172-185.

Robinson DA and Fuchs AF. 1969. Eye movements evoked by stimulation of frontal eye fields Journal of Neurophysiology 32(5):637-648.

Rondot P, de Recondo J, Dumas JL. 1977. Visuomotor ataxia Brain : A Journal of Neurology 100(2):355-376.

Sasaki K and Gemba H. 1987. Plasticity of cortical function related to voluntary movement motor learning and compensation following brain dysfunction Acta Neurochirurgica.Supplementum 41:18-28.

Scott SH. 2004. Optimal feedback control and the neural basis of volitional motor control Nature Reviews.Neuroscience 5(7):532-546.

Semlitsch HV, Anderer P, Schuster P, Presslich O. 1986. A solution for reliable and valid reduction of ocular artifacts, applied to the P300 ERP Psychophysiology 23(6):695-703.

Serrien DJ and Wiesendanger M. 2000. Temporal control of a bimanual task in patients with cerebellar dysfunction Neuropsychologia 38(5):558-565.

Stein JF and Glickstein M. 1992. Role of the cerebellum in visual guidance of movement Physiological Reviews 72(4):967-1017.

Suminski AJ, Rao SM, Mosier KM, Scheidt RA. 2007. Neural and electromyographic correlates of wrist posture control Journal of Neurophysiology 97(2):1527-1545.

Swick D and Turken AU. 2002. Dissociation between conflict detection and error monitoring in the human anterior cingulate cortex Proceedings of the National Academy of Sciences of the United States of America 99(25):16354-16359.

Thach WT, Goodkin HP, Keating JG. 1992. The cerebellum and the adaptive coordination of movement Annual Review of Neuroscience 15:403-442.

Vercher JL and Gauthier GM. 1988. Cerebellar involvement in the coordination control of the oculo-manual tracking system: Effects of cerebellar dentate nucleus lesion Experimental Brain Research.Experimentelle Hirnforschung.Experimentation Cerebrale 73(1):155-166.

Wheaton L, Fridman E, Bohlhalter S, Vorbach S, Hallett M. 2009. Left parietal activation related to planning, executing and suppressing praxis hand movements Clinical Neurophysiology : Official Journal of the International Federation of Clinical Neurophysiology 120(5):980-986.

Wolpert DM and Ghahramani Z. 2000. Computational principles of movement neuroscience Nature Neuroscience 3 Suppl:1212-1217.

Zang Y. 2003. Functional organization of the primary motor cortex characterized by event-related fMRI during movement preparation and execution Neuroscience Letters 337(2):69-72.

Zilles K and Palomero-Gallagher N. 2001. Cyto-, myelo-, and receptor architectonics of the human parietal cortex NeuroImage 14(1 Pt 2):S8-20.

APPENDICES

Appendix A: Averaged Behavioral Response

The following figures illustrate single-subject behavioral wrist and cursor responses to Proprioceptive and Visual perturbations. Proprioceptive perturbations applied to the wrist at 5 levels of displacement (L1 to L5) generated error in position between target and wrist position. Likewise, Visual perturbations generated error in cursor position relative to target. Low-pass filtered position, velocity, and acceleration responses to the perturbations are shown below (30 Hz; low-pass 4th order Butterworth).

Subject AV7089: Proprioceptive Condition

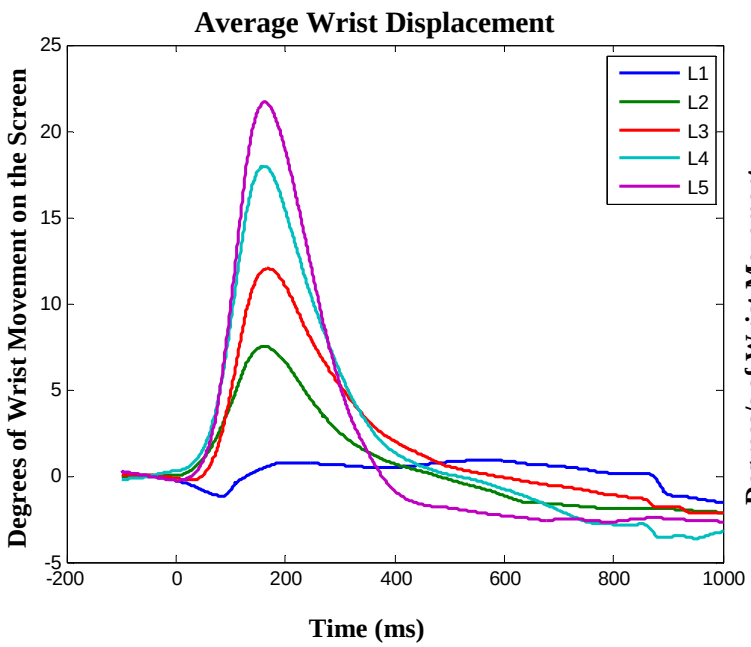

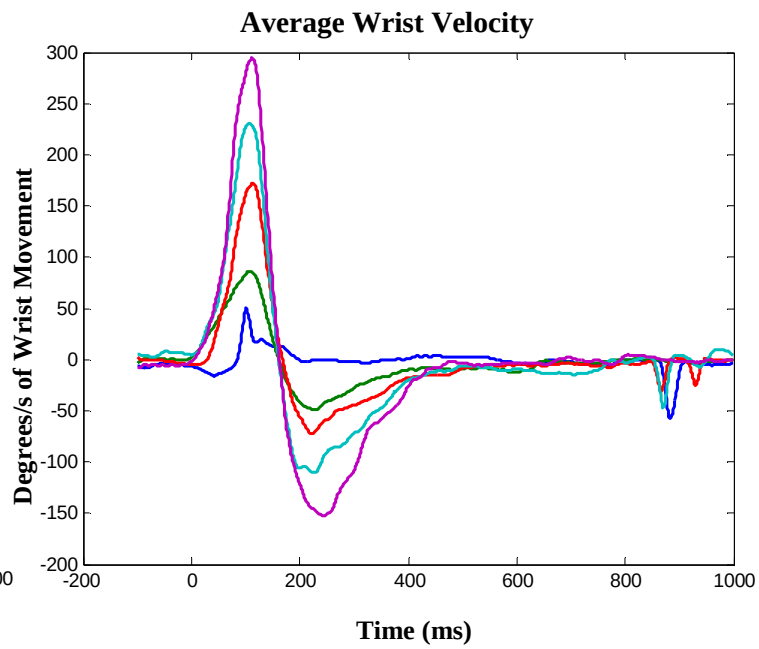

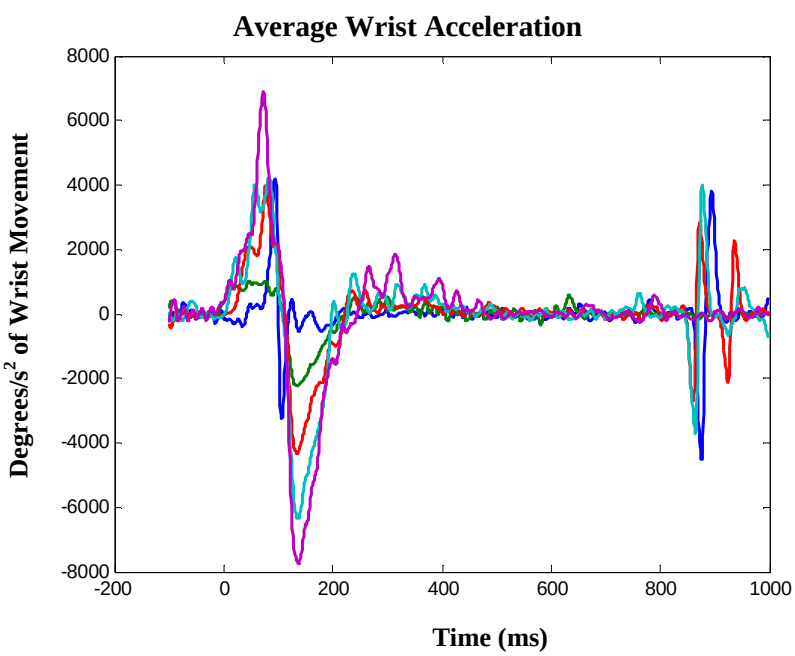

Subject AV7089: Visual Condition

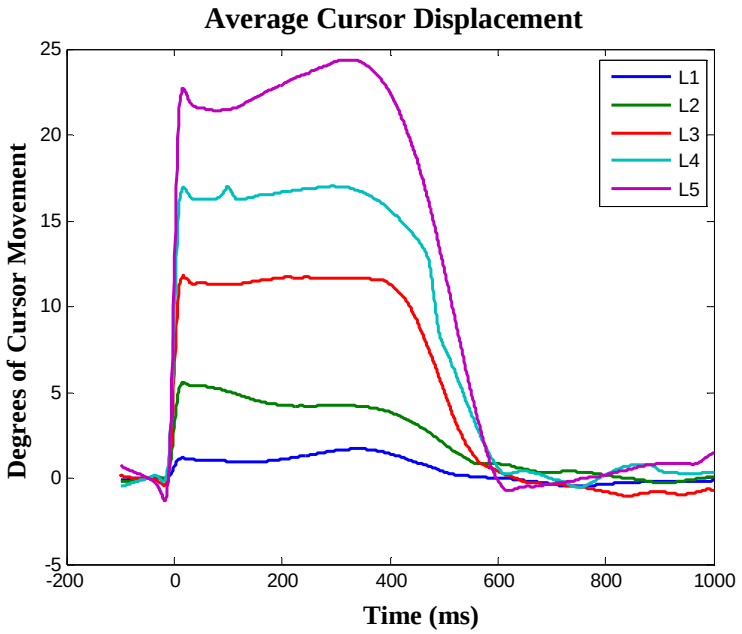

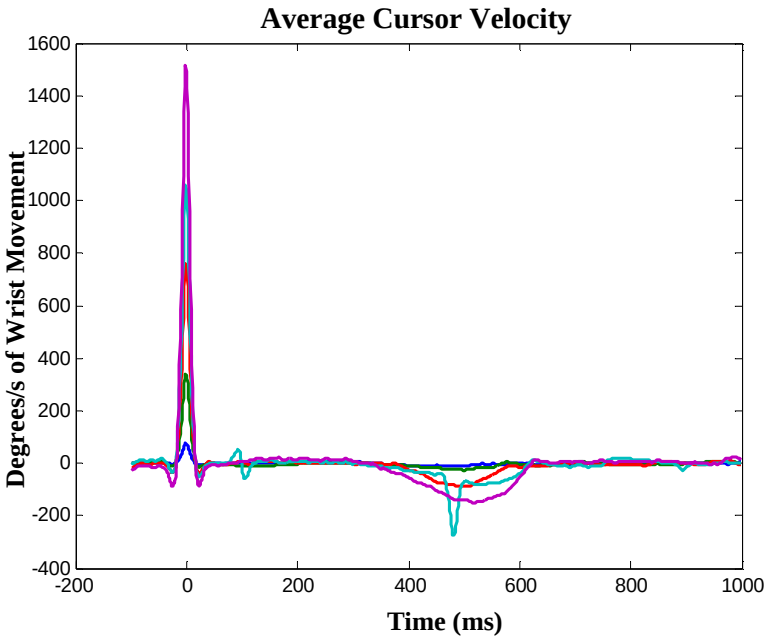

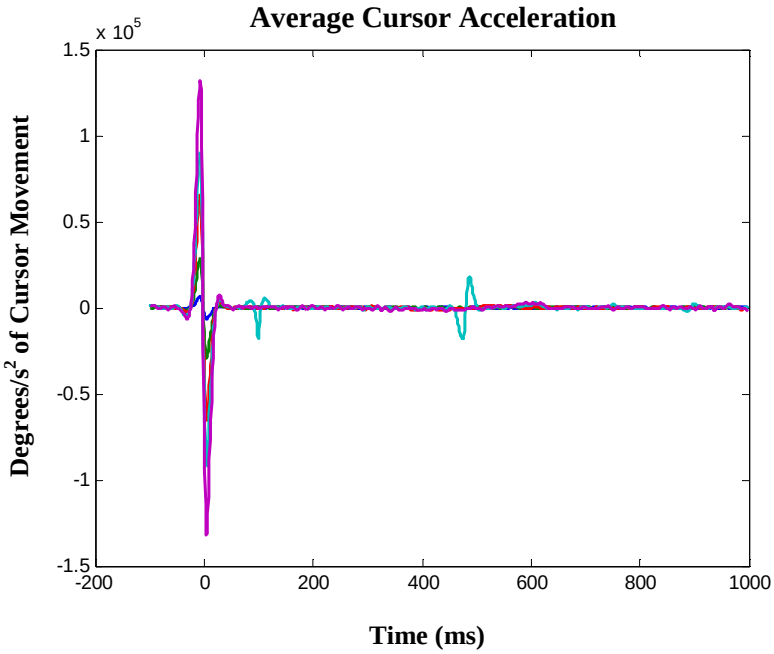

Subject CL2426: Proprioceptive Condition

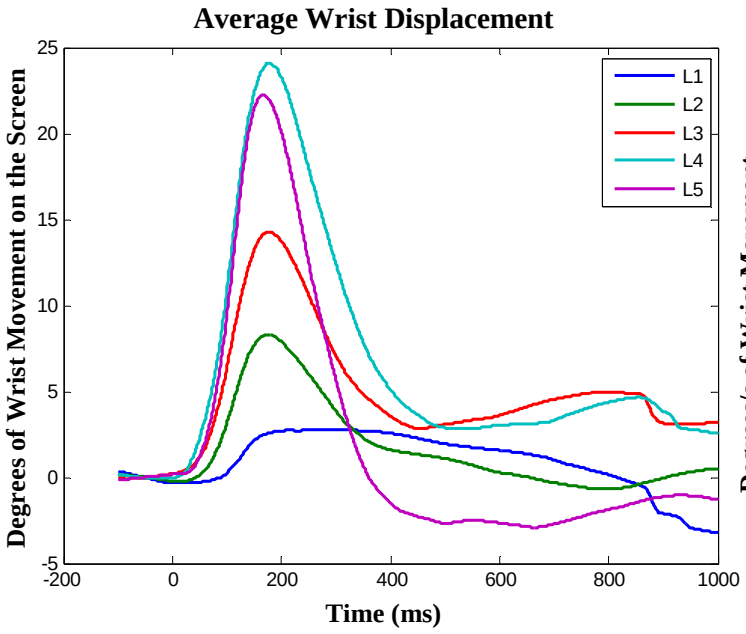

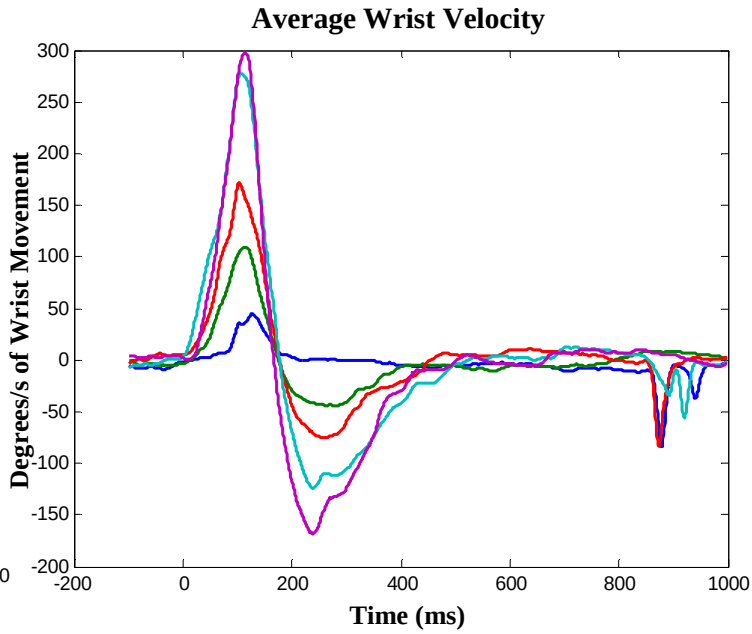

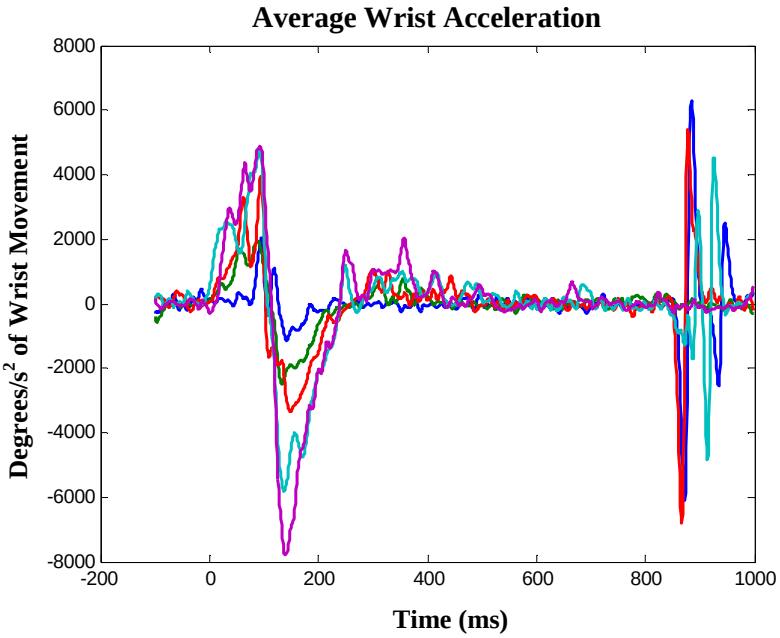

Subject CL2426: Visual Condition

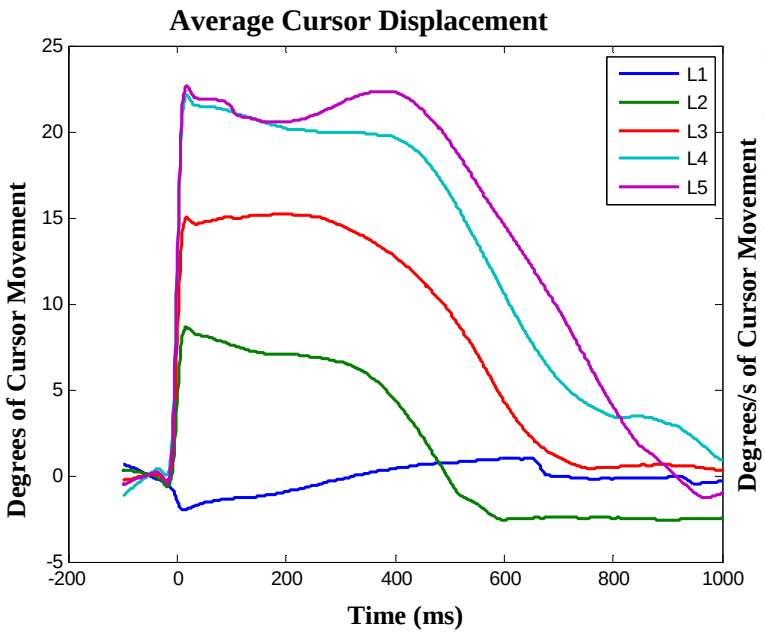

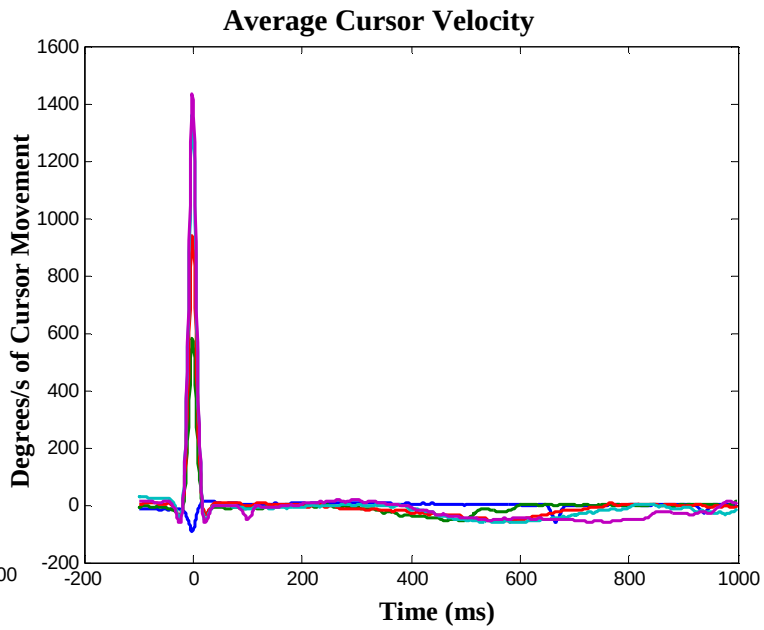

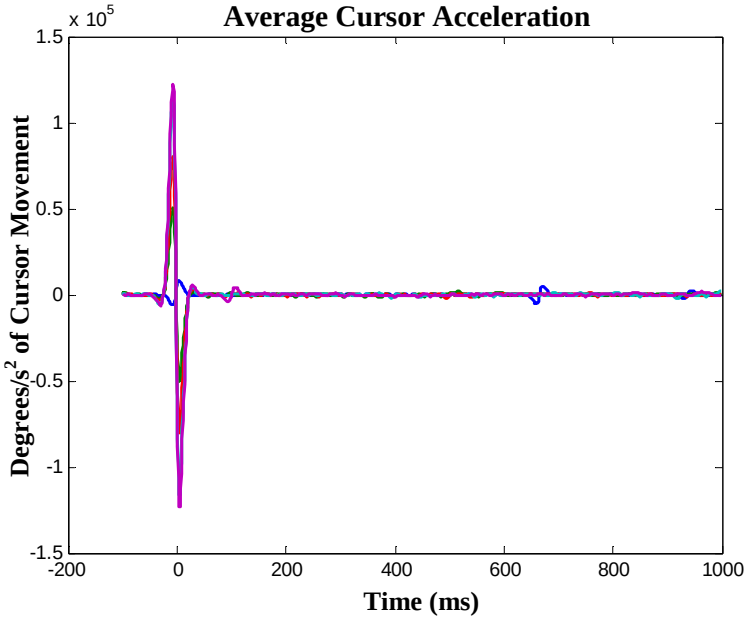

Subject MD9904: Proprioceptive Condition

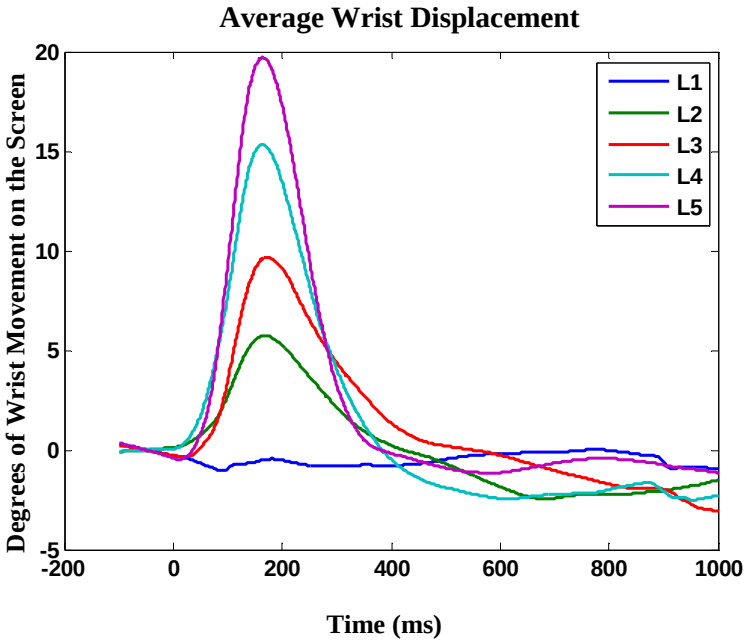

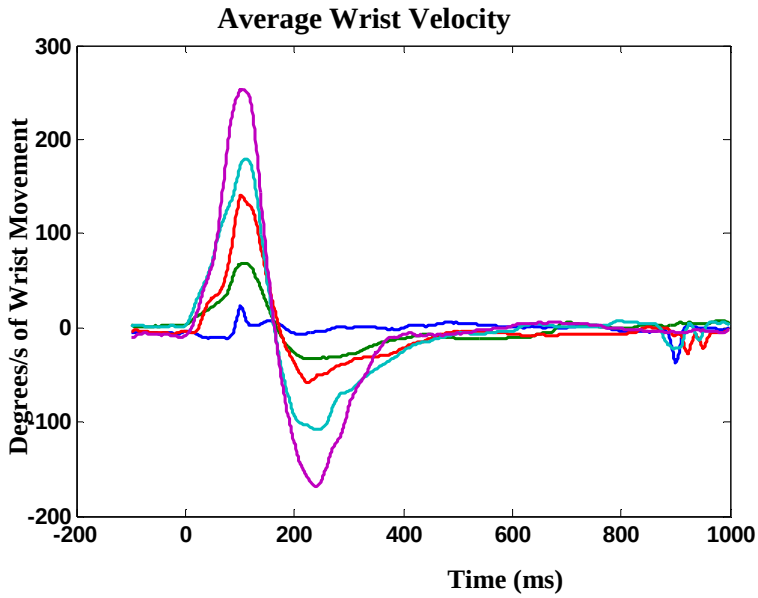

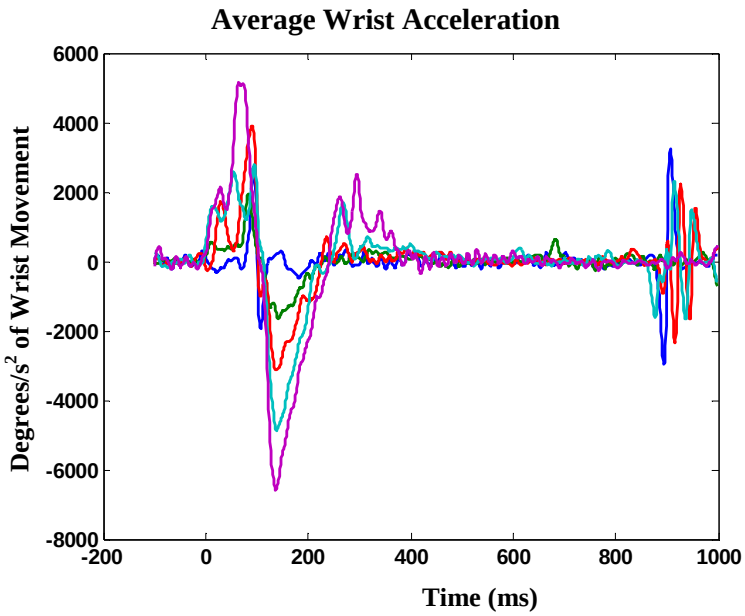

Subject MD9904: Visual Condition

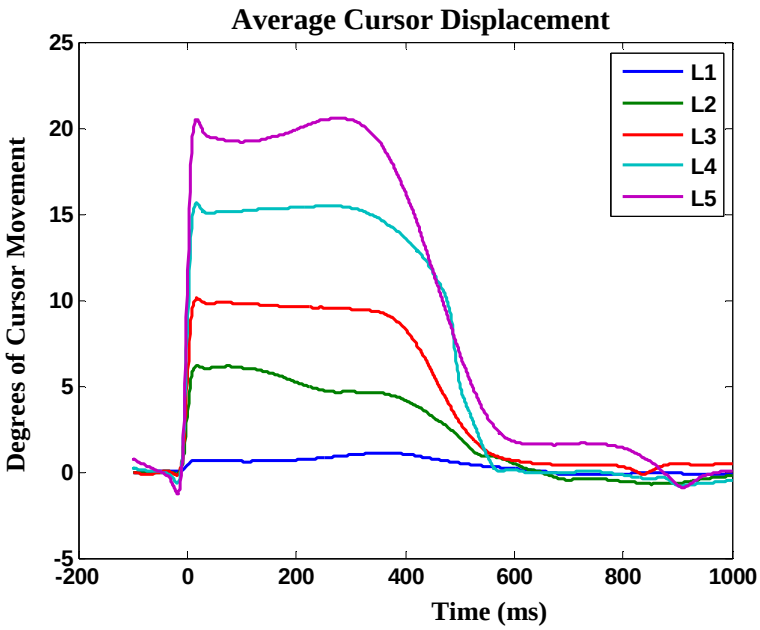

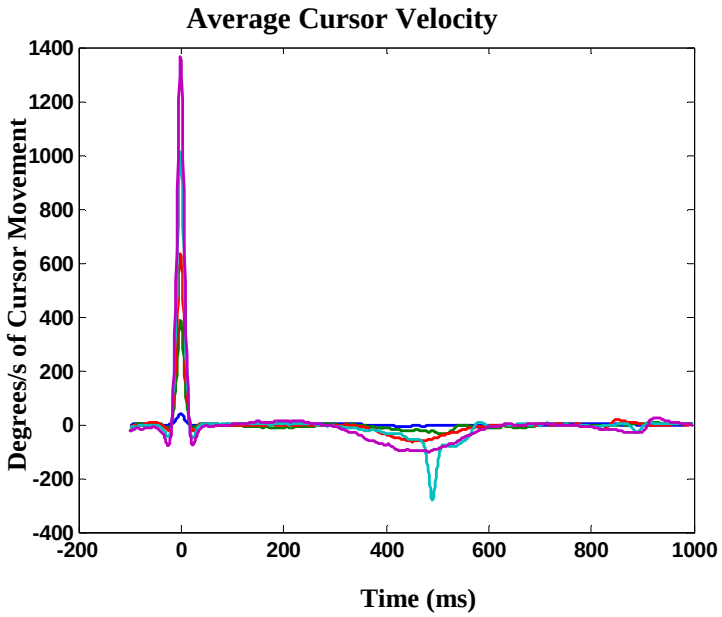

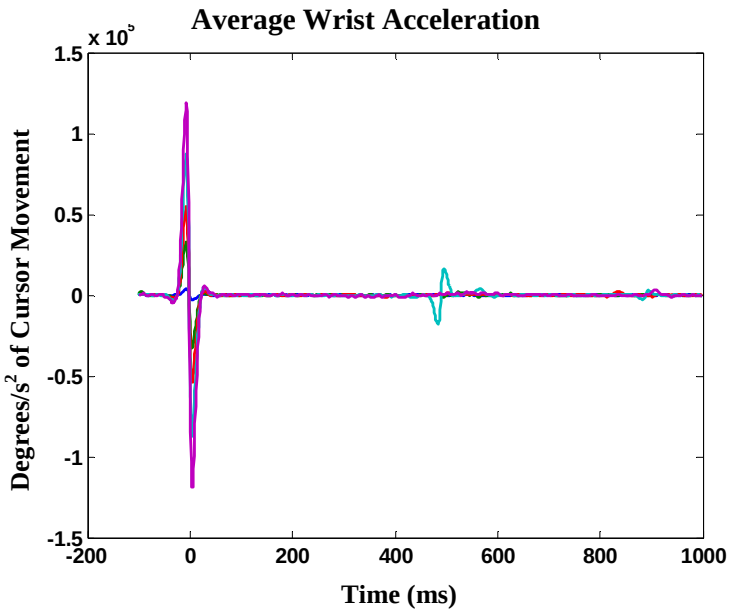

Subject NJ5013: Proprioceptive Condition

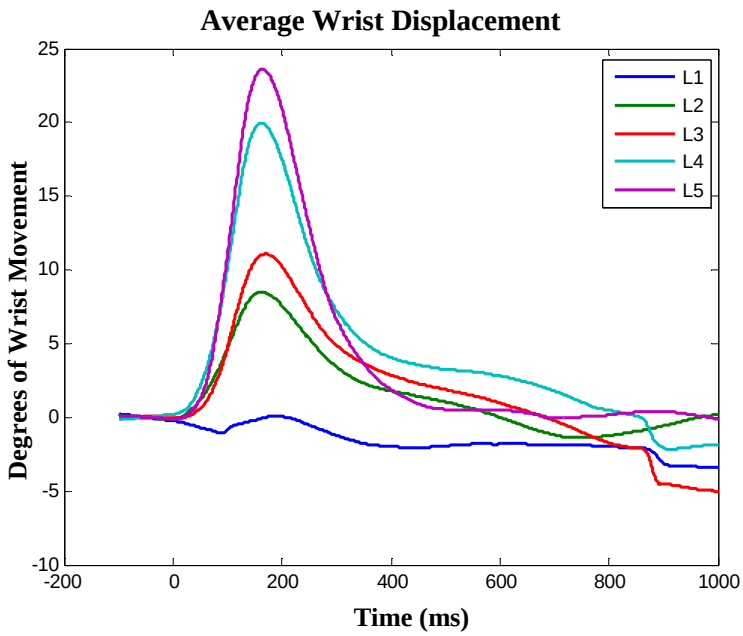

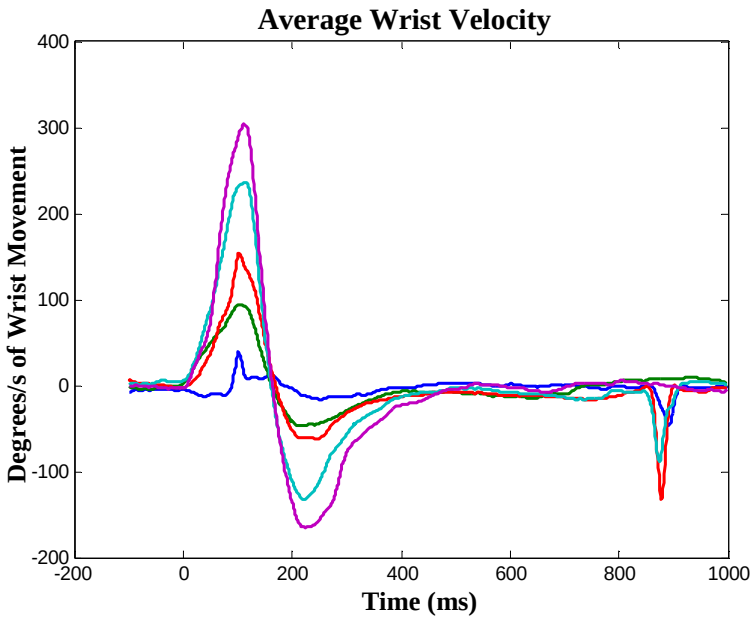

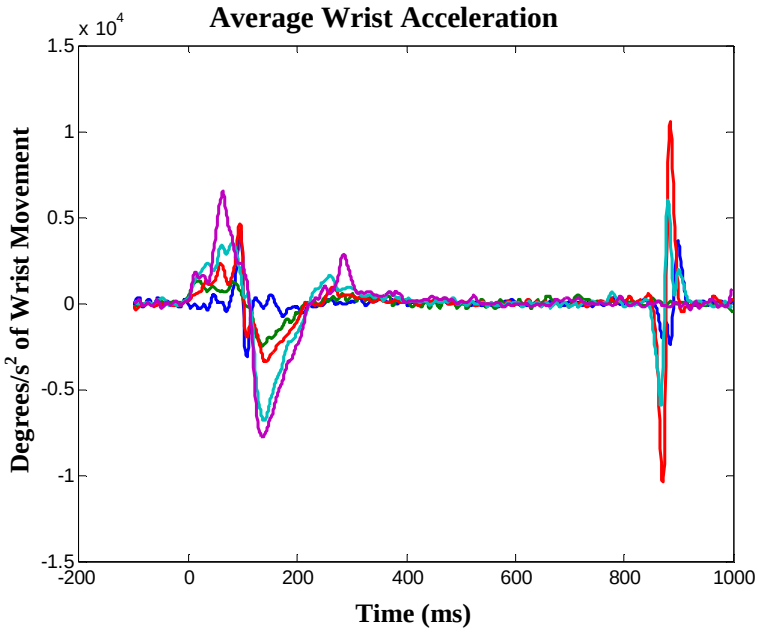

Subject NJ5013: Visual Condition

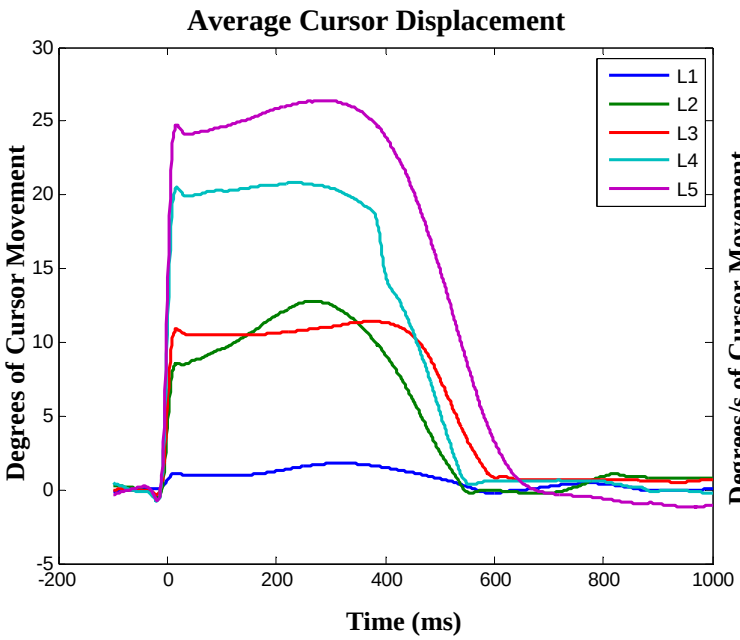

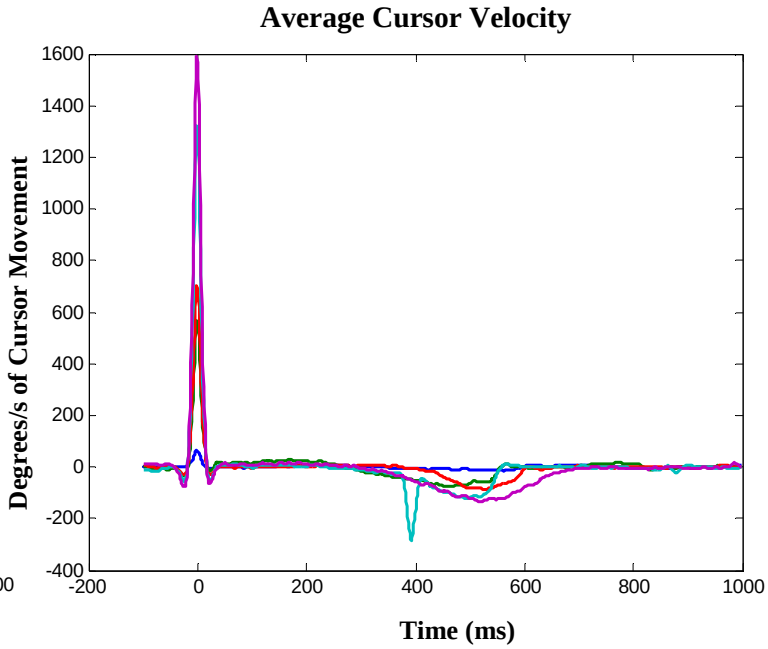

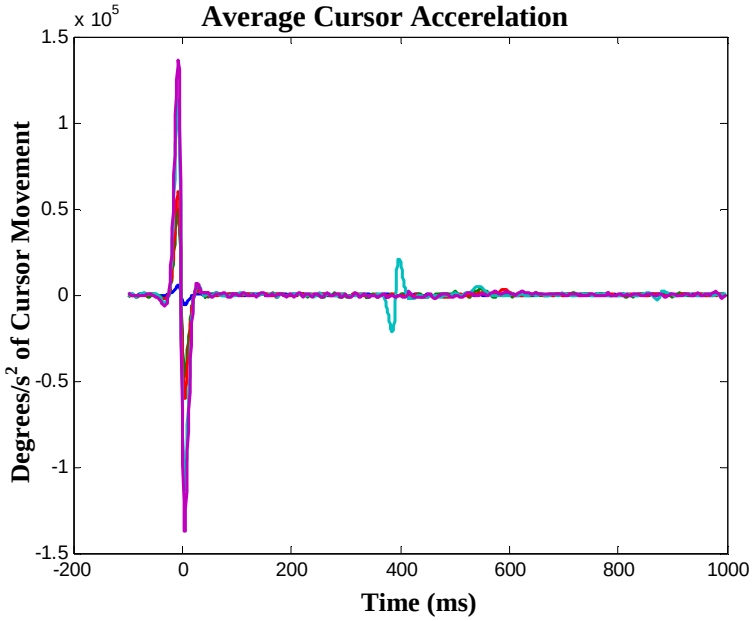

Subject NY2985: Proprioceptive Condition

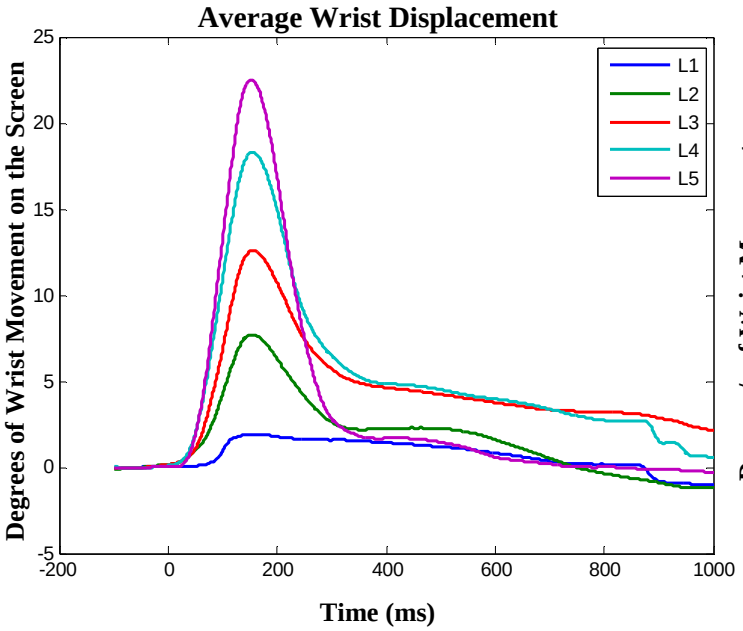

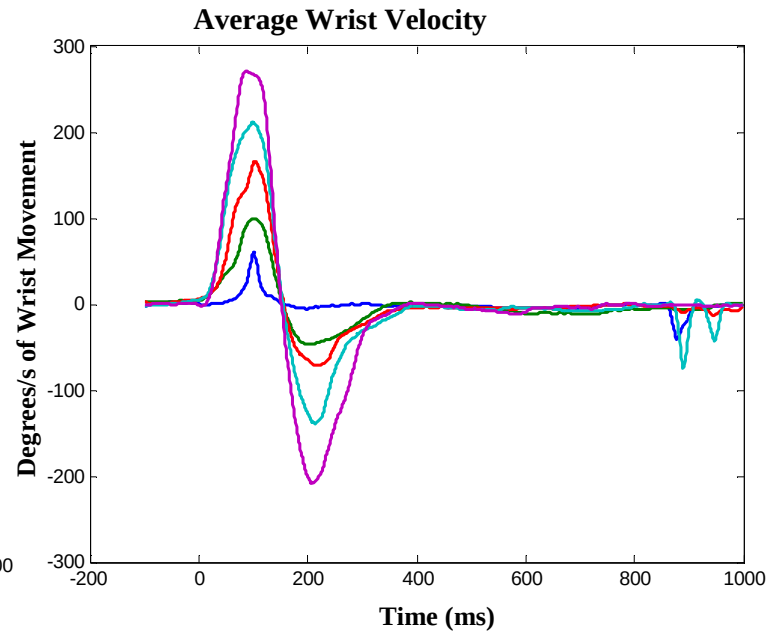

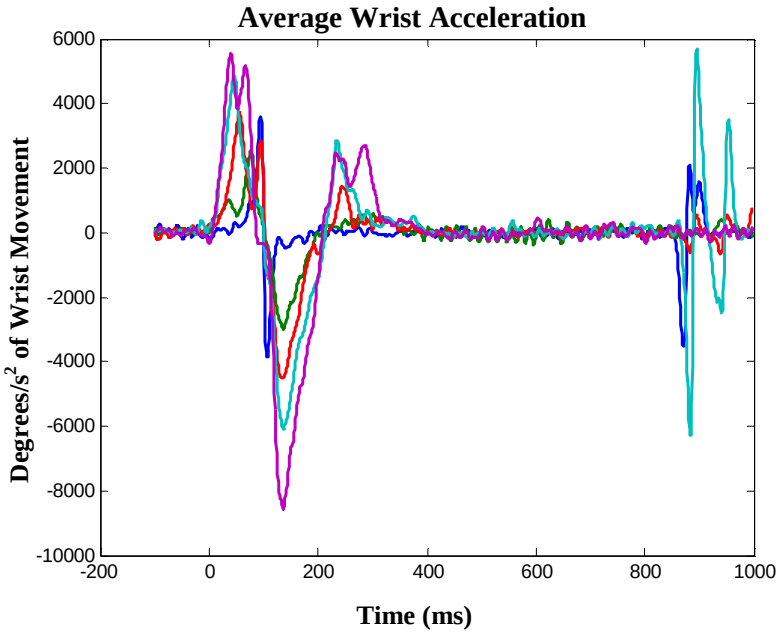

Subject NY2985: Visual Condition

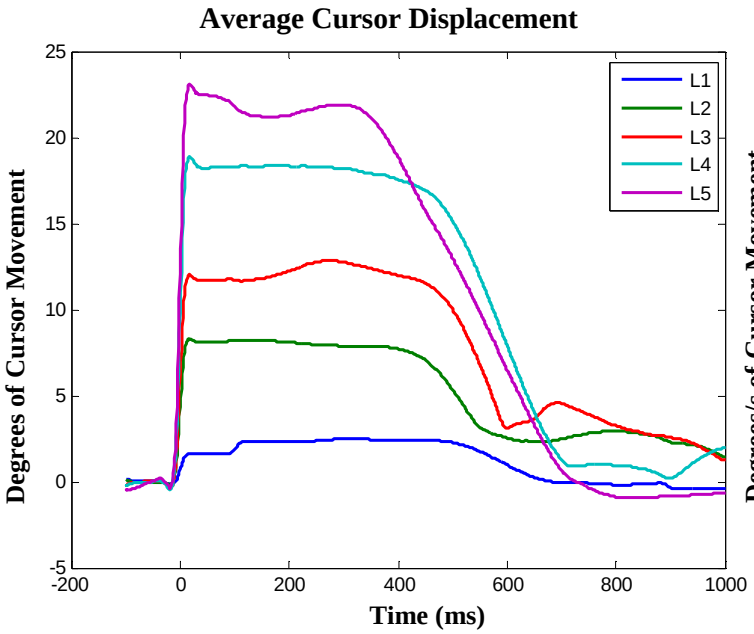

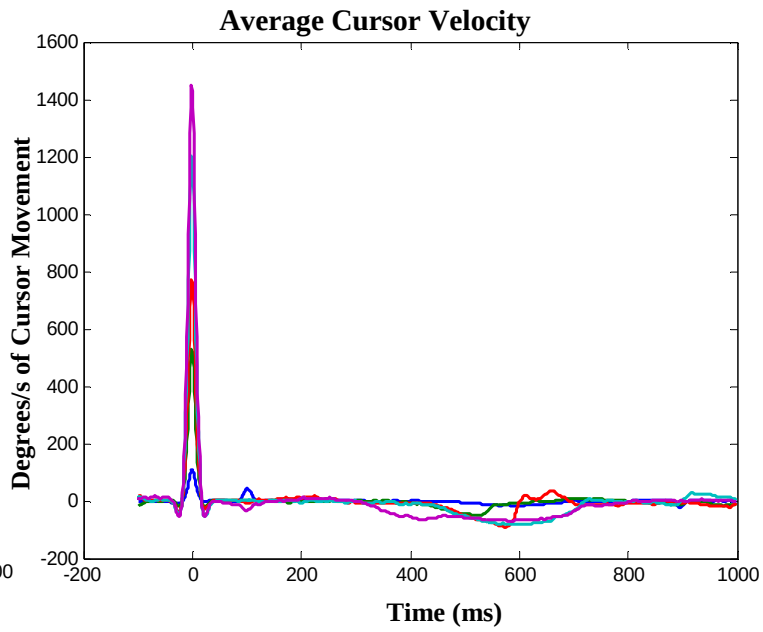

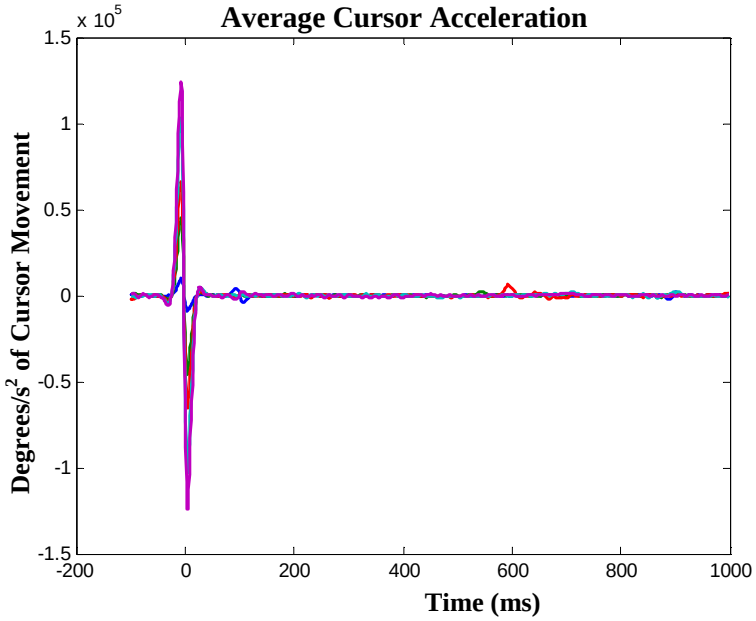

Subject PU7493: Proprioceptive Condition

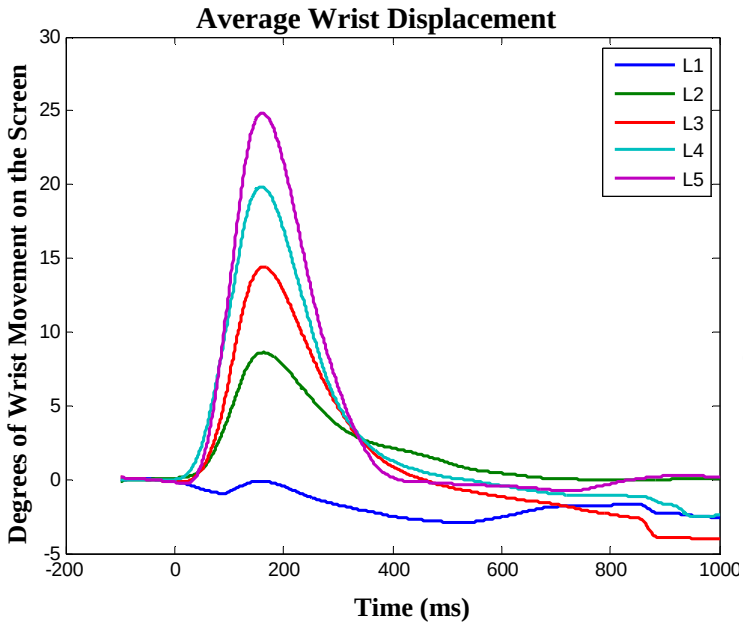

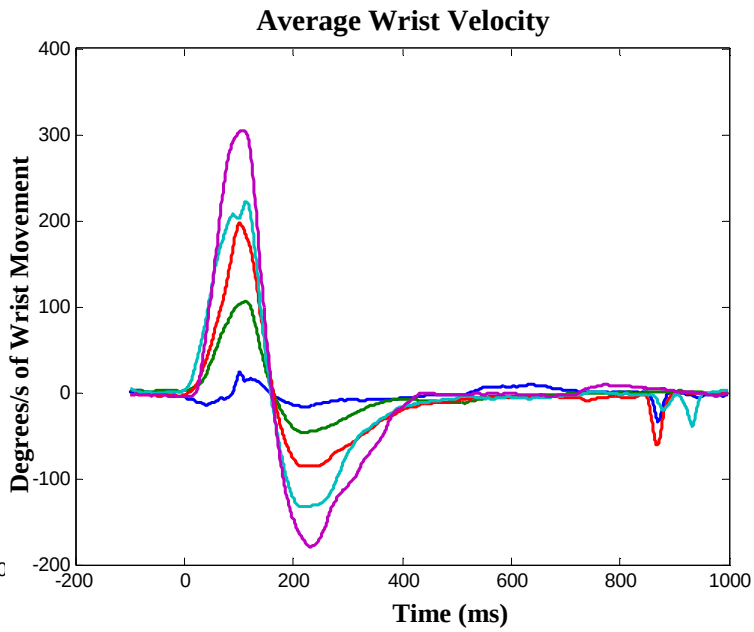

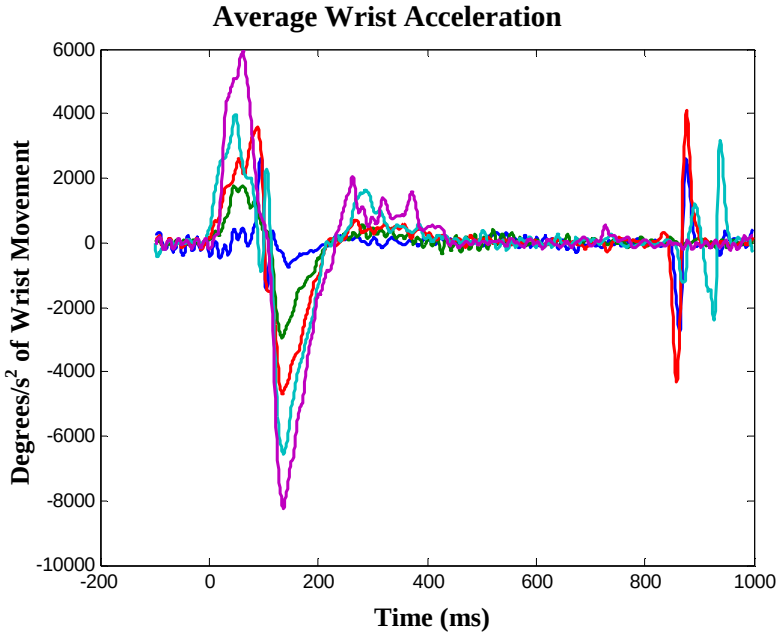

Subject PU7493: Visual Condition

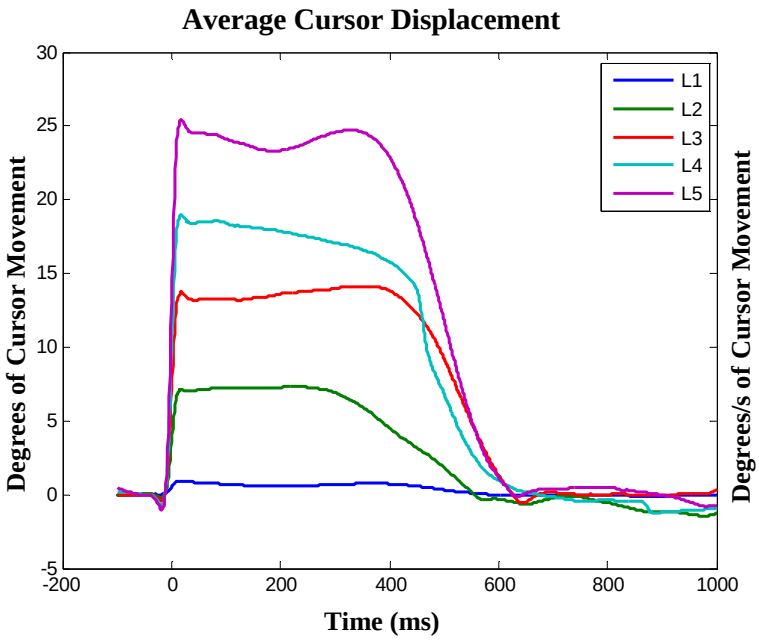

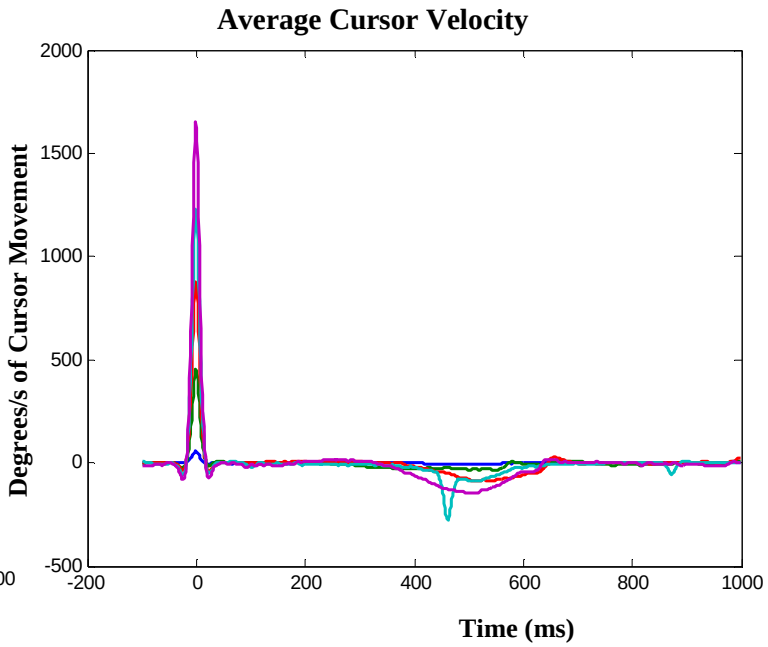

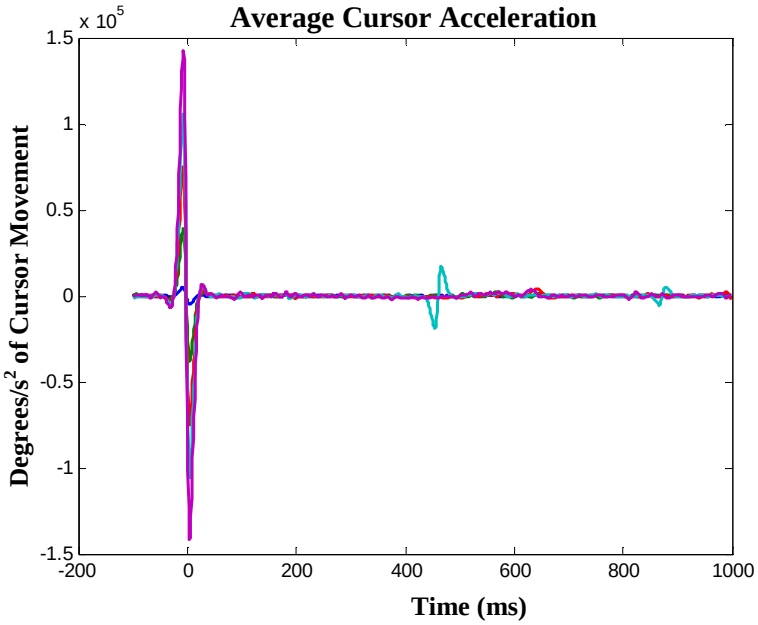

Subject RL3934: Proprioceptive Condition

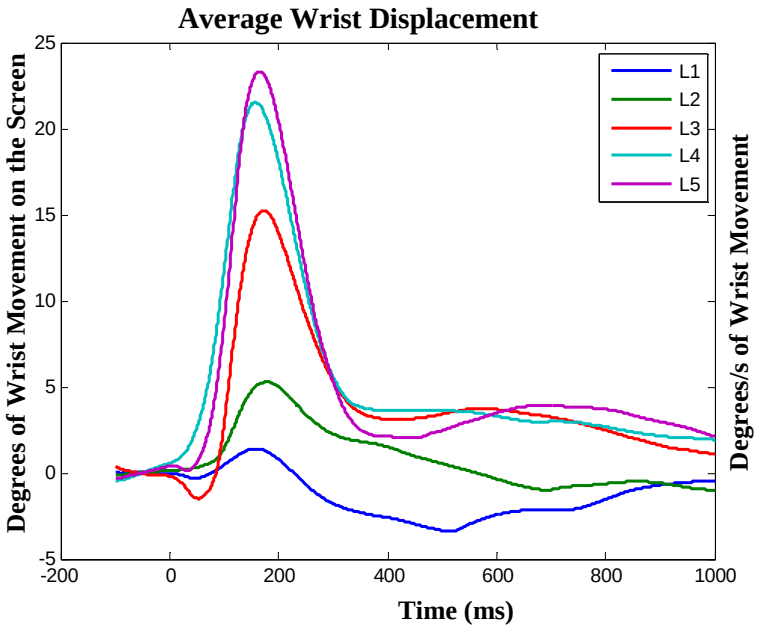

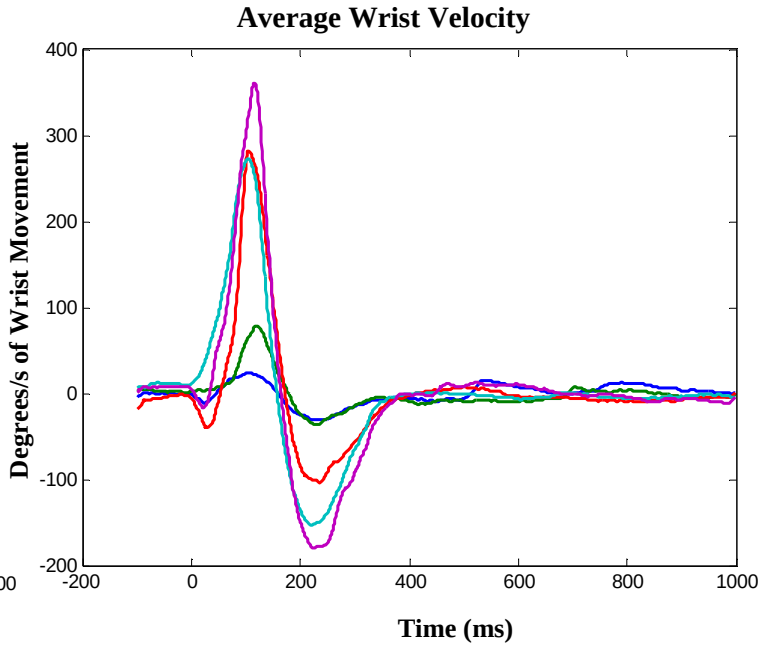

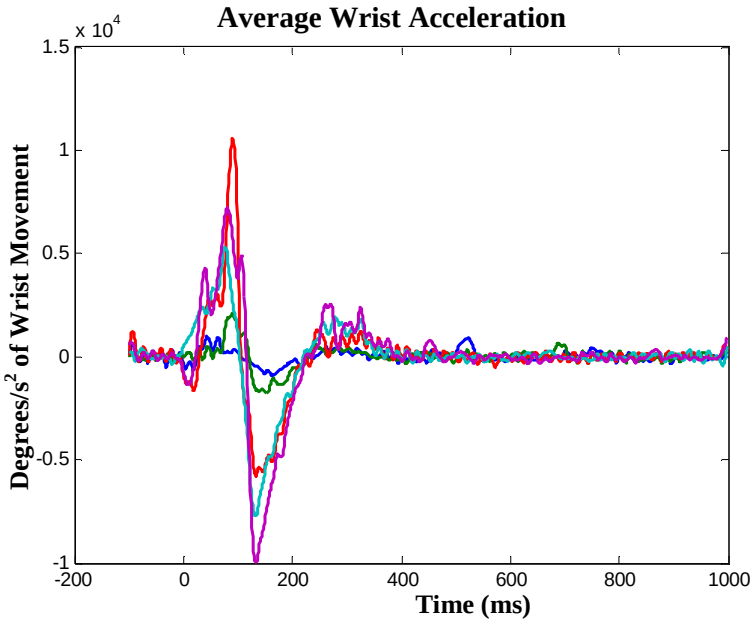

Subject RL3934: Visual Condition

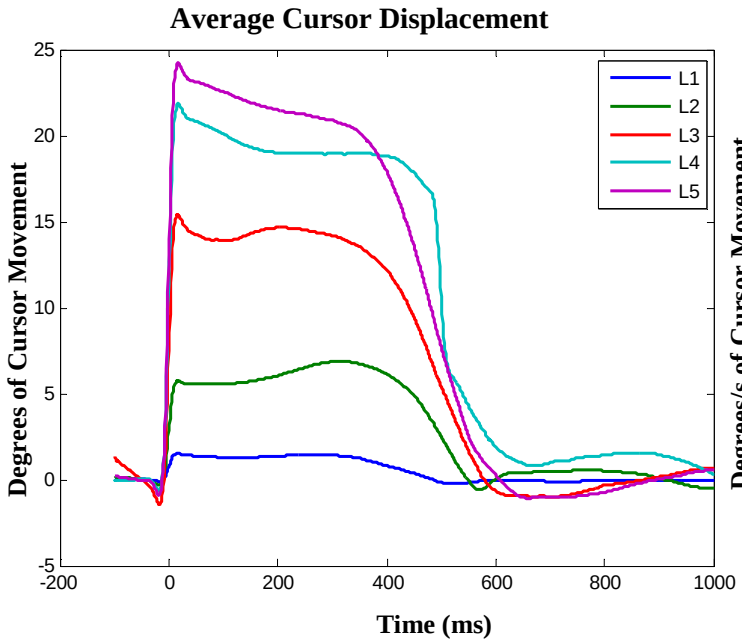

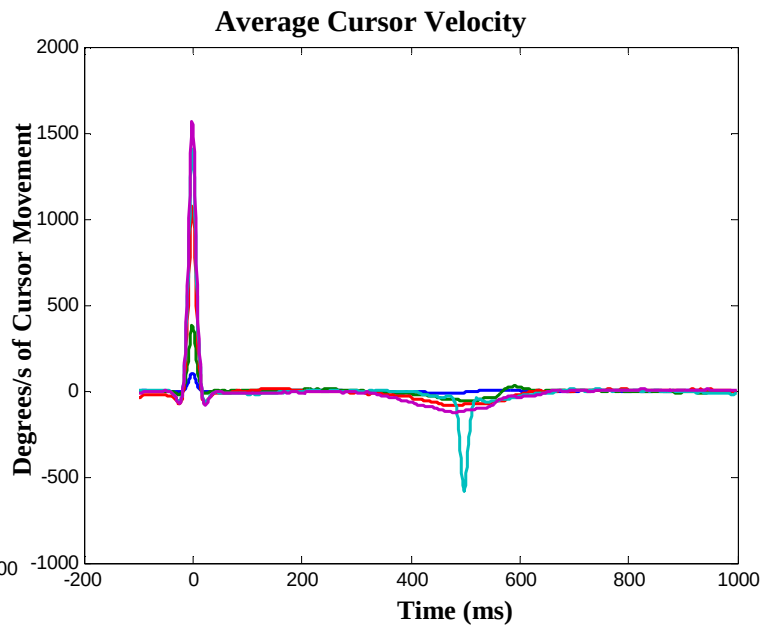

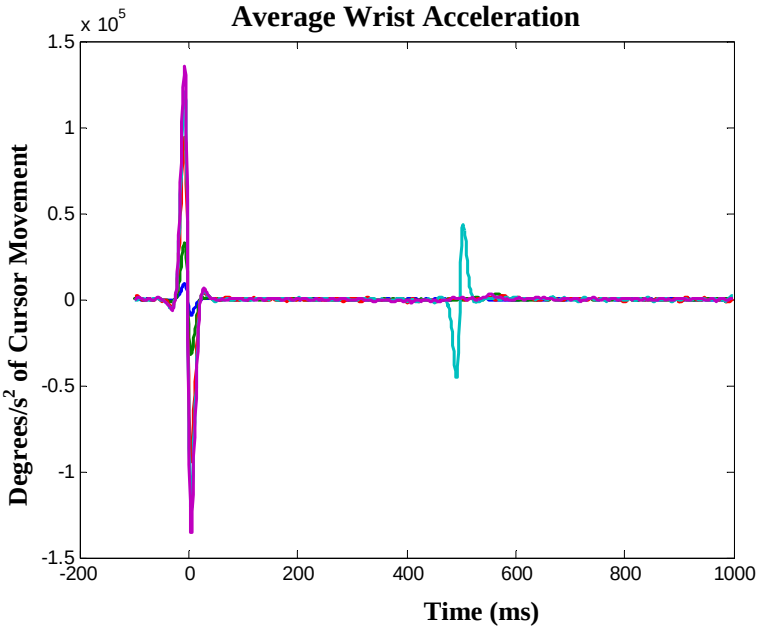

Appendix B: Averaged Evoked Response

The following plots show single-subject averaged EEG data at two specific EEG channels. Proprioceptive plots illustrate the neural response at Channel CZ and Visual plots at Channel CP1. The channels were selected based on their maximal neural response across subjects.

Subject AV7089

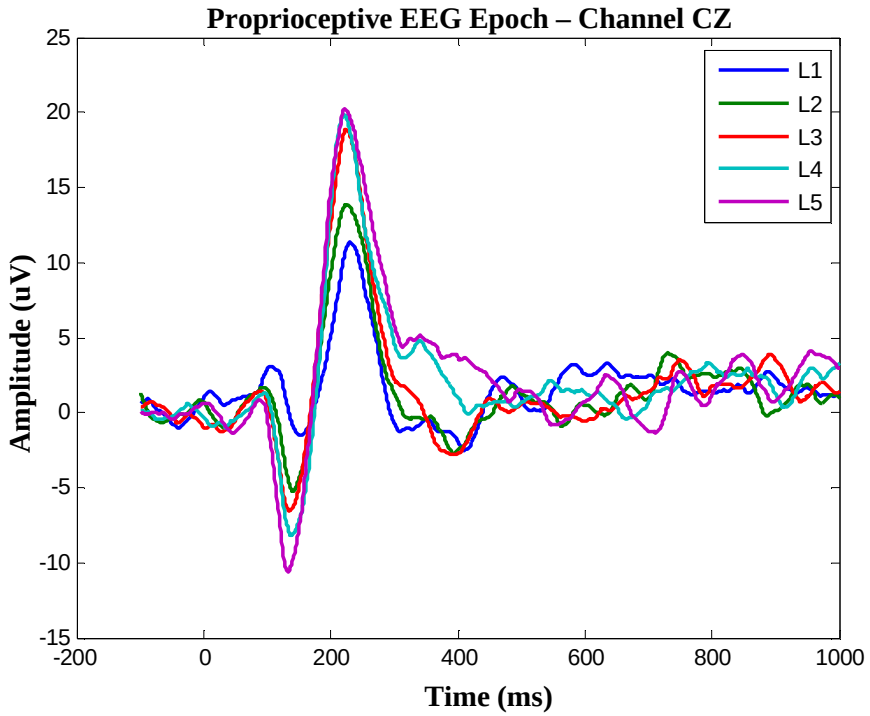

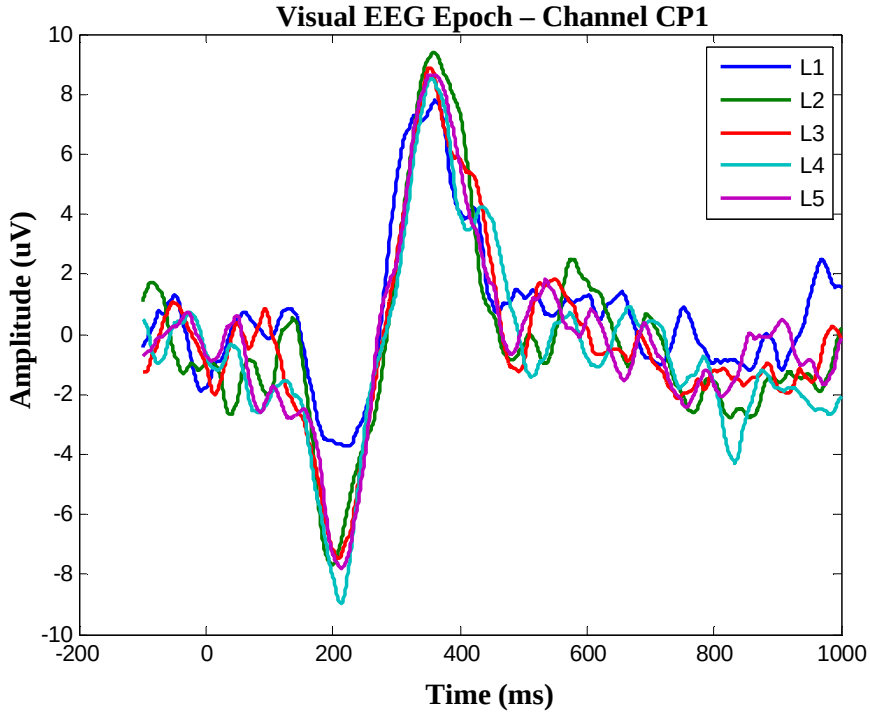

Subject CL2426

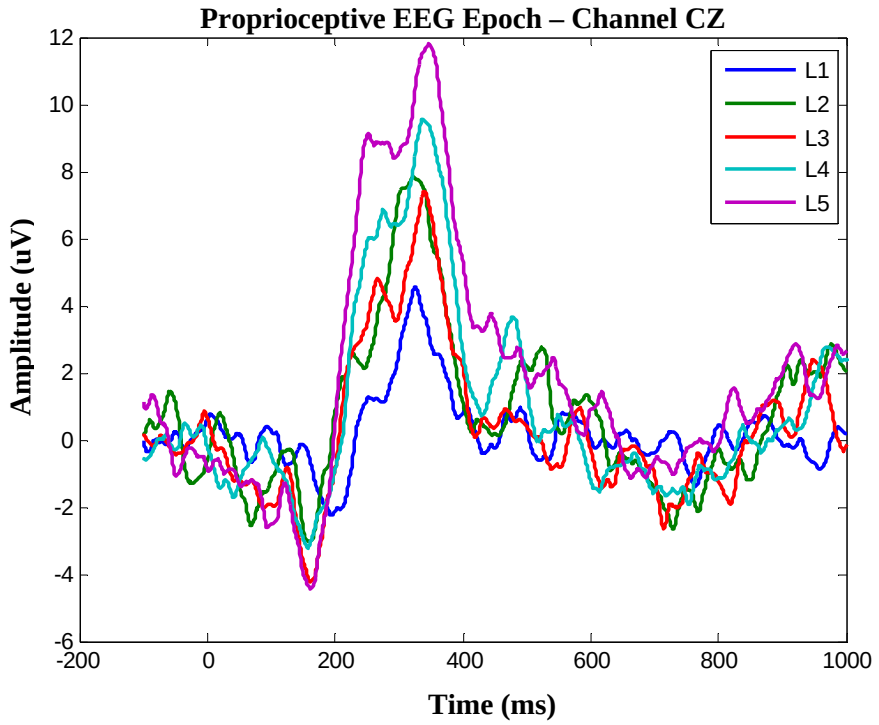

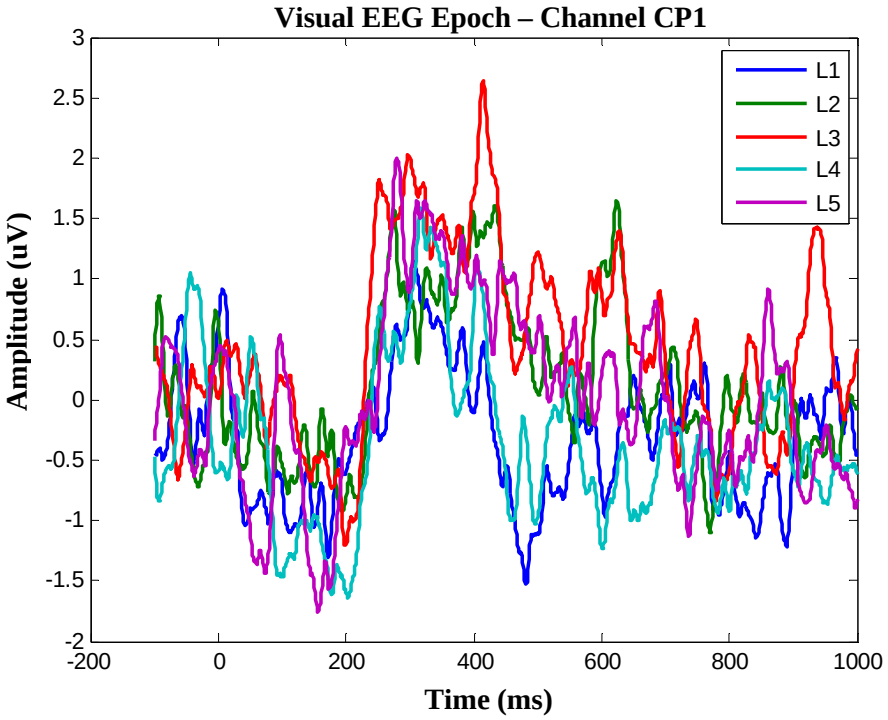

Subject MD9904

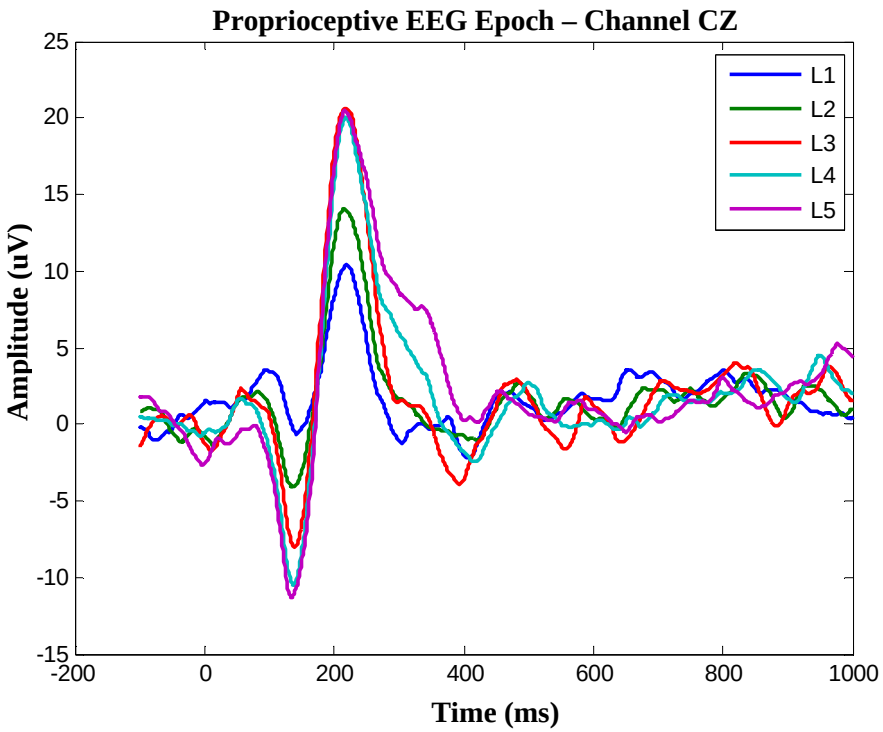

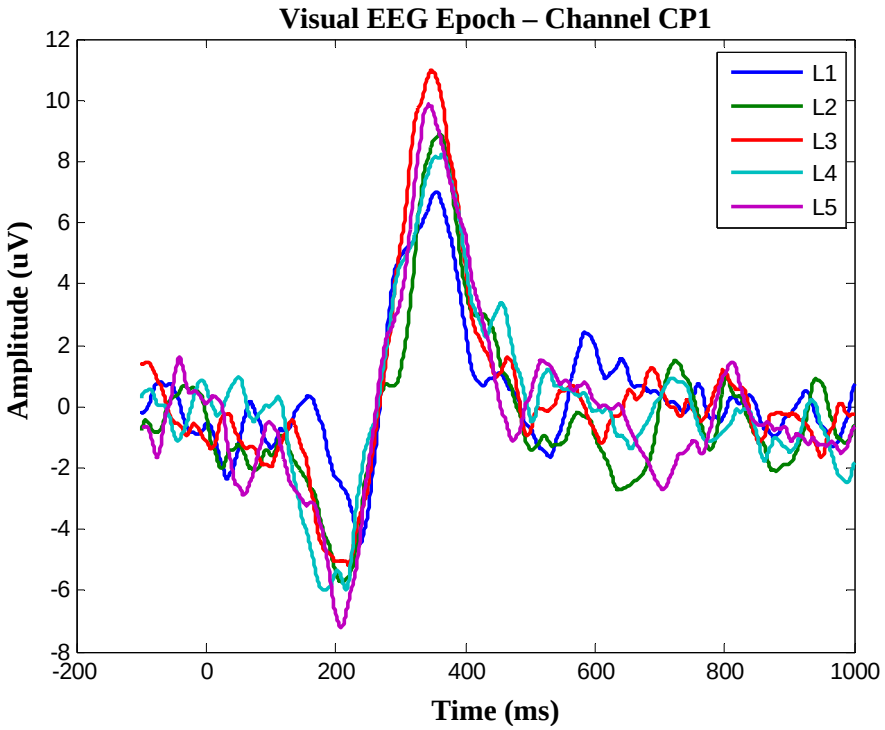

Subject NJ5013

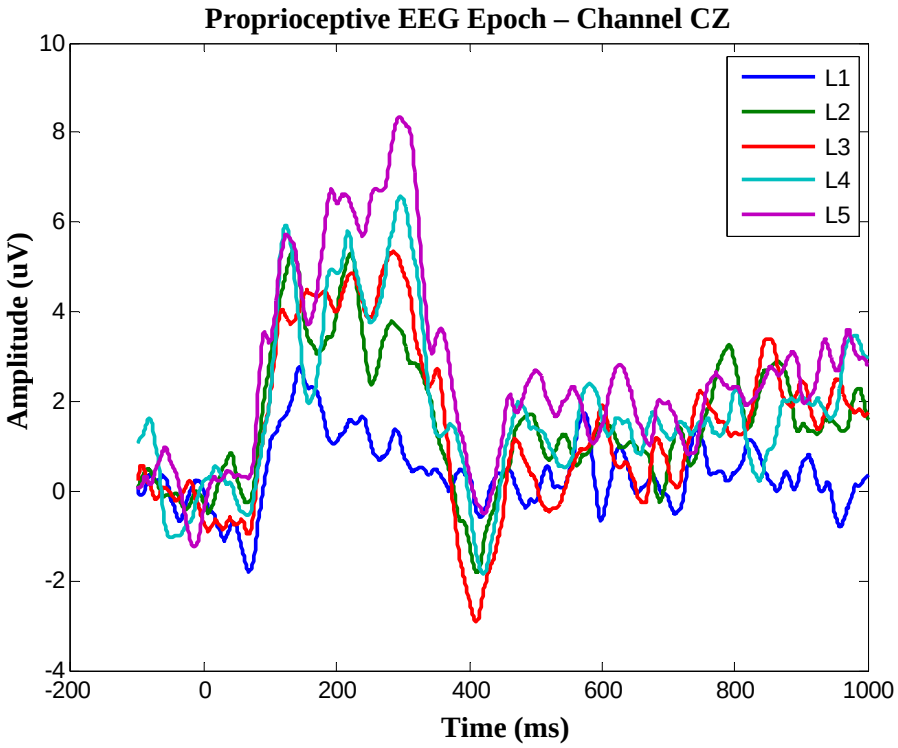

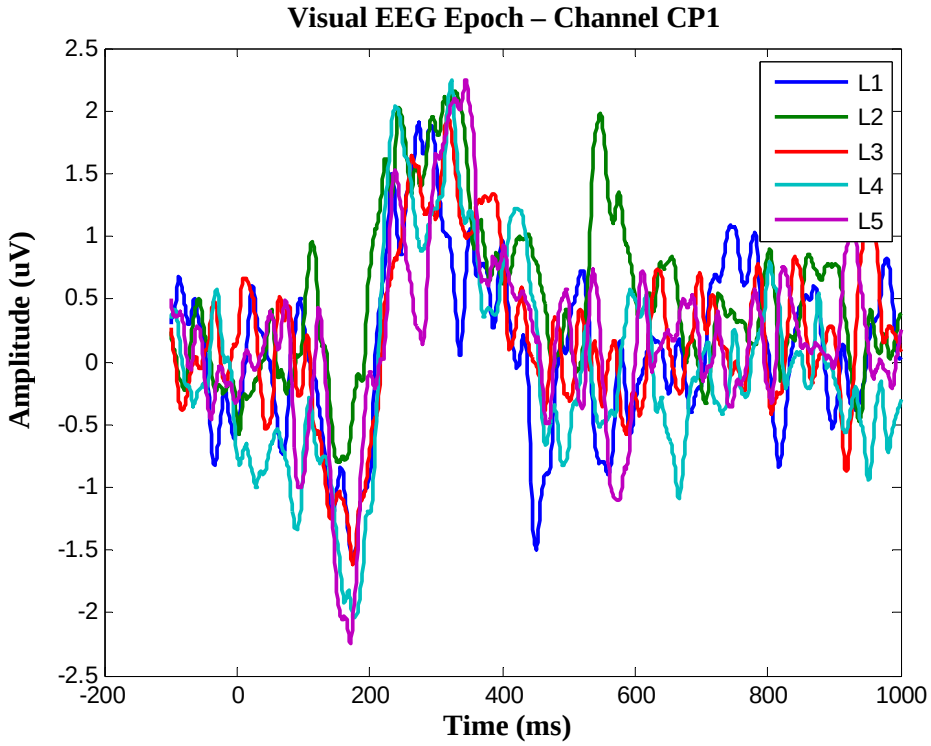

Subject NY2985

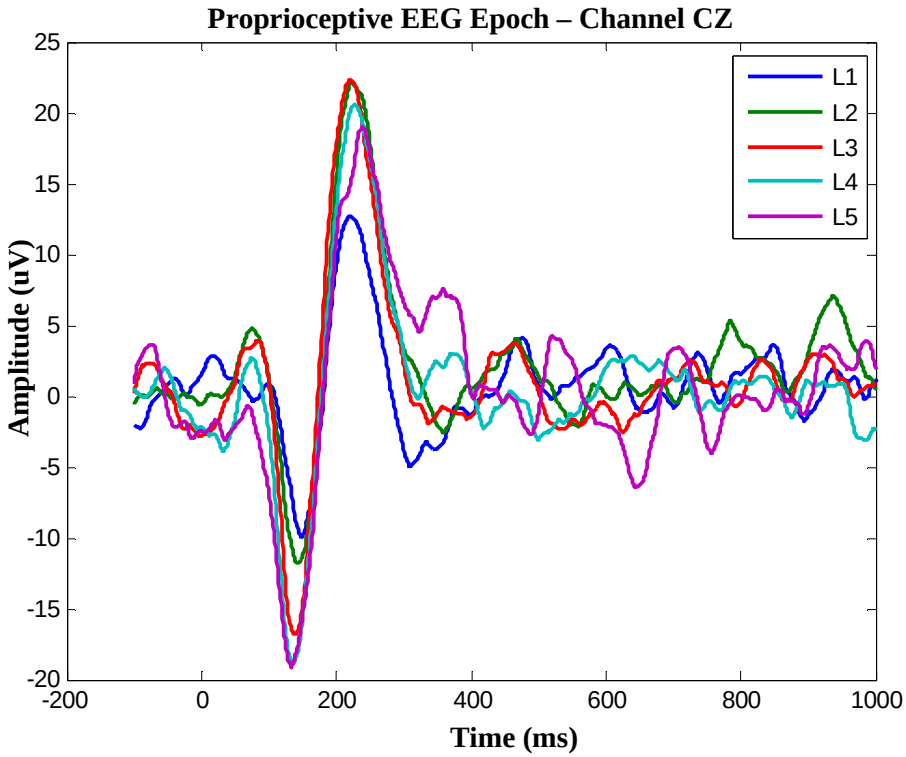

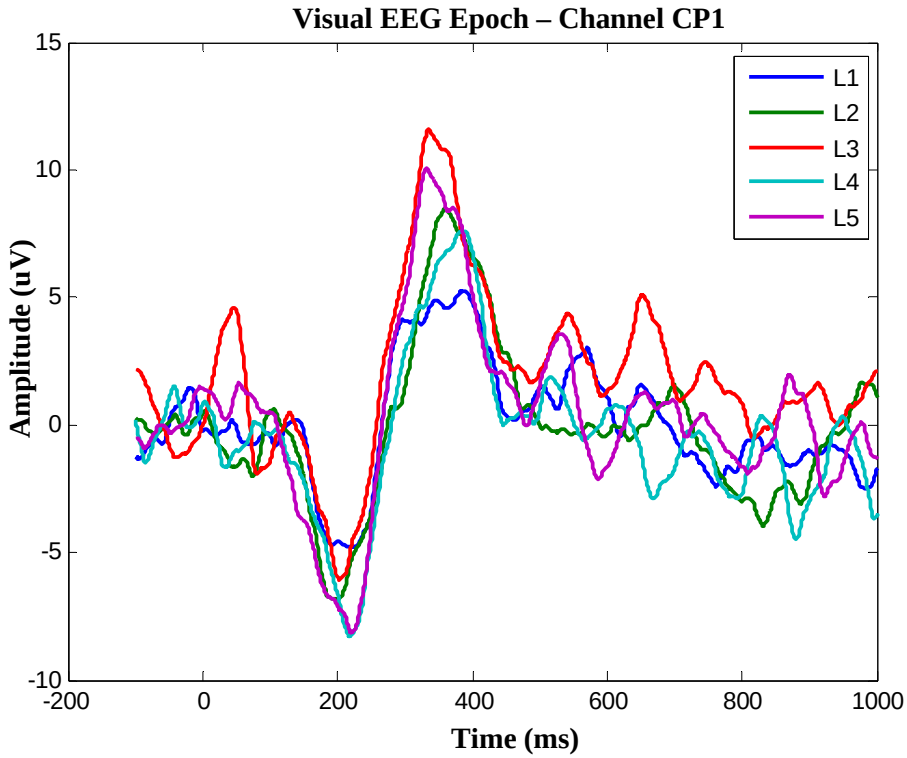

Subject PU7493

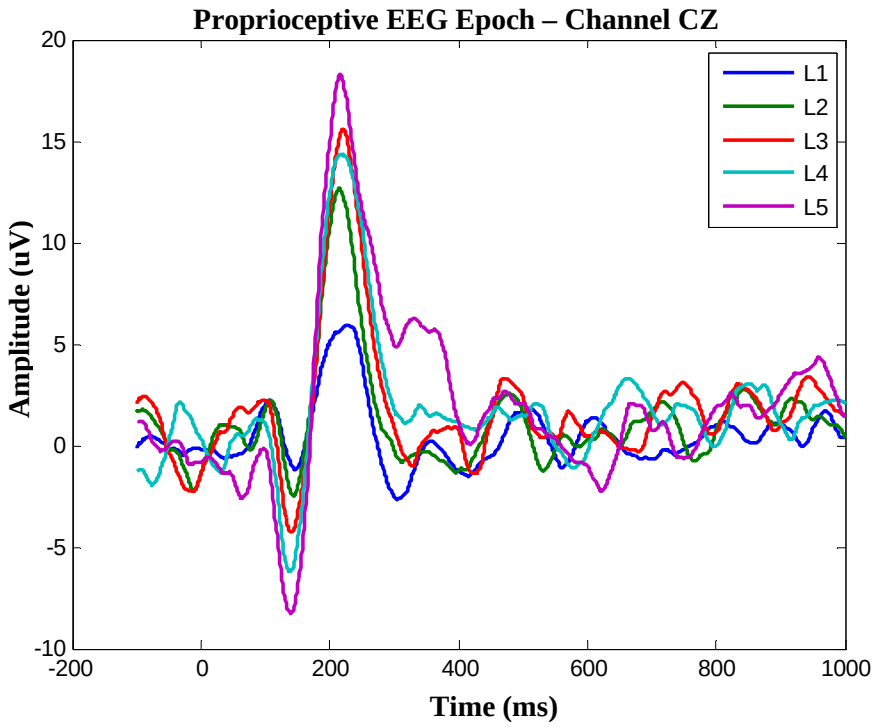

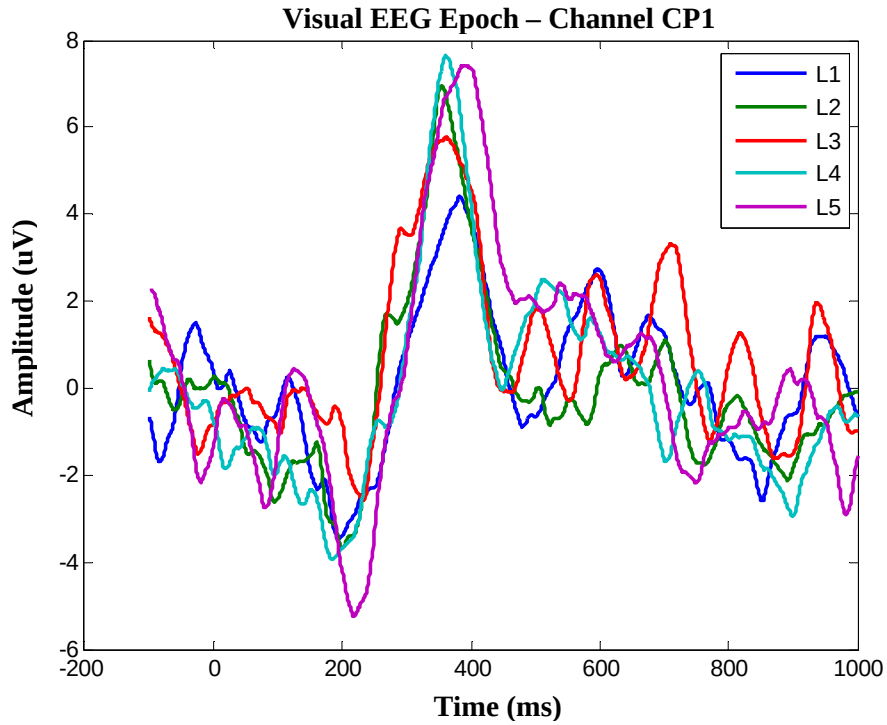

Subject RL3934

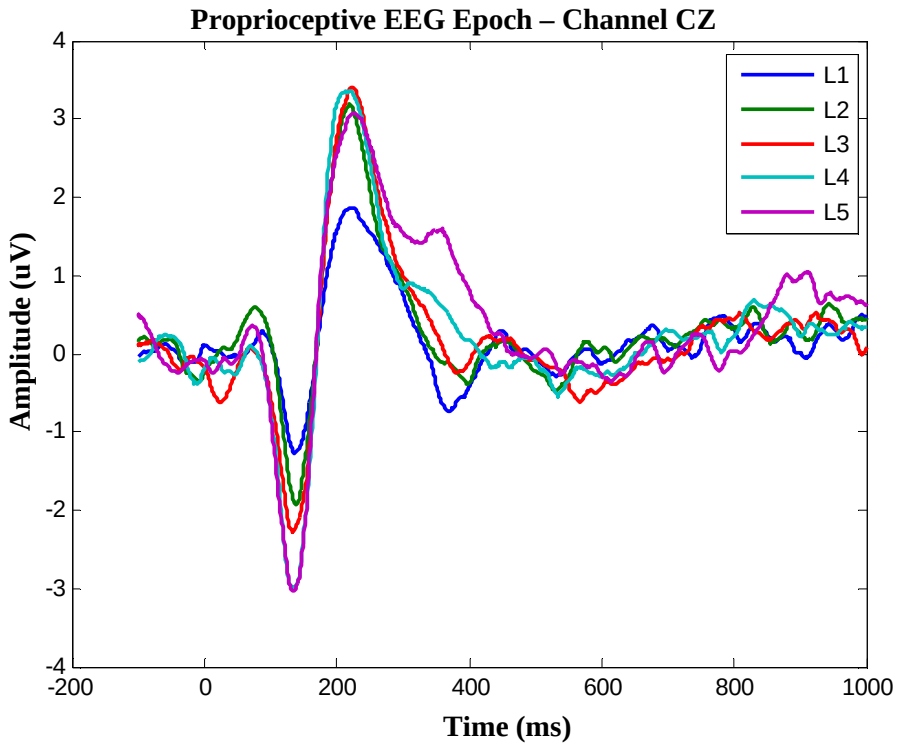

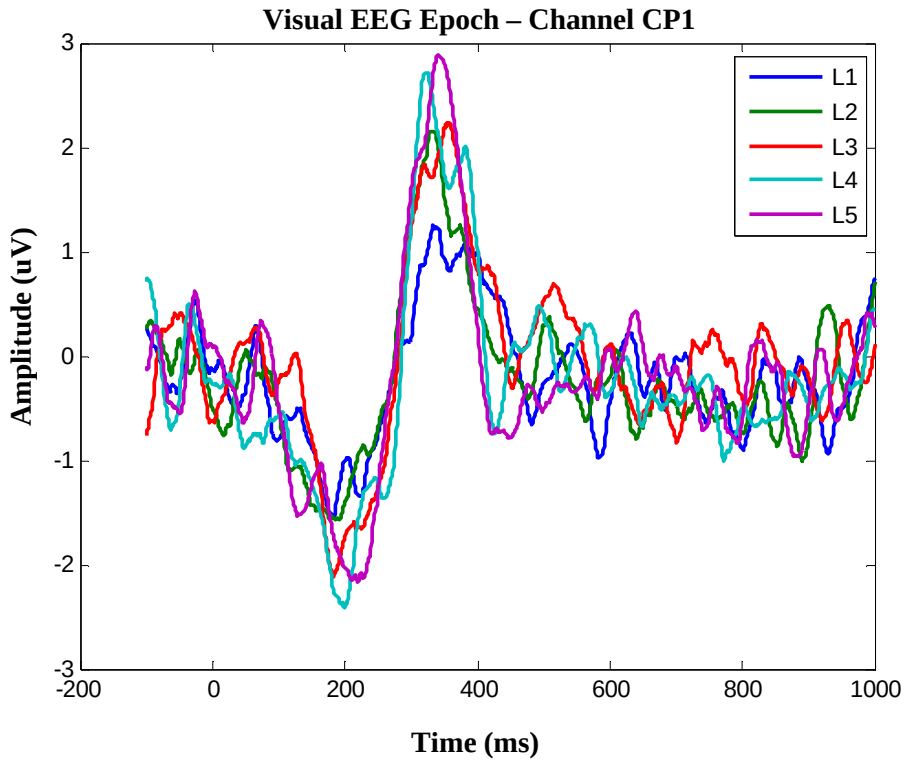

Appendix C: Current Source Density Profiles Across ROI's

The following plots display the entire time course of average cortical activity within a time window across ROI's on the left cortical surface for MD9904. Time windows were chosen centered around the N100 (i.e. 110-160 ms for Proprioceptive and 180-230 ms for Visual) unless no significant vertices were found in that time window. For ROI's that did not contain significant vertices in the specified time window, the next closest time window with error-related vertices was chosen.

Frontal Areas

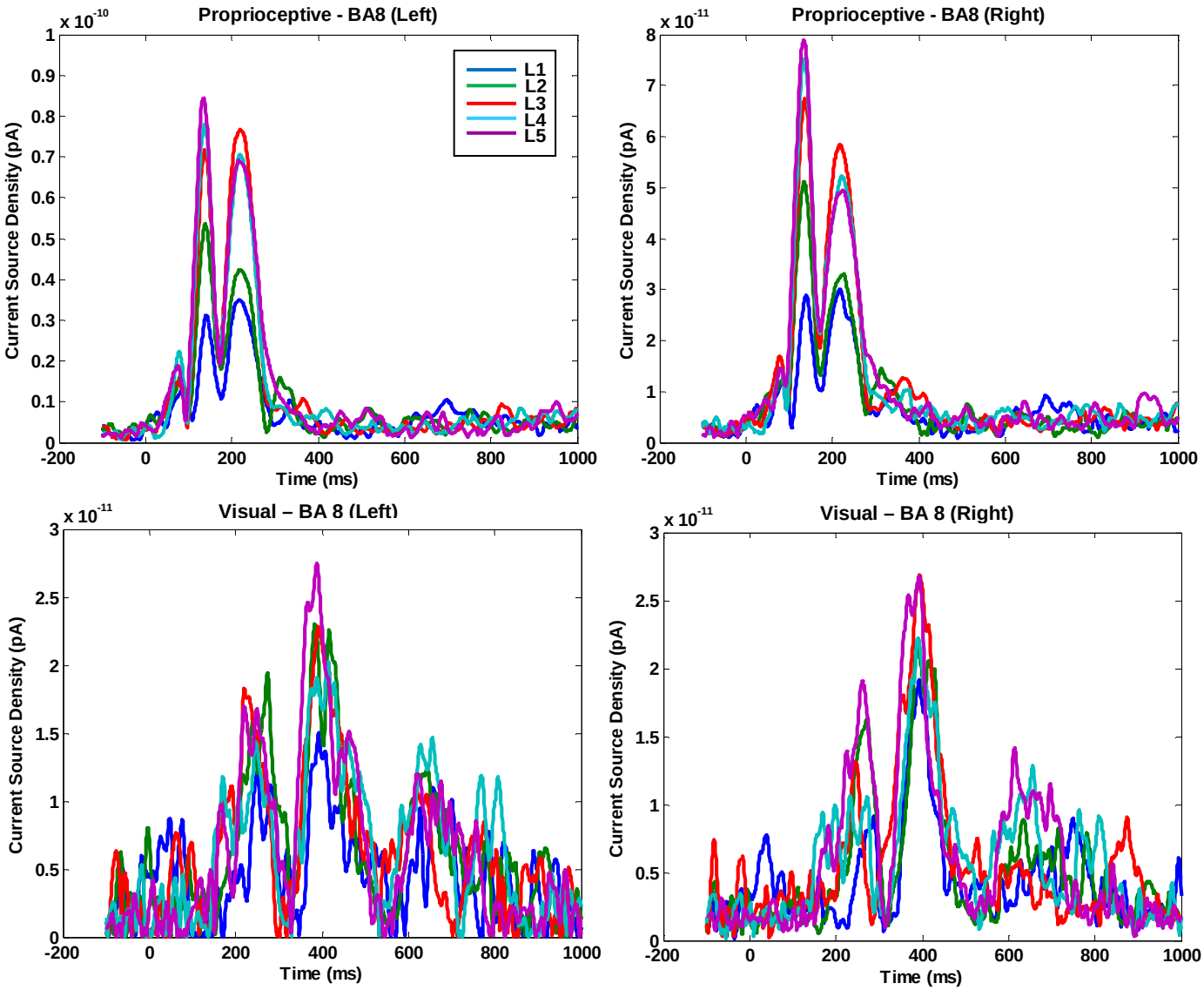

Due to a lack of error-related vertices in the 180-230 time bin, the next closest time window was chosen for BA 8 (Left) – Visual at 320-370 ms.

Unimodal Sensory Areas

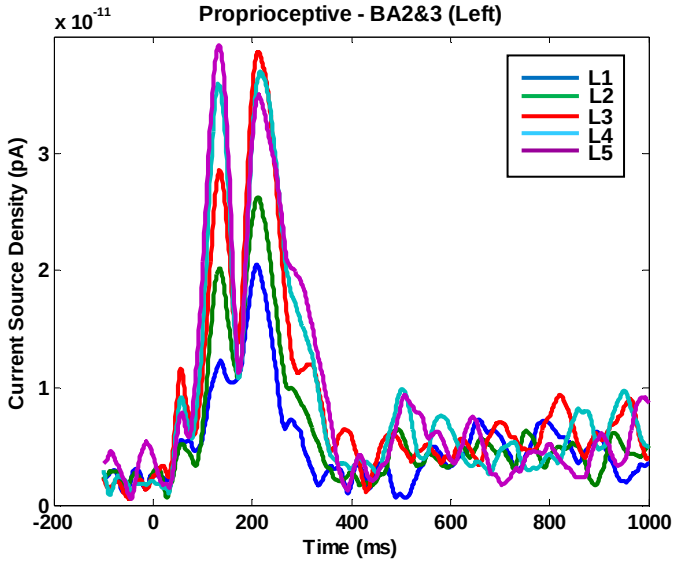

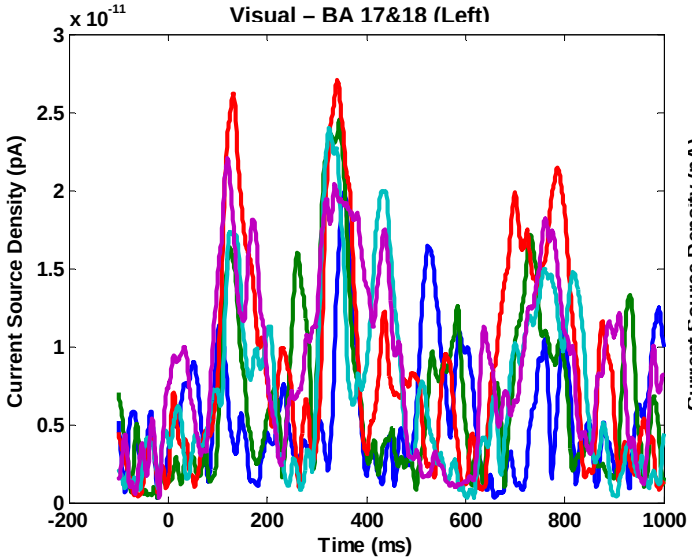

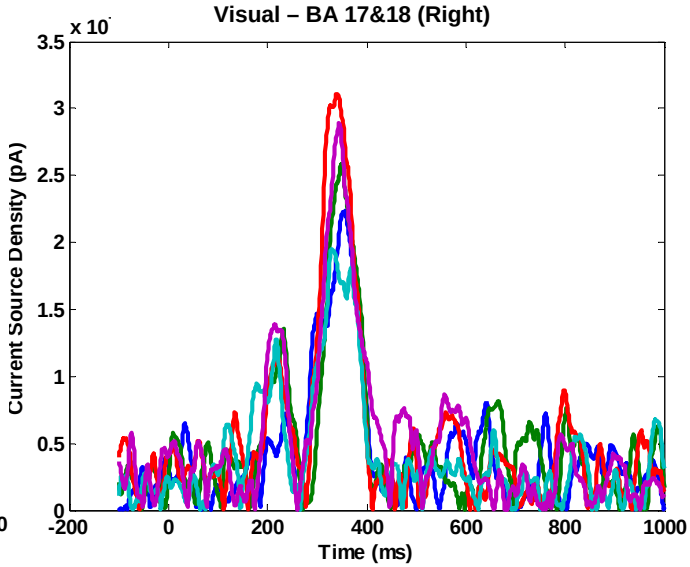

Due to a lack of error-related vertices in the N100 time window (180-230 ms), the next closest time window was chosen for BA 17&18 (Left) at 170-220 ms.

Motor Areas

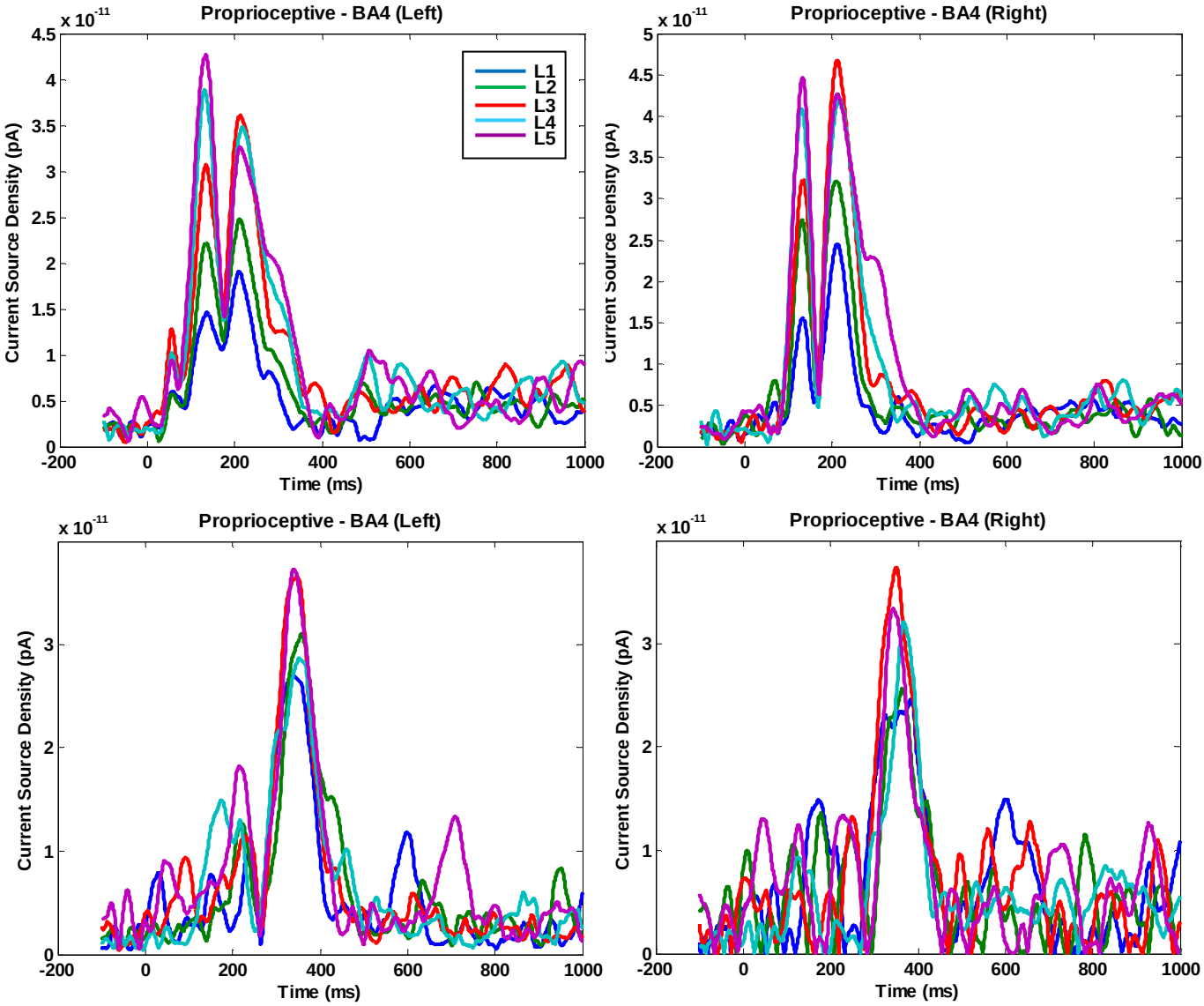
Proprioceptive - BA4 (Left)
Proprioceptive - BA4 (Right)
Proprioceptive - BA4 (Left)
Proprioceptive - BA4 (Right)
x 10^-11
Current Source Density (pA)
Time (ms)
L1
L2
L3
L4
L5

Premotor Areas

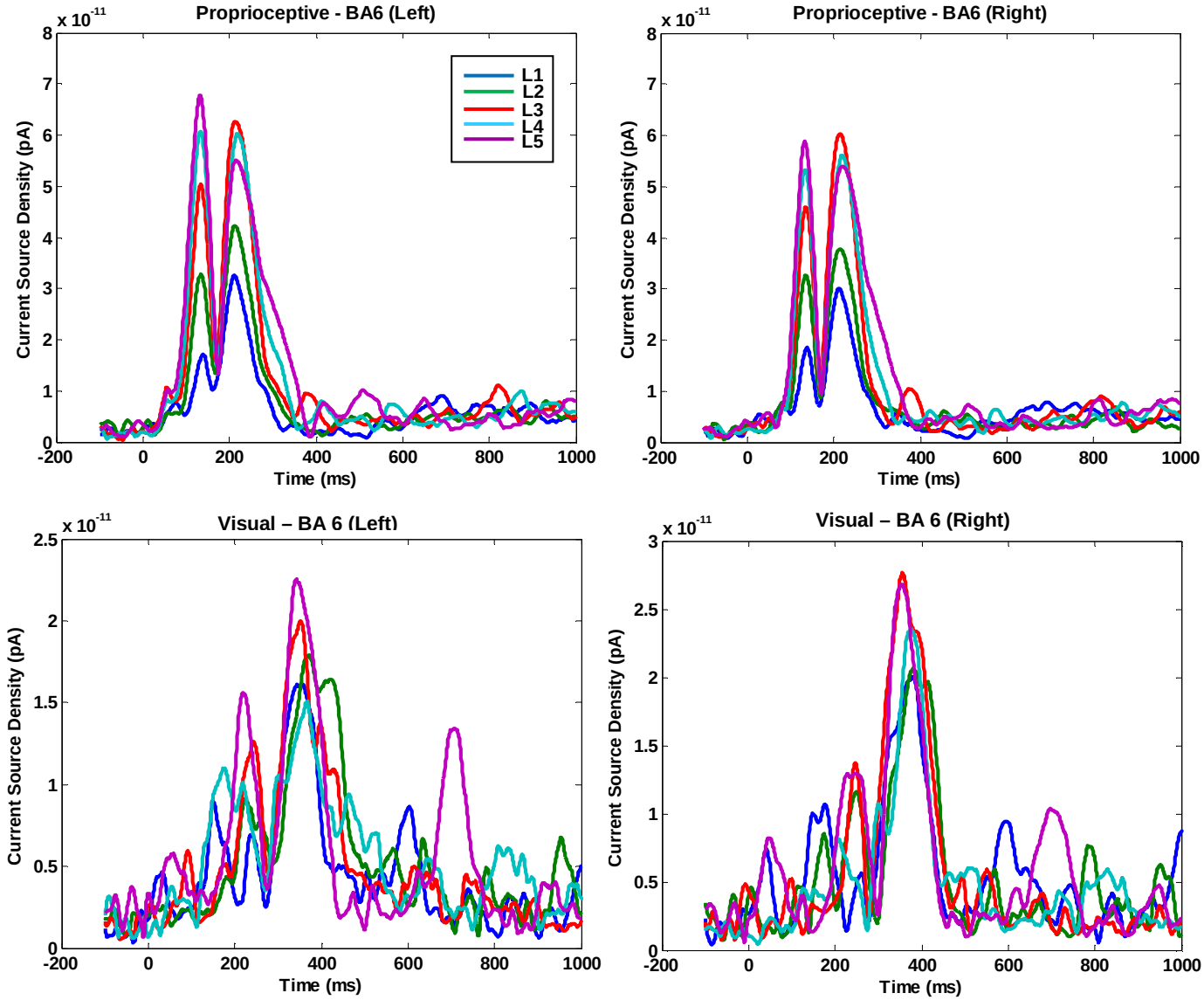

Parietal Areas

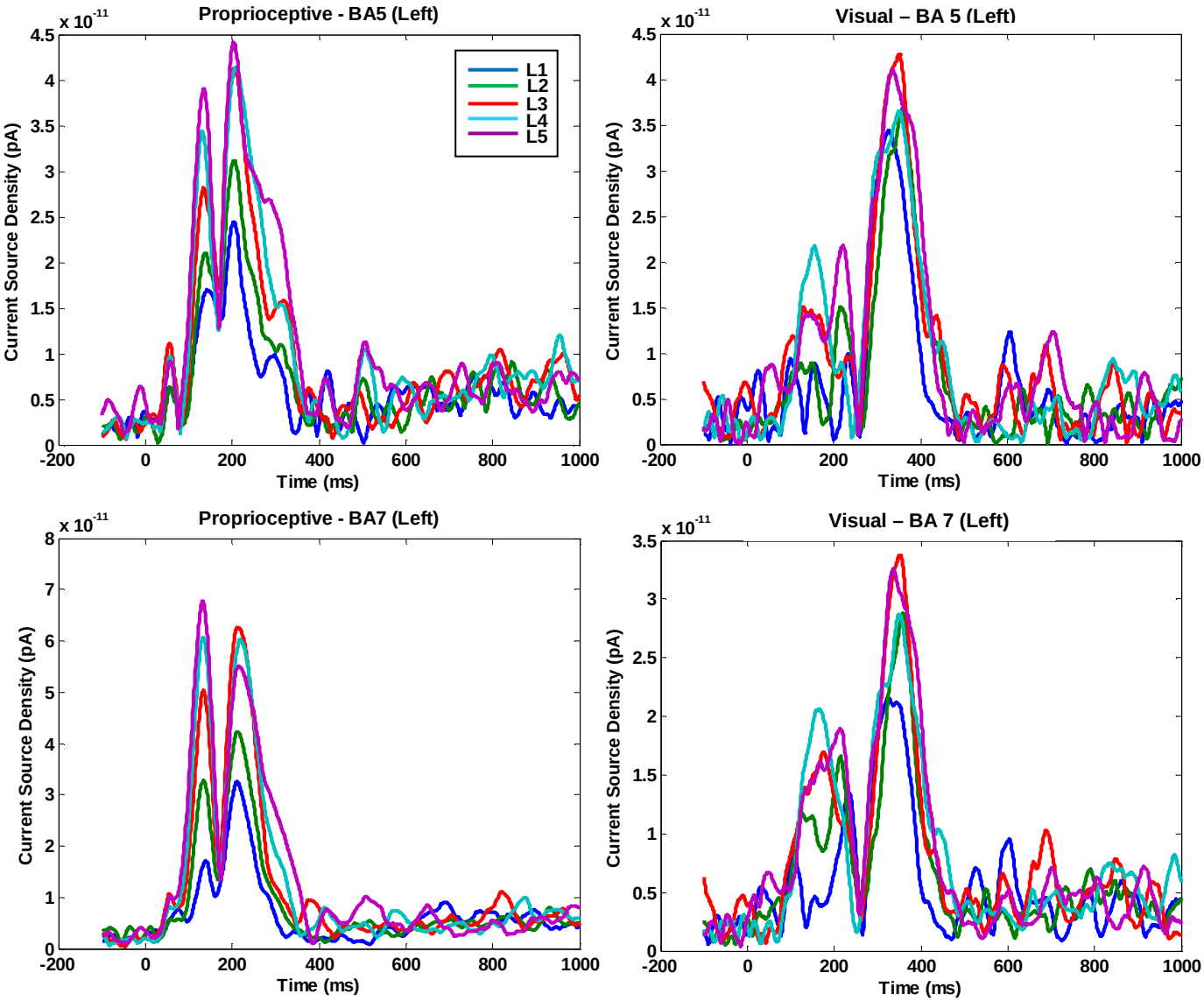

Parietal Areas

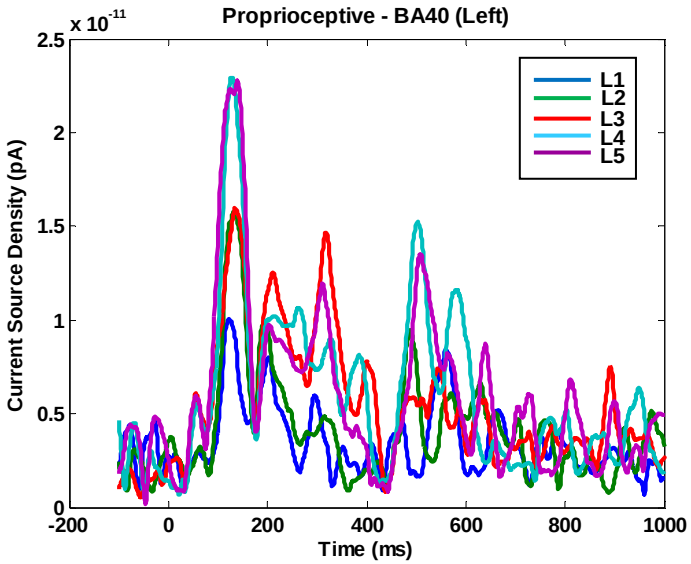

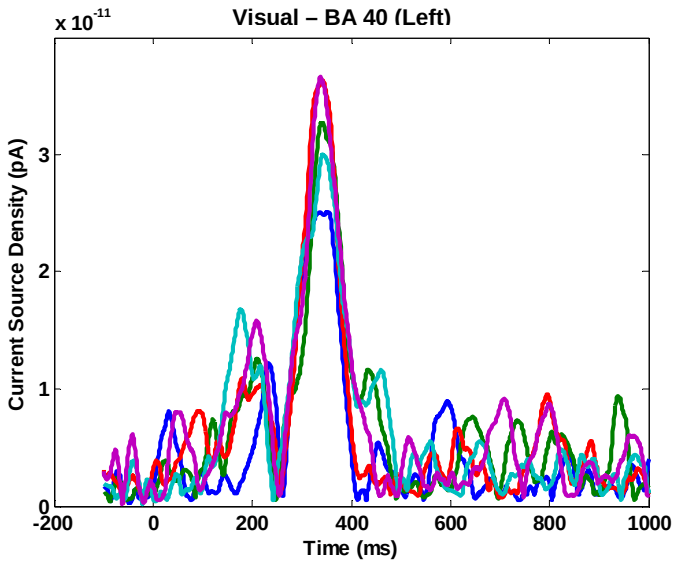

Appendix D: Functional Activation of ROI's

The following plots display the time course of functional activation (i.e. the number of vertices significantly correlated with displacement error in each time window across ROI's). Significantly activated vertices were normalized to the total number of activated vertices in each time window (thus each ROI peaked at 1).

Subject AV7089

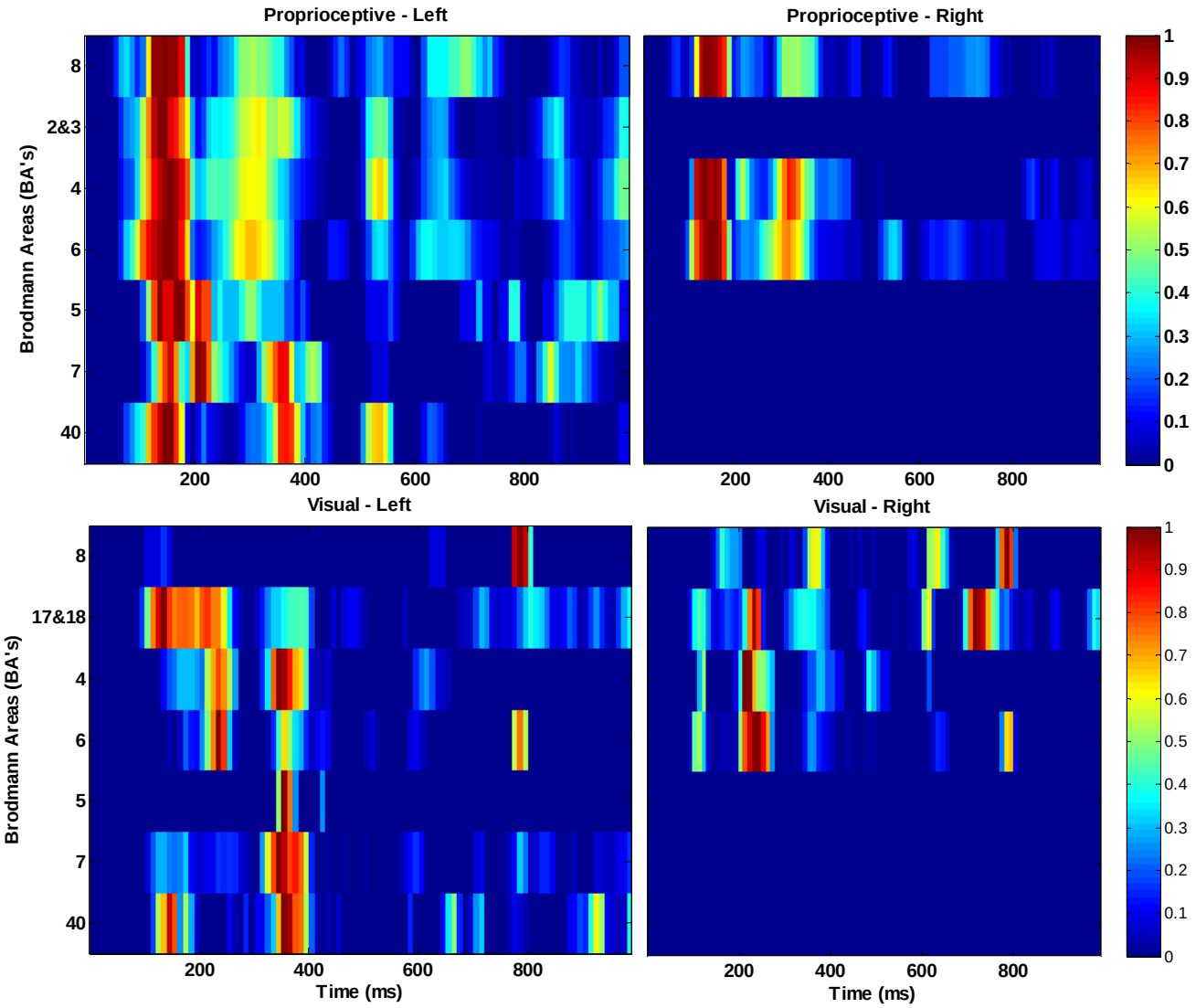

Subject CL2426

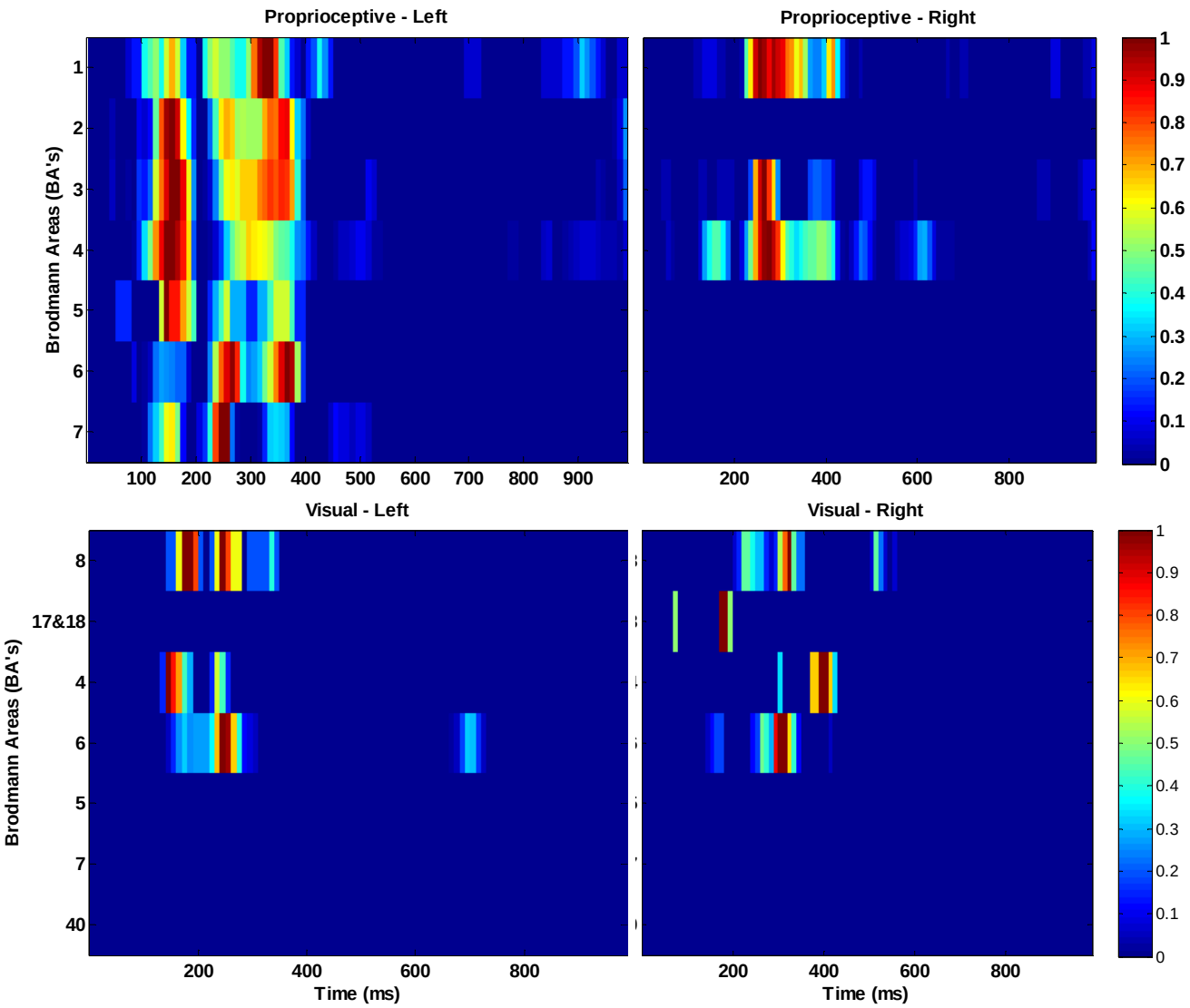

Note: Visual ROI's BA's 17&18 (left), 5, 7, and 40 (left) did not achieve statistical significance in error-related activity and thus were not used in results showing subject averages.

Subject MD9904

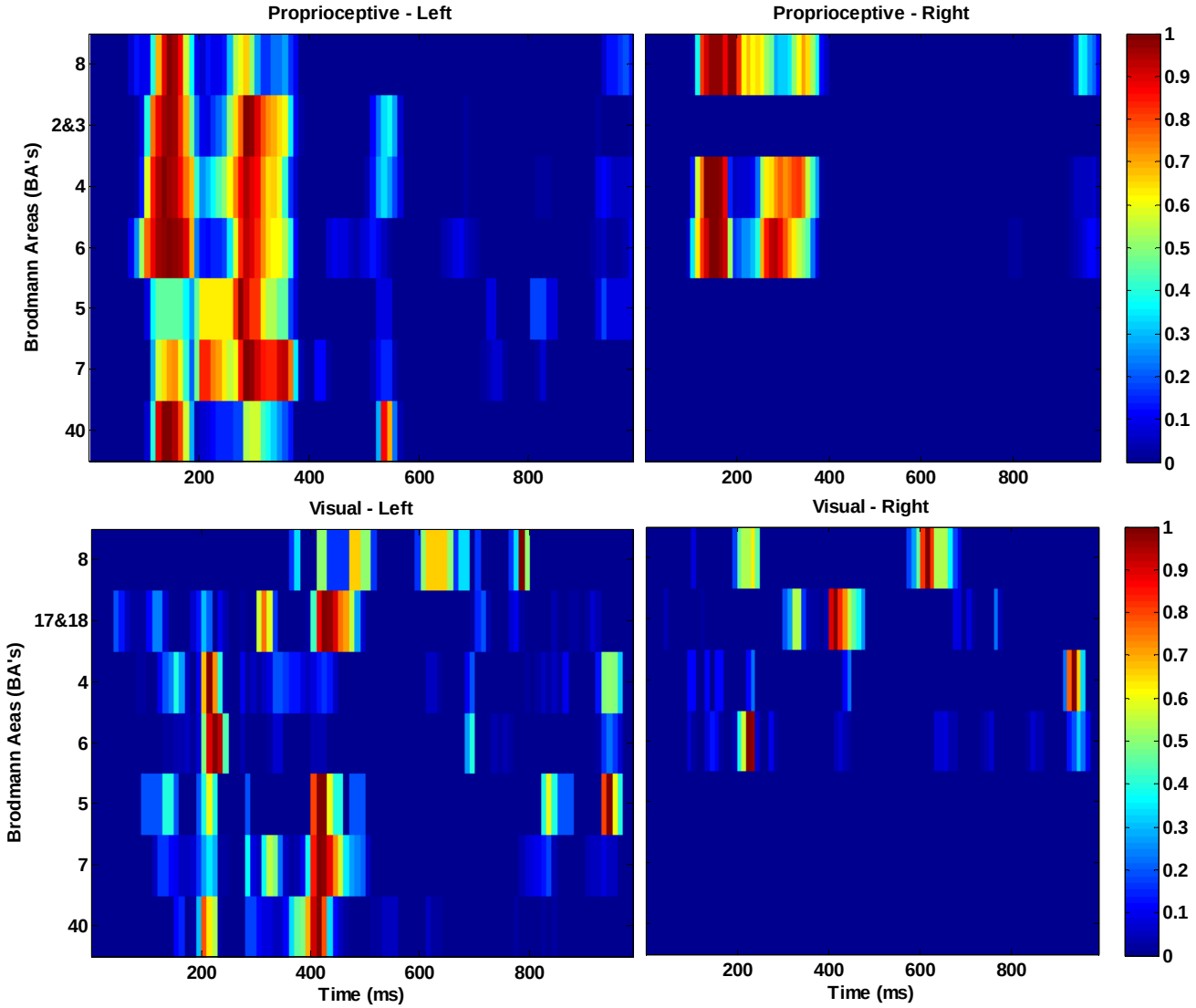

Subject NJ5013

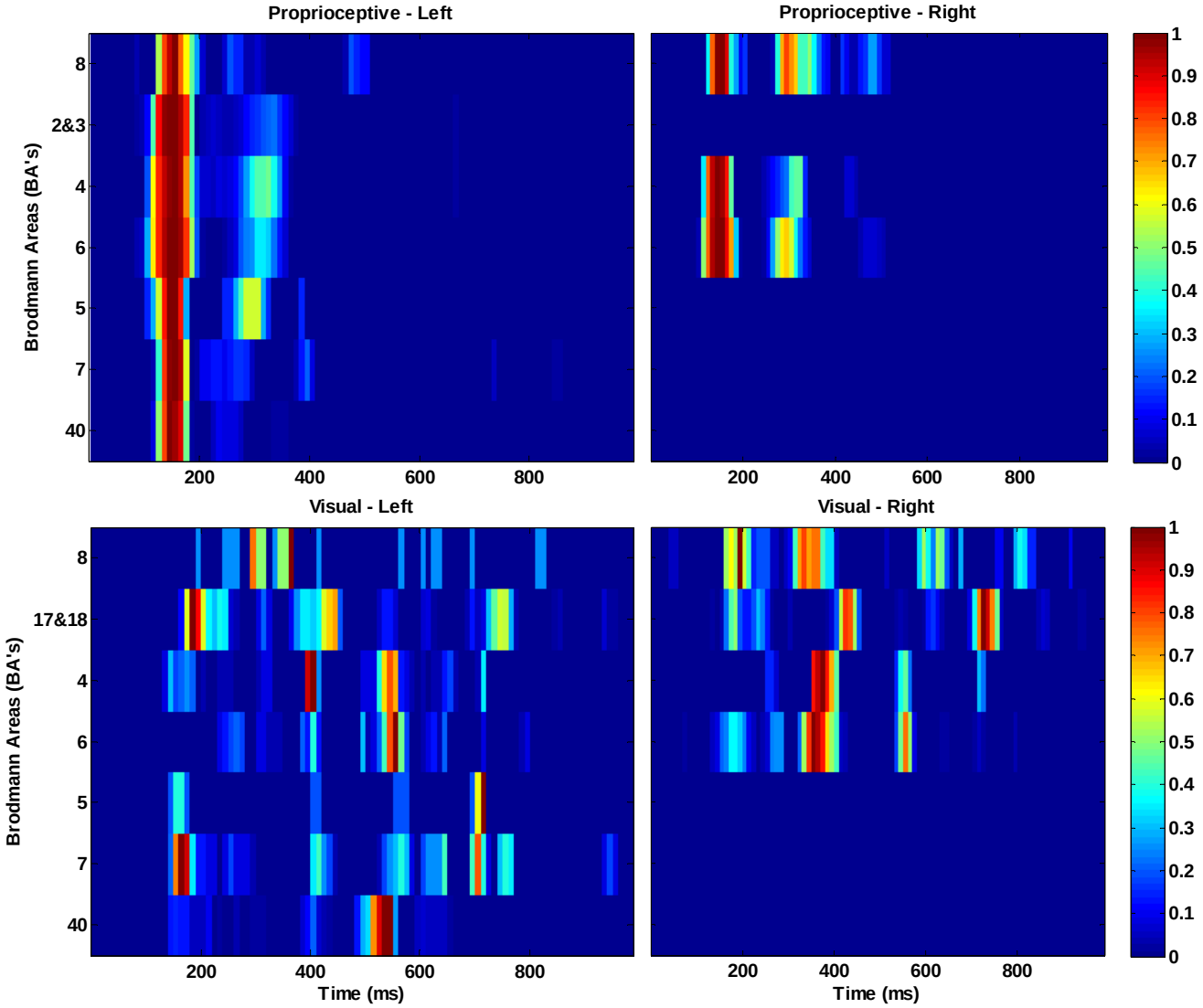

Subject NY2985

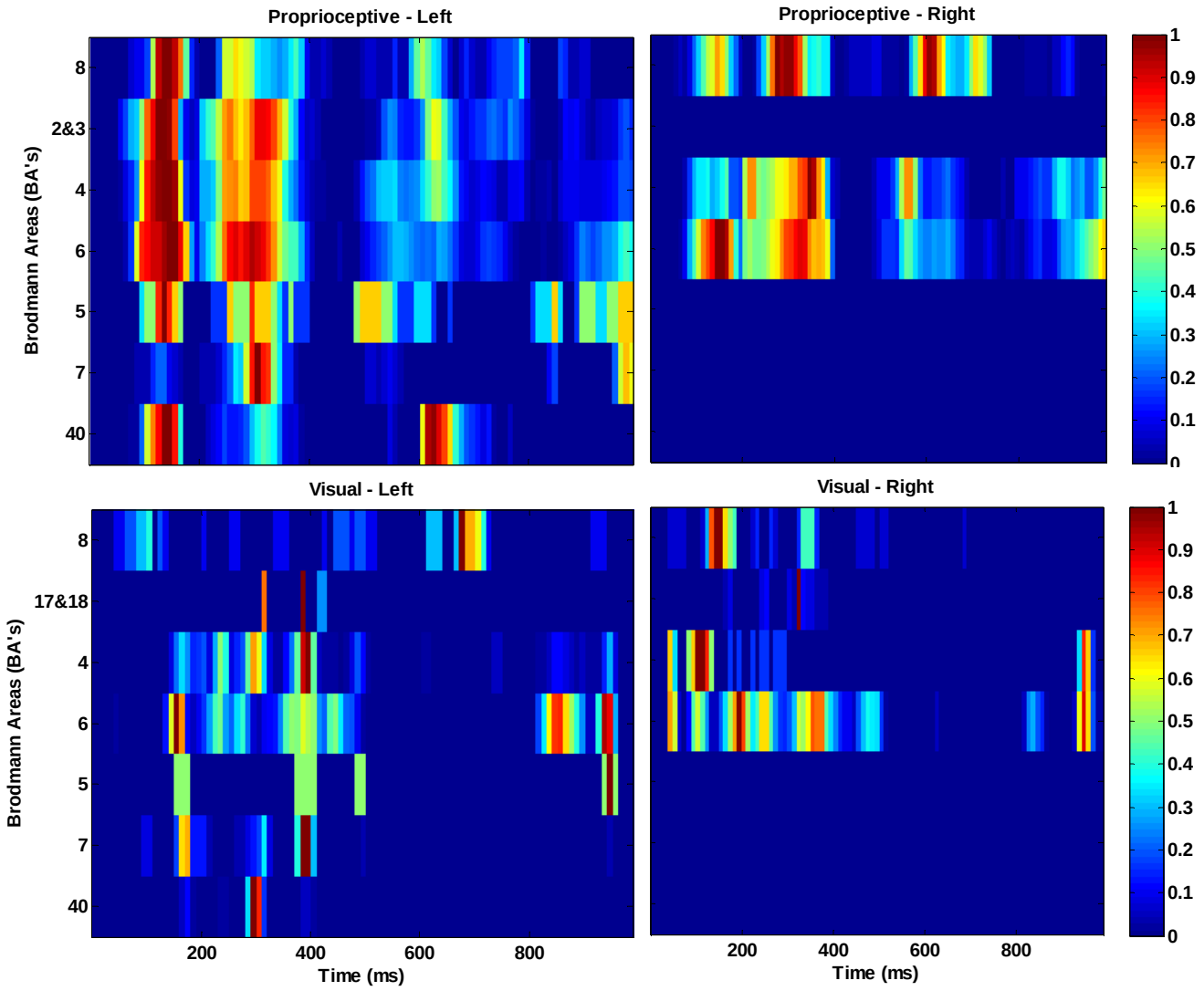

Subject PU7493

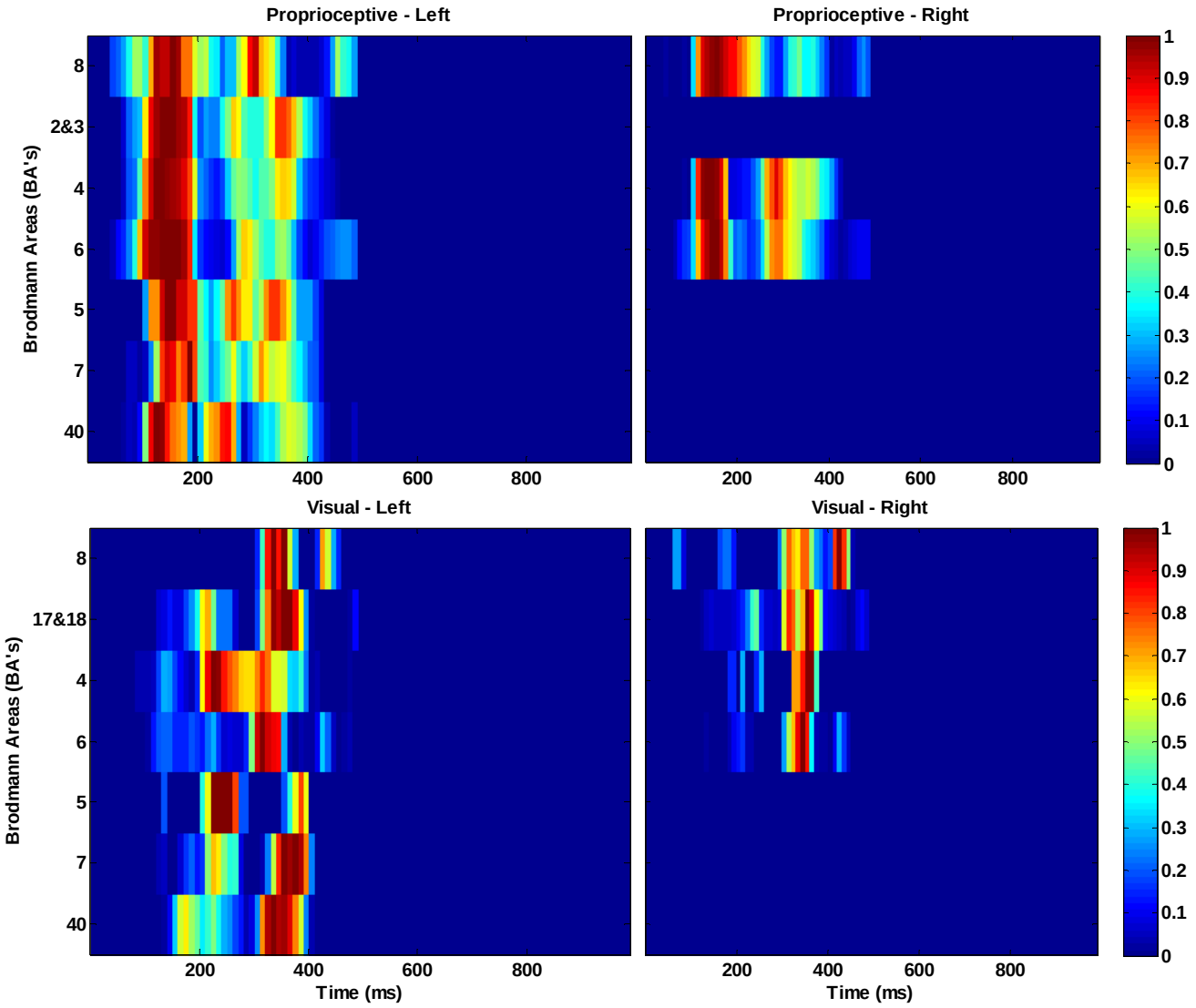
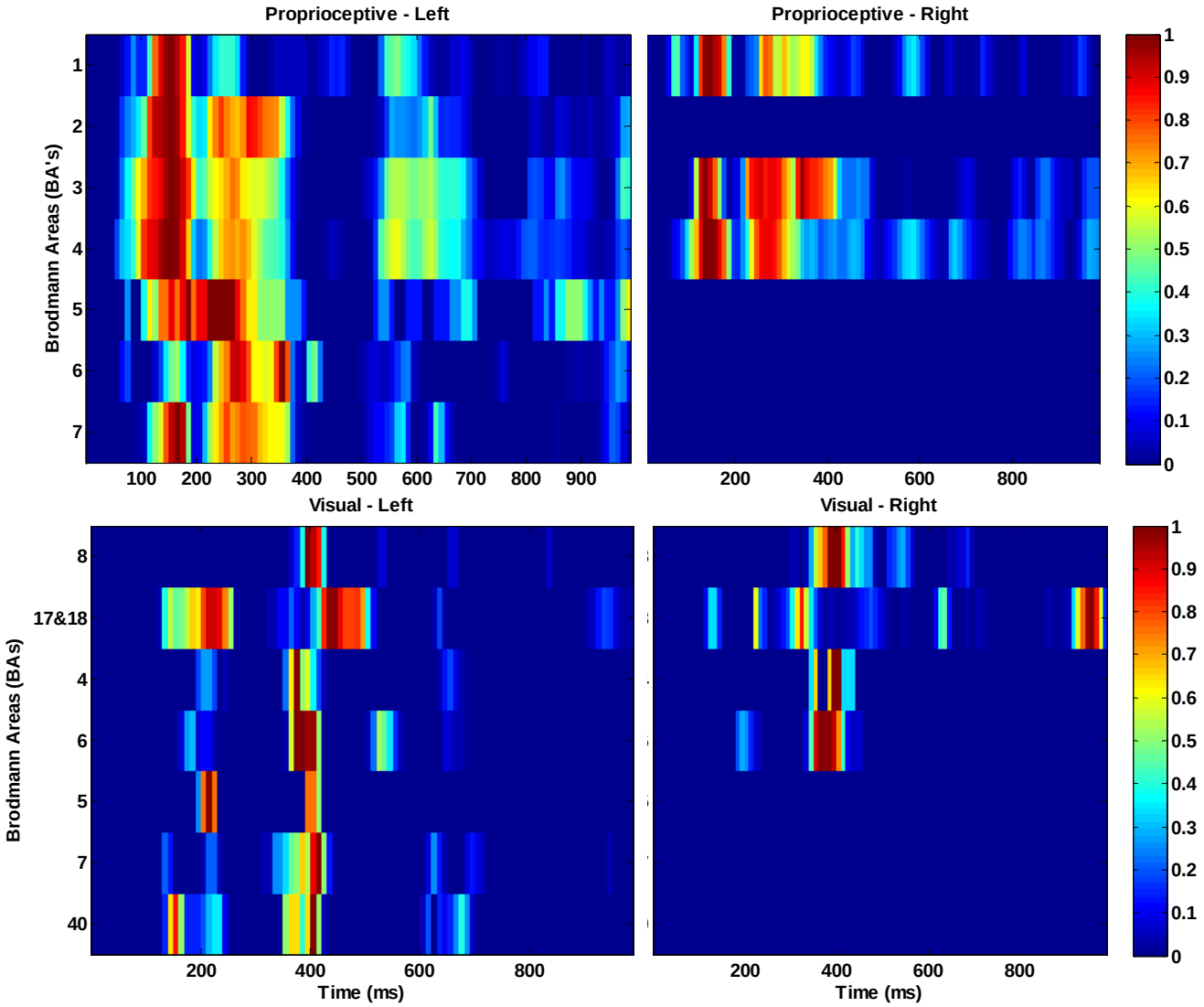
Subject RL3934